# CALIBRATING THE INERTIAL COORDINATE SYSTEM OF THE MINIATURE INERTIAL MEASUREMENT UNIT ON SAGE III ISS

A Thesis
Presented to
The Academic Faculty

by

Amy F. Rowell

In Partial Fulfillment
of the Requirements for the Degree
Master of Science in the
School of Aerospace Engineering

Georgia Institute of Technology
December 2016

# CALIBRATING THE INERTIAL COORDINATE SYSTEM OF THE MINIATURE INERTIAL MEASUREMENT UNIT ON SAGE III ISS

Approved by:

Dr. Alan Wilhite, Advisor
School of Aerospace Engineering
*Georgia Institute of Technology*

Dr. Marcus Holzinger
School of Aerospace Engineering
*Georgia Institute of Technology*

Dr. Joseph Zawodny
Science Directorate
*National Aeronautics and Space Administration*

Date Approved: 6 December 2016

*For my Bright Star.*

# ACKNOWLEDGEMENTS

Why anyone would voluntarily embark on the journey of writing a thesis is a question I have been pondering quite a lot over the last couple of years. I'm sure every graduate student has a unique reason, but, at the end of the day, when I answer that question for myself I very simply wanted to learn something new. And not just subject matter but also the techniques of the creation and dissemination of knowledge. For while this may be the end of my formal education, it is by no means the end of learning. There will always be a special place in my heart for those who love to learn, and I am ever grateful to those who have inspired me to continue pushing my boundaries.

SAGE III would not be possible without funding provided by NASA headquarters and support of LaRC management. I would like to acknowledge the Flight Software Systems Branch and Dave Haakenson for their encouragement in performing this research and thank Drs. Wilhite, Holzinger, and Zawodny for their patience throughout this process. Preparing a payload for launch at the same time as writing a thesis was not ideal, but I was fortunate to be surrounded by understanding and supportive mentors and team members. It has been a joy working on this payload with the SAGE III Project members, particularly the mission operations, ground system, and science teams.

My loving and supportive parents Fred and Mary Rowell sparked my interest in space and in music. For that I am forever indebted to them. Music may seem superfluous to someone getting an engineering degree, but music brings me joy and solace, and I rely on it heavily. Thanks to mum and dad for constantly singing and dancing around the house as I was growing up and for the many songs we continue to enjoy together.

I consider myself very lucky to have a gaggle of gorgeous girlfriends to put up with (and sometimes indulge) my crazy behavior. Shereen, Jen, Liz, Amber, and many others, you were there for me at all hours of the night and in many states of disarray. You gals always make me smile.

I most sincerely want to thank the DMP masters Drs. Charles Anthony Hill and Kevin Leavor, who carried me through my pessimism with immeasurable friendship and generous guidance. The words "thank you" do not begin to express my gratitude for your unwavering support. I will never meet two truer friends or kinder souls.

Someone I greatly admire frequently reminds me that, "we are the makers of meaning". I do not pretend that one thesis carries much meaning, but the relationships forged during the development of it will always mean something to me.

# TABLE OF CONTENTS

# LIST OF TABLES

# LIST OF FIGURES

# LIST OF ABBREVIATIONS

| | |
|---|---|
| **AEKF** | Additive Extended Kalman Filter |
| **AMS-02** | Alpha Magnetic Spectrometer |
| **APID** | Application Identifier |
| **ARW** | Angular Random Walk |
| **ASCII** | American Standard Code for Information Interchange |
| **ATBD** | Algorithm Theoretical Basis Document |
| **BAD** | Broadcast Ancillary Data |
| **CCD** | Charge-Coupled Device |
| **CMP** | Contamination Monitoring Package |
| **CRS** | Commercial Resupply Services |
| **CSSI** | Center for Space Standards & Innovation |
| **CSV** | Comma Separated Value |
| **DCM** | Direction Cosine Matrix |
| **DE430** | Development Ephemerides 430 |
| **DMP** | Disturbance Monitoring Package |
| **EHS** | Enhanced HOSC System |
| **EKF** | Extended Kalman Filter |
| **ELC-4** | ExPRESS Logistics Carrier-4 |
| **EOS** | Earth Observing System |
| **ESE** | Earth Science Enterprise |
| **ExPA** | ExPRESS Payload Adapter |
| **ExPRESS** | Expedite the Processing of Experiments to the Space Station |
| **FOO** | Flight Of Opportunity |
| **FTP** | File Transfer Protocol |
| **HEU** | Hexapod Electronics Unit |

| | |
|---|---|
| **HICO** | Hyperspectral Imager for the Coastal Ocean |
| **HMA** | Hexapod Mechanical Assembly |
| **HOSC** | Houston Operations Support Center |
| **HREP** | HICO and RAIDS Experiment Payload |
| **IAM** | Interface Adapter Module |
| **ICE** | Instrument Control Electronics |
| **ICRF** | International Celestial Referece Frame |
| **IFOV** | Instantaneous Field Of View |
| **IIR** | Infinite Impulse Response |
| **InGaAs** | Indium Gallium Arsenide |
| **ISS** | International Space Station |
| **ISSP** | International Space Station Program |
| **JEM** | Japanese Experiment Module |
| **KSC** | Kennedy Space Center |
| **LEO** | Low Earth Orbit |
| **LVLH** | Local Vertical Local Horizontal |
| **M3M** | Meteor–3M |
| **MATLAB** | Matrix Laboratory |
| **MEKF** | Multiplicative Extended Kalman Filter |
| **MIMU** | Miniature Inertial Measurement Unit |
| **MUSES** | Multiple User System for Earth Sensing |
| **NASA** | National Aeronautics and Space Administration |
| **NORAD** | North American Aerospace Defense Command |
| **QUEST** | Quaternion Estimator |
| **RAIDS** | Remote Atmospheric and Ionospheric Detection System |
| **RLG** | Ring Laser Gyroscope |
| **SA** | Sensor Assembly |

| | |
|---|---|
| **SAGE** | Stratospheric Aerosol and Gas Experiment |
| **SAGE II** | Stratospheric Aerosol and Gas Experiment II |
| **SAGE III** | Stratospheric Aerosol and Gas Experiment III |
| **SAM** | Stratospheric Aerosol Measurement |
| **SCF** | Science Computing Facility |
| **SDP** | Science Data Processing |
| **SGP4** | Simplified General Perturbations 4 |
| **SpaceX** | Space Exploration Technologies Corporation |
| **SSMC** | Solid State Memory Card |
| **STK** | Systems Tool Kit |
| **SVD** | Singular Value Decomposition |
| **TEA** | Torque Equilibrium Attitude |
| **TLE** | Two-line Element |
| **TRIAD** | Tri-axial Attitude Determination |
| **UTCG** | Coordinated Universal Time, Gregorian Calendar |

# SUMMARY

The Stratospheric Aerosol and Gas Experiment III (SAGE III) on the International Space Station (ISS) will extend NASA Langley Research Center's long legacy of satellite atmospheric occultation measurements. Unlike its predecessors, SAGE III ISS will encounter off-nadir attitudes and jitter conditions caused by the mechanical instability of the ISS environment. The retrieval algorithm for the SAGE III science data product requires precise and accurate knowledge of the instrument boresight pointing with respect to Earth and the radiant target, either Sun or Moon. Without knowledge of the attitude drifts at the instrument scan head and the associated mechanical jitter the data retrievals will be compromised. A subsystem on the payload termed the Disturbance Monitoring Package (DMP), which is comprised of a Miniature Inertial Measurement Unit (MIMU) built by Honeywell Aerospace of Clearwater, Florida, was added to quantify this disturbance. By calibrating coordinate transformations on orbit and using attitude determination algorithms, the pointing information needed for post-processing can be derived. This research will provide the necessary calibration methods and simulate the on-orbit mechanical environment to prepare for the SAGE III ISS mission ensuring that the data retrievals maintain the high standard expected of this class of instrument.

# CHAPTER I

# INTRODUCTION

This chapter serves as a brief, high-level introduction to the material contained herein. The purpose of this research is explained first and is followed by a guide of the chapters to come.

## *1.1 Motivation and Significance of Research*

The Stratospheric Aerosol and Gas Experiment III (SAGE III) on the International Space Station (ISS) instrument payload is a passive remote sensing instrument that measures gaseous and aerosol constituents in Earth's atmosphere from orbit using a method called atmospheric occultation. Like a photographic camera without a flash, *passive* remote sensors do not carry their own light source, but instead collect incoming light from remote sources. A photographic camera that uses a flash would be called an *active* remote sensor. The SAGE III ISS payload consists of a spectrographic science instrument and telescope supported by several subsystems that takes measurements of the atmosphere by collecting sunlight or moonlight after that light has interacted with the atmosphere. Paramount to this thesis, the Disturbance Monitoring Package (DMP) subsystem on SAGE III ISS is a Honeywell Miniature Inertial Measurement Unit (MIMU). With a sensor block consisting of three orthogonally arranged Honeywell GG1320 Ring Laser Gyroscopes (RLGs), the DMP will be used to measure the changing payload attitude and to monitor SAGE III instrument vibrations both as the ISS vacillates nominally and during the anticipated recurring disturbance events. The project objectives of the DMP are twofold: flag invalid data and increase the accuracy of science retrievals. By monitoring vibration, potentially invalid science measurements captured during unusually large jitter events can be

flagged. Because of assumptions used in science calculations about how well the telescope is pointing and how stable the instrument is during data collection, large mechanical jitter events can cause science results to be invalid. Since the mechanism for flagging invalid data using the DMP is already in place, the focus of this thesis will be to address the second objective. Being able to relate the lower frequency disturbances measured at the DMP to the instrument scan head will allow for an improved understanding of boresight pointing, and ultimately, a higher quality data product potentially over a larger region of the atmosphere. The DMP can provide scan head deflections as a function of time, allowing corrections to be introduced in post-processing. This requires knowledge of the DMP reported change in attitude, the current orientation of the Hexapod Mechanical Assembly (HMA) subsystem and SAGE III scan head, and a method of combining this information and propagating error estimations. The purpose of this thesis is to develop an on-orbit DMP calibration technique to derive these needed coordinate transformations and error estimations after installation of the payload on the ISS, to develop a robust algorithm and validate this technique well in advance of launch with high-fidelity orbit simulations, and to define an attitude determination algorithm that can be incorporated into the science inversion algorithm.

A scan head and scan mirror on SAGE III can rotate the telescope boresight around two axes to point the instrument. SAGE III can perform three event types to take atmospheric measurements. Solar events use the Sun as an emissive target viewed as either a Sunrise or a Sunset from the perspective of the ISS. The Moon is not a light source, but the sunlight reflecting off of the Moon allows for Moonrise and Moonset events similar to the solar events. During rise and set events, light from the target passes through the atmosphere before being measured by the SAGE III instrument. Limb scattering events measure scattering of solar radiation off of Earth's atmosphere without a radiative target in view behind the atmosphere. Atmospheric

measurements from solar and lunar data are the primary objective of the SAGE III ISS mission, and limb scattering measurements serve as an experimental data product. The calibration of the DMP will enable correction of pointing during instrument scans of the atmosphere by providing a coordinate transformation between the coordinates in which the DMP measurements are made and the scan head coordinates in which the science measurements are made. The mathematical coordinate transformation is used to relate disturbances at the base of the payload measured by the DMP to the instrument scan head. The final relative orientations of the DMP and scan head subsystems cannot be known before installation on ISS because of launch vibrations that can cause the instruments to shift with respect to each other on the instrument pallet. Therefore, calibration must occur on orbit as the ISS rotates to maintain its attitude with respect to the local horizon. The derived coordinate transformation will be applied to all event types on orbit. Absolute attitude determination is necessary only for limb scattering measurements because this technique does not track an emissive source with a known location as with solar and lunar events.

Improvements to the SAGE III data products can be as far reaching as retrieving gaseous species data lower into the troposphere than the previous family of SAGE instruments. Overall the techniques developed in this thesis provide additional tools in the arsenal for improving science data, integrating information between separate subsystems on the payload, and laying out the path to an independent attitude data product derived from the DMP subsystem.

## *1.2 Organization of Thesis*

SAGE III ISS is the latest in a line of Earth observing instruments that have roots back to the Apollo program in 1975. SAGE III will contribute to the collective knowledge of Earth's stratospheric composition not only for ozone and aerosols but also for several more trace gases. The passive remote-sensing measurement technique

used by SAGE III, called occultation, measures light transmitted through Earth's atmosphere. Science data products result from a mathematical inversion algorithm applied to transmitted light along slant paths (see Section 2.1).

The SAGE III ISS payload is comprised of several distinct subsystems which are described in Chapter 2: the SAGE III instrument assembly, an actuator Hexapod pointing system, contamination monitoring package, disturbance monitoring package, and a flight computer (see Section 2.1.2). This integrated payload works in collaboration to facilitate science measurements and to ensure the safety of the science instrument and quality of the science data. The position of the payload on ISS will be on the starboard truss in a nadir-viewing configuration. The anticipated ISS motions experienced by SAGE III are difficult to predict pre-launch. Attitude variations are monitored at several locations on station, but internal ISS bending modes cause a unique attitude experience throughout station. The DMP will capture the attitude changes of the SAGE III payload using three RLGs, one for each axis. The Sensor Assembly (SA) captures an incomplete attitude providing both an azimuth and elevation angle of the Sun measurements. But the SA can be used as a Sun attitude sensor utilizing a novel approach.

Chapter 3 details the creation of a simulated data set of SA and DMP measurements using actual ISS positions and attitudes from 2014 and the construction of each SA and DMP attitude quaternion. A quaternion is a mathematical representation of a rotation in three dimensional space and is discussed in detail in Section 2.2. It is in the construction of the SA quaternion that the lack of a degree of freedom is accounted for using the total rotation measurement from the DMP. With SA and DMP input vectors, a robust coordinate transformation can be found using the *optimal fast quaternion method* as described in Section 3.2.1. The method solves the classical attitude determination problem using two vectors in each coordinate system as input to generate one coordinate transformation quaternion. The path forward for

a limb scattering attitude determination method using the same simulated data set is described in Section 3.3.

The results of applying the calibration method to the simulated data set with a focus on providing answers needed for on-orbit operations are discussed in Chapter 4. Each science event produces one SA and one DMP rotation axis vector. Vector pairs are constructed by randomly sampling from a subset of all events. Coordinate transformation quaternions are generated using the vector pairs as input to the optimal fast quaternion method. One-thousand Monte Carlo simulations are performed to generate average coordinate transformations for four test cases. Simulations are run for levels of angular error down to 1 arcminute to show the relationship of the error and error bars as a function of the number of combinations of rotation axes. Knowing this error trend will allow the SAGE III DMP science team to decide on a reasonable coordinate transformation error requirement for flight.

Baseline conditions are covered in Sections 4.4.1 and 4.4.3, and flight-like conditions are presented in Sections 4.4.2 and 4.4.4. "Baseline" indicates that the simulated data are used as-is, whereas "flight-like" cases inject Gaussian error into the simulated data sets based on subsystem measurement accuracies found during ground testing. Statistical errors are quantified for important properties in order to incorporate the calibration methods into the science inversion algorithm (see Section 4.4.6) and the possible impacts of unexpected non-orthogonality of the DMP gyros are explored (see Section 4.4.7).

The topics of Chapter 5 are the conclusions drawn from the Chapter 4 analyses and future applications of this thesis research. Future work will primarily focus on flight implementation and the development of and extensibility of a DMP absolute attitude data product.

# CHAPTER II

# BACKGROUND

## *2.1 Stratospheric Aerosol and Gas Experiment*

The Stratospheric Aerosol and Gas Experiment III (SAGE III) on the International Space Station (ISS) payload is a new atmospheric remote sensing science platform that is currently scheduled for launch in early 2017 from the National Aeronautics and Space Administration's (NASA) Kennedy Space Center (KSC). The payload will be delivered to orbit in the unpressurized compartment of a Space Exploration Technologies Corporation (SpaceX) Dragon spacecraft during the Falcon 9 Commercial Resupply Services (CRS) 10 mission. Using the ISS as a platform is attractive because power and data service are readily available, and because the orbit is ideal for the desired latitude coverage. ISS orbital dynamics introduce new challenges into the science data retrieval that have not needed to be addressed in previous, similar missions. Jitter conditions on the ISS are largely unknown for science payloads, and since SAGE III will be the first payload of its size to be deployed to the ExPRESS (Expedite the Processing of Experiments to the Space Station) Logistics Carrier-4 (ELC-4) site, shown in Figure 1, there is little reference data to definitively predict mechanical conditions. The ISS attitude is not stabilized with respect to the local horizon, but rather wobbles slowly as a function of solar beta angle to achieve a Torque Equilibrium Attitude (TEA). This prevents saturation of the four control moment gyroscopes aboard ISS that are actuated to control station attitude. The reported ISS attitude is unreliable at the ELC-4 site because the station exhibits internal bending modes, a degree of freedom that is attitude-dependent and poorly characterized. Additionally, to preserve the integrity of the SAGE III data product,

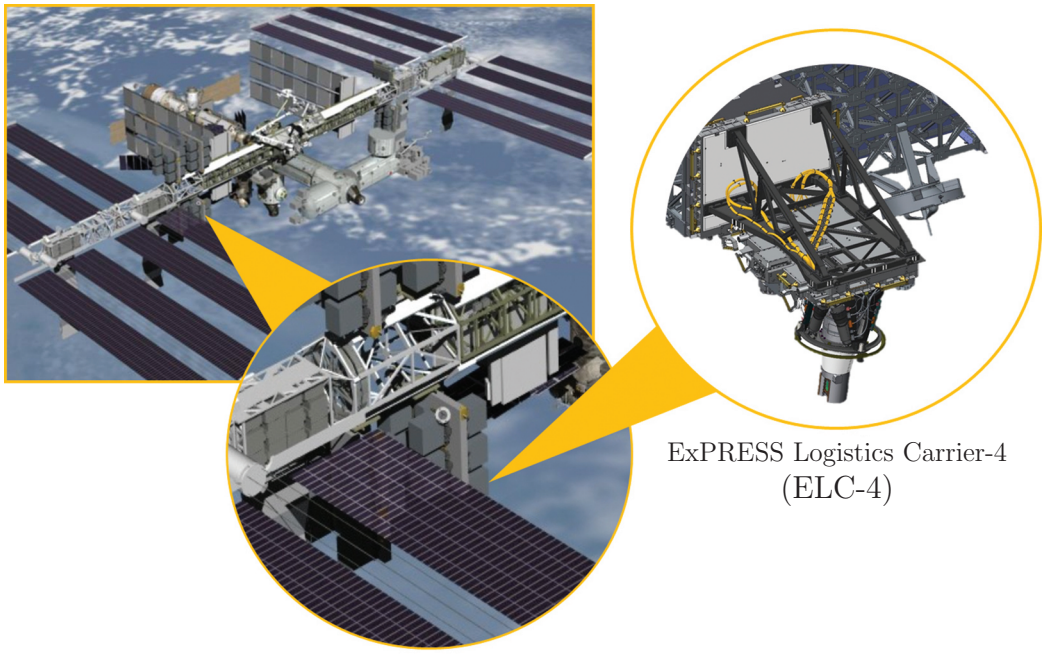


**Figure 1: SAGE III Position on ISS.** The position and orientation of the SAGE III payload on ELC-4 is depicted.

the possibility of significant and intermittent payload vibrations must be anticipated and handled. Failure to address these attitude uncertainties will negatively impact science data retrievals.

The SAGE III ISS Project descends from a long line of Earth observing satellites. Beginning with the Stratospheric Aerosol Measurement (SAM) in the 1970s, SAGE, SAGE II, and most recently the SAGE III Meteor–3M mission (2002–2005, sun-synchronous orbit) NASA has been monitoring Earth's stratosphere from Low Earth Orbit (LEO) for over 35 years. Three nearly identical SAGE III instruments were built by Ball Aerospace & Technologies Corporation (Boulder, Colorado) under contract to NASA's Langley Research Center in Hampton, Virginia. The individual instruments were given the three-letter designations M3M, ISS, and FOO, indicating respectively that the first mission had been slated to operate aboard Meteor–3M (M3M), the second aboard the International Space Station, and the third was awaiting an undetermined Flight of Opportunity (FOO). With this long heritage,

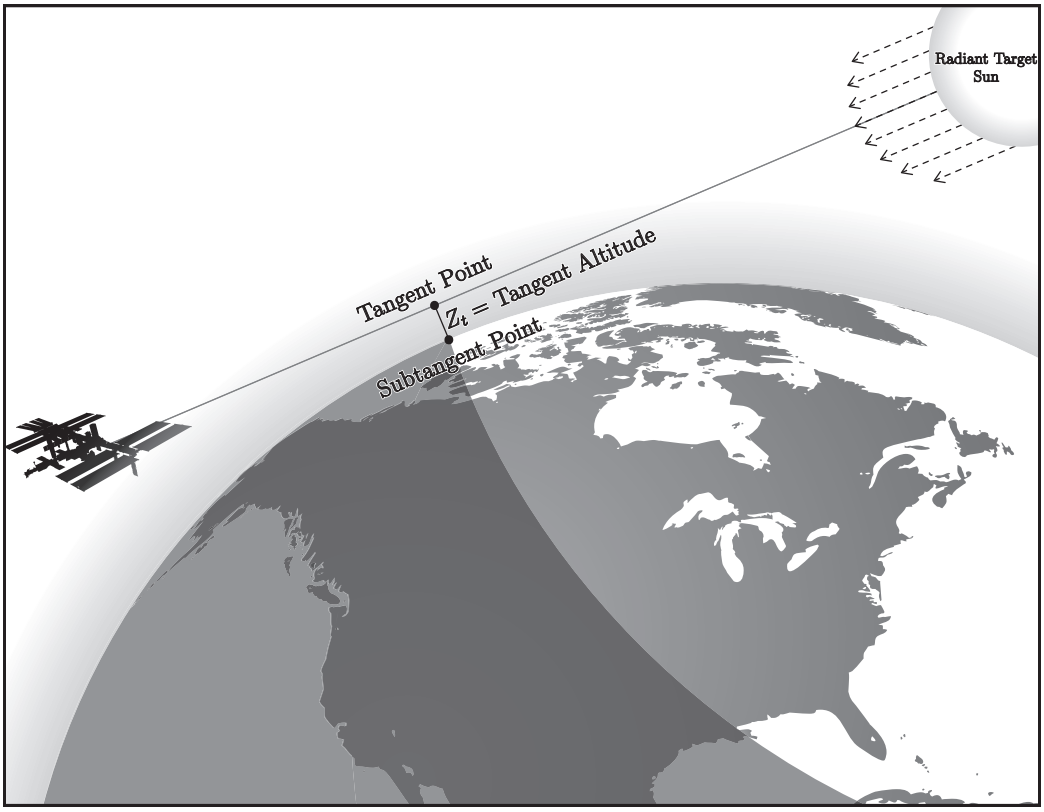


**Figure 2: Solar Occultation Geometry.** An illustration of a SAGE III ISS solar occultation event shows the measurement location at the Tangent Point.

SAGE III ISS will continue to contribute to NASA's Earth Observing System (EOS) to better understand Earth's climate and environment (McCormick, 1991; Bradley et al., 1994).

The SAGE instruments provide vertical profiles of aerosols and trace gases and are considered international standards in ozone and aerosol for accuracy and trending. SAGE III instruments measure the light that transmits through atmospheric gases, clouds, and aerosols using an emissive target such as the Sun or Moon. This method of passive remote sensing, referred to as occultation and shown in Figure 2, can be used to measure constituents in the stratosphere and upper troposphere. Atmospheric constituents can scatter and/or absorb radiation from the target as a function of wavelength. Occultation instruments measure the unattenuated balance of light along the line-of-sight to the target to infer the molecular species and aerosol extinction

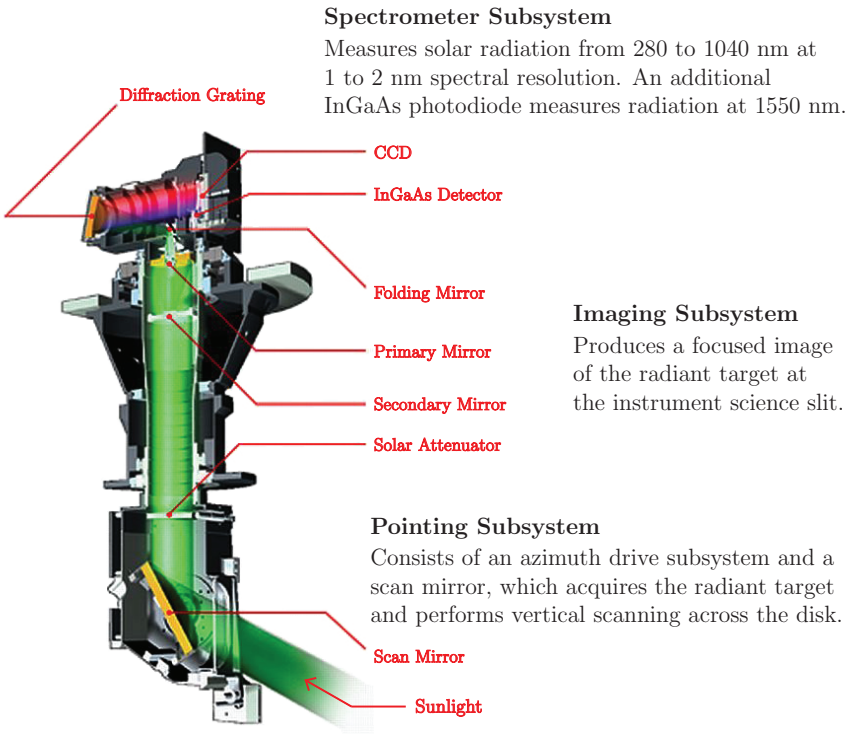


**Figure 3: SAGE III Optics Illustration.** Light from the radiant target enters the telescope and is focused on the science slit in the SAGE III scan head.

present within the atmospheric path. The SAGE III instruments can perform both solar and lunar occultations as well as limb scatter events that measure the scattering of solar radiation by Earth's atmosphere.

The SAGE III ISS Dall-Kirkham telescope focuses light from infinity onto the science aperture. The rectangular science slit's instantaneous field of view (IFOV) is approximately 0.5×5.0 arcminutes, the smaller dimension being oriented along the local vertical to limit the field stop to no more than 500 meters in altitude at the tangent point. Through the science aperture, incident light falls onto a grating spectrometer that measures intensity as a function of wavelength by recording the induced electron current across each pixel of a charge-coupled device (CCD) as depicted in Figure 3. The SAGE III grating spectrometer is sensitive to wavelengths between 280 nm and 1040 nm with approximately 1–2 nm resolution, depending on where the

light falls across the CCD. Light in these wavelengths are disbursed in the first order onto the CCD from a holographically recorded plano–concave diffraction grating. Additionally, a wide band 1550 nm Indium Gallium Arsenide (InGaAs) photodiode measures light in the zeroth order for cloud and solar edge detection. Science channel wavelengths may be selected during mission operations providing the flexibility to add species to the data product without a significant impact to the hardware. Data product retrieval is achieved using a mathematical inversion of the remote sensing data.

### 2.1.1 The SAGE III Meteor–3M Mission

The former Russian Aviation and Space Agency, now known as Роскосмос ("Roskosmos", the Russian Federal Space Agency) worked in close cooperation with NASA to provide a flight for one of the SAGE III instruments aboard a newly-designed Метеор–3М (Meteor–3M) spacecraft (Roberts et al., 1996).

SAGE III aboard Meteor–3M was launched from the Baikonur Cosmodrome in Kazakhstan at 17:18:57 UTC on 10 December 2001. A Ukrainian-built Зенит-2 (Zenit-2, meaning "Zenith-2") rocket carried the satellite payload, logged as Meteor–3M-N1 (the first flight of a Meteor–3M spacecraft) into a nearly-polar sun-synchronous orbit. Power to SAGE III was activated on 17 December 2001, after which the instrument was placed into a standby mode for a period of outgassing and spacecraft qualification (Chu et al., 2002). Solar measurements commenced on 27 February 2002, and the first lunar measurement was made on 4 March 2002. Between occultation events, the instrument exercised its programmatic flexibility to accomplish limb scattering measurements. The regular science data product is available from 7 May 2002 through 31 December 2005. After the Russian spacecraft suffered a power supply failure from which it could not recover, the SAGE III mission was officially ended

**Table 1: SAGE Instrument History.** Shown is a summary of the lineage of the SAM/SAGE suite of instruments.

| Experiment | Era | Orbit/Platform | Channels (Species) | Science Highlight |
|---|---|---|---|---|
| SAM | 1975 | Inclined/ Apollo-Soyuz | Single channel at 840 nm | Demonstration |
| SAM II | 1978–1993 | Sun-synch/ Nimbus 7 | Single channel at 1 $\mu$m | Polar stratospheric clouds |
| SAGE I | 1979–1981 | Inclined/AEM–2 | Ozone, aerosol $NO_2$ | Pre-decline ozone baseline |
| SAGE II | 1984–2005 | Inclined/ERBS | Addition of water vapor | Ozone trends, extreme aerosol variability |
| SAGE III | 2001–2006 and 2017+ | Sun-synch/ Meteor–3M and Inclined/ISS | Addition of $O_2$; Mesospheric ozone Night-time: Ozone, $NO_2$, $NO_3$ | Tropospheric measurements, lunar occultation, and limb scattering |

on 6 March 2006. The Meteor–3M instrument provided over 3.5 years of high latitude observations that have contributed to the record used by NASA's Earth Science Enterprise (ESE) for the understanding and analysis of geophysical trends.

Table 1 details the heritage of SAGE instruments and lists the species retrieved from each instrument. SAGE III Meteor–3M has provided the widest suite of species including aerosol extinctions at 9 wavelengths (385, 448, 521, 596, 676, 754, 868, 1019, and 1550 nm).

Achieving a data product suitable for validation and analysis by the scientific community is a complex procedure. After the raw (Level 0) data are collected the data processing algorithm shown in Figure 4 is used. A full description of each step is given in Damadeo et al. (2013). For the purpose of this thesis only the relevant steps are described in detail.

Instrument boresight pointing determines the location on the solar disk from which

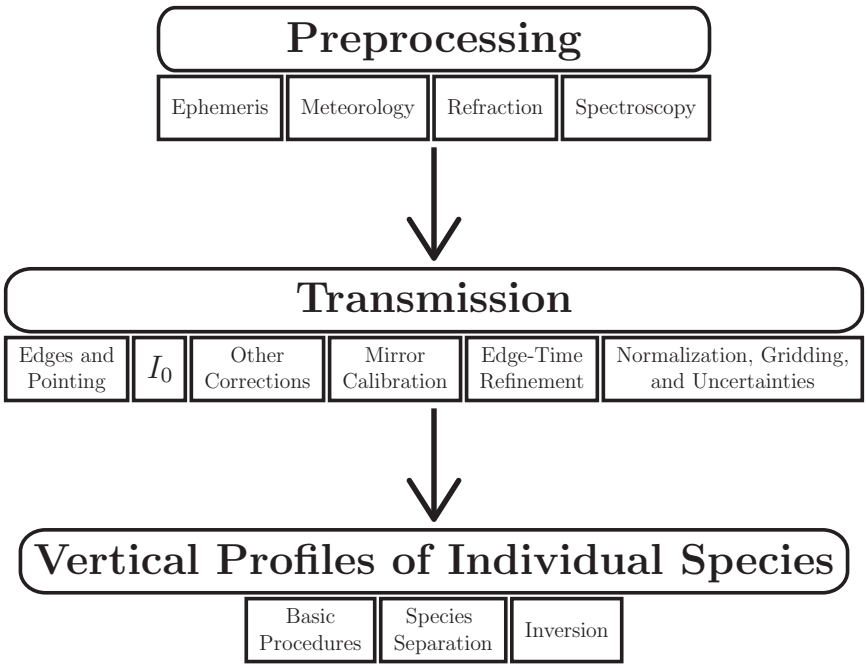


**Figure 4: SAGE Algorithm Version 7.0 Flow.** This outline of the SAGE algorithm was adapted directly from Damadeo et al. (2013).

the measured solar radiation originated. This is essential to the science retrieval because atmospheric transmission must be determined as a ratio relative to the incident light. Boresight pointing also provides the measurement tangent point that maps measurements to a latitude, longitude, and altitude on Earth. For solar occultations on SAGE III Meteor–3M, the radiometric top and bottom edges of the Sun were used along with a fixed scan head nadir orientation to establish instrument boresight pointing. An edge was defined as a mathematical inflection point in the measured limb darkening curve. The center of the Sun was determined from these edge measurements, and the Science Computing Facility (SCF) version of the geopositioning software package Science Data Processing (SDP) Toolkit was used to determine absolute instrument scan mirror pointing. Taking into account refraction by the atmosphere, the tangent point is the point on the (potentially curved) line-of-sight between the instrument and Sun that is closest to the Earth's surface as seen in Figure 2. The

geodetic latitude, longitude, and altitude of this point defines the location of the retrieved science data product. For the Edges and Pointing step in the Transmission algorithm of Figure 4, each data packet is mapped to the corresponding position on the Sun. This is accomplished by driving the instrument scan mirror at a constant rate of motion, allowing each data packet to be interpolated to a location on the Sun. The Meteor–3M satellite provided a stable environment for optical geolocation with SAGE III. Because Meteor–3M was a three-axis stabilized spacecraft there was little concern for jitter, and therefore the aforementioned process of finding solar centers met pointing knowledge requirements.

Extinction of sunlight from atmospheric constituents increases as the line-of-sight passes lower into Earth's atmosphere. The bottom of the Sun is more distorted than the top because of refraction. It is increasingly difficult to detect the bottom edge of the Sun relative to the spacecraft when it passes below the tropopause. The exercise is rendered impossible by interference from cloud ceilings or when the solar edge falls below Earth's horizon. Lower altitude retrievals were performed on Meteor–3M data by calculating an "apparent" scan rate from the edge time series and assuming that rate remained fixed when the bottom edge was lost. The apparent rate is a combination of the constant, known scan mirror rate and extrapolated motion of the spacecraft. Low altitude data were acquired using a transmission algorithm termed "Rate Fix". The algorithm linearly extrapolates the slope of the apparent scan rate to estimate transmission lower in the troposphere. The addition of a shift and stretch function smooths some of the noise introduced by Rate Fix and in the raw data. Of the data collected during the Meteor–3M mission, the data below 10 km were available in the product less than 75% of the time as shown in Figure 5. Lower than 5 km the percentage drops to 25% or less.

Although the post-processing boresight pointing algorithm described above has been effective in the past, it is not the ideal method. In the upcoming SAGE III ISS

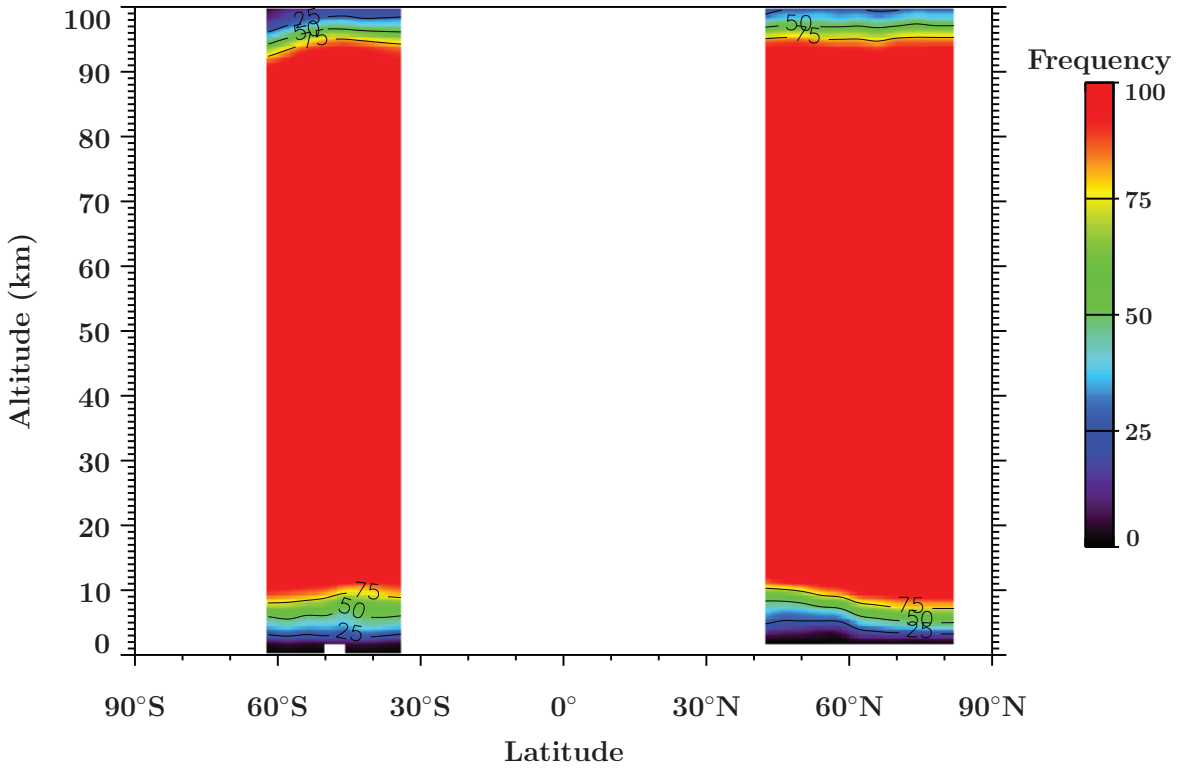


**Figure 5: SAGE III Meteor–3M Altitude Data Product Frequency vs. Latitude.** For solar occultation the frequency is the percentage of the total data products for which the data were available at a given latitude and altitude.

mission it is desired to better account for spacecraft motions and consequently improve the data usability lower into the troposphere. The addition of a payload angular rate sensor that can precisely track attitude is a practicable and promising method. To summarize, the local geometric bottom of the solar disk during occultation measurements at low altitudes is often obscured, making it difficult to accurately determine where the instrument is pointing on the Sun and diminishing retrieval accuracy. Rate sensor information in post-processing is expected to improve pointing accuracy and the retrieval of SAGE III ISS science products. If the process can be refined to gather data lower than 10 km and on a more consistent basis, this would extend the scientific usability of the SAGE III ISS data, bring a new user community to the project, and

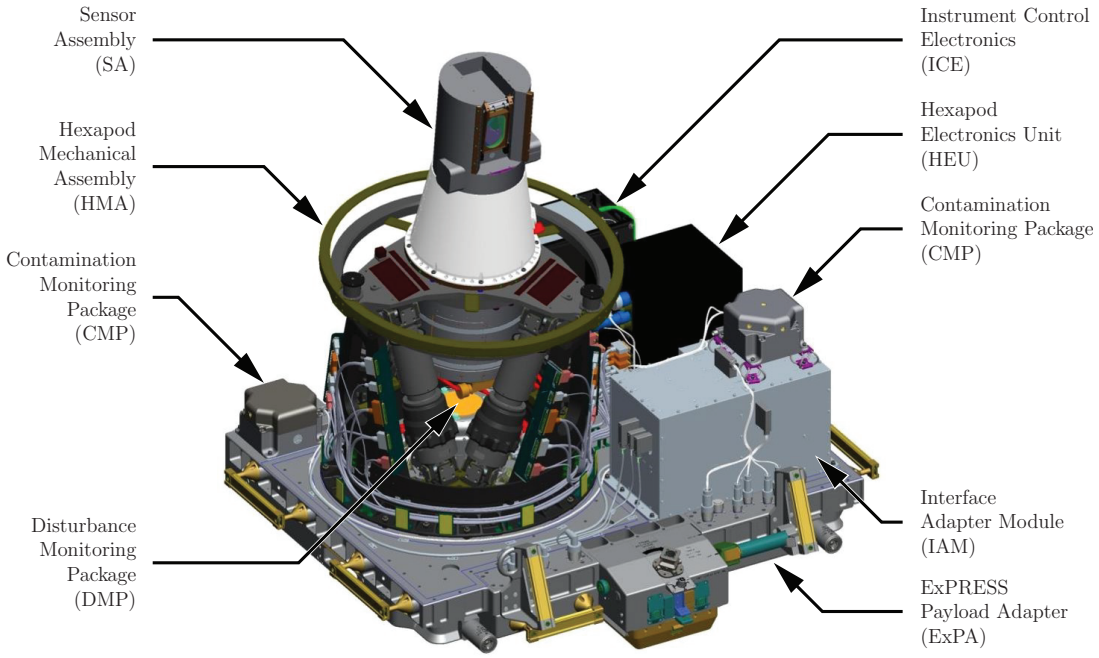


**Figure 6: The SAGE III ISS Payload.** The individual subsystems of the SAGE III ISS payload are listed.

provide new insights into upper tropospheric chemistry.

### 2.1.2 The Future: SAGE III ISS

Plans to deploy SAGE III ISS are currently under way. The SAGE III payload will be integrated onto a nadir-viewing platform and attached to the ELC-4 on the ISS no earlier than January 2017. Figure 6 details the components of the SAGE III payload and how they are arranged on the ExPRESS Payload Adapter (ExPA). The ELC-4 provides a mechanical mounting surface, electrical power, and command and data handling. The ISS achieves a TEA more than 75% of the time, which seeks to minimize solar, magnetic, drag, and gravitational gradient interactions. The Local Vertical Local Horizontal (LVLH) Coordinate System for the ISS is defined in Figure 7, where the +X-axis is along the velocity vector, the +Z-axis is towards the center of mass of the Earth (the nadir direction), and the +Y-axis completes a right handed coordinate system and is directed opposite the osculating orbital angular momentum vector (ISSP, 2001).

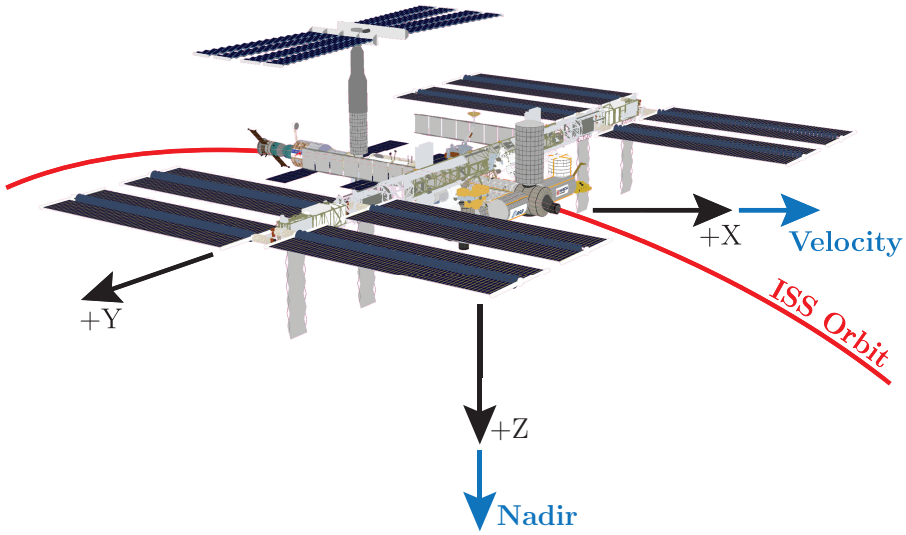


**Figure 7: ISS Coordinate System.** A Local Vertical Local Horizontal (LVLH) Reference Coordinate System is defined for the ISS. The X–Z-plane is the osculating orbital plane. The Y-axis completes the rotating right-handed Cartesian coordinate system and is directed opposite the orbital angular momentum vector.

The SAGE III Meteor–3M mission described in Section 2.1.1 made measurements exclusively at upper latitudes in both hemispheres, whereas the ISS mission will cover the middle to lower latitudes. Using the same occultation method as SAGE III Meteor–3M, SAGE III ISS will retrieve atmospheric state and chemistry data products. Accurate data retrievals rely on precise pointing knowledge of the Sensor Assembly (SA) scan head with respect to both the Sun and Earth. ISS orbital and tumbling mechanics must be taken into account when predicting and planning SAGE III data gathering event opportunities. The ISS operational schedule must also be considered. For example, the ISS altitude is typically descending as a result of drag. To compensate, periodic re-boosts by visiting vehicles are performed, which abruptly change the ISS position relative to Earth and hence the expected solar acquisition coordinates. The ISS attitude angles (roll, pitch, and yaw with respect to the +X-axis and LVLH coordinates) are also irregular and must be taken into account. Mechanical disturbances to the ISS occur during spacecraft docking events, which also produce significant changes to the ISS TEA while the visiting vehicle remains docked. The

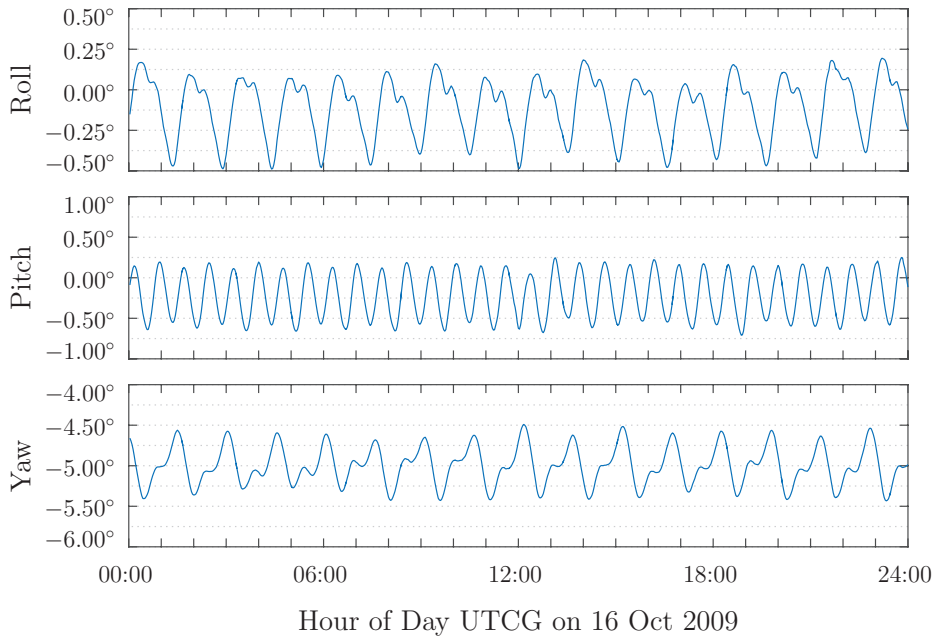


**Figure 8: HREP Star Tracker Attitude Time Series.** The roll, pitch, and yaw attitude variations shown over the course of one day are taken with respect to the +X-axis and LVLH coordinates.

many possible sources of jitter include docking and capture events, ISS bending modes of vibration, crew and robotic movements, and solar panel articulations.

ISS attitude data have been collected on orbit by the Hyperspectral Imager for the Coastal Ocean (HICO) and the Remote Atmospheric and Ionospheric Detection System (RAIDS) Experimental Payload (HREP) star tracker since 2009. Analyzing data from October 2009 through June 2011 provides some insight into ISS disturbance severity and duration. Docking events are by far the most disruptive, but are not common occurrences. The time series in Figure 8 demonstrates that on a daily basis the typical roll and pitch variations tend to be on the order of a half of a degree, whereas the yaw variation can be twice as much.

As described in more detail in Section 3.1.1 on page 34, the ISS reports coarse attitude in its own Broadcast Ancillary Data (BAD) that is available in real time

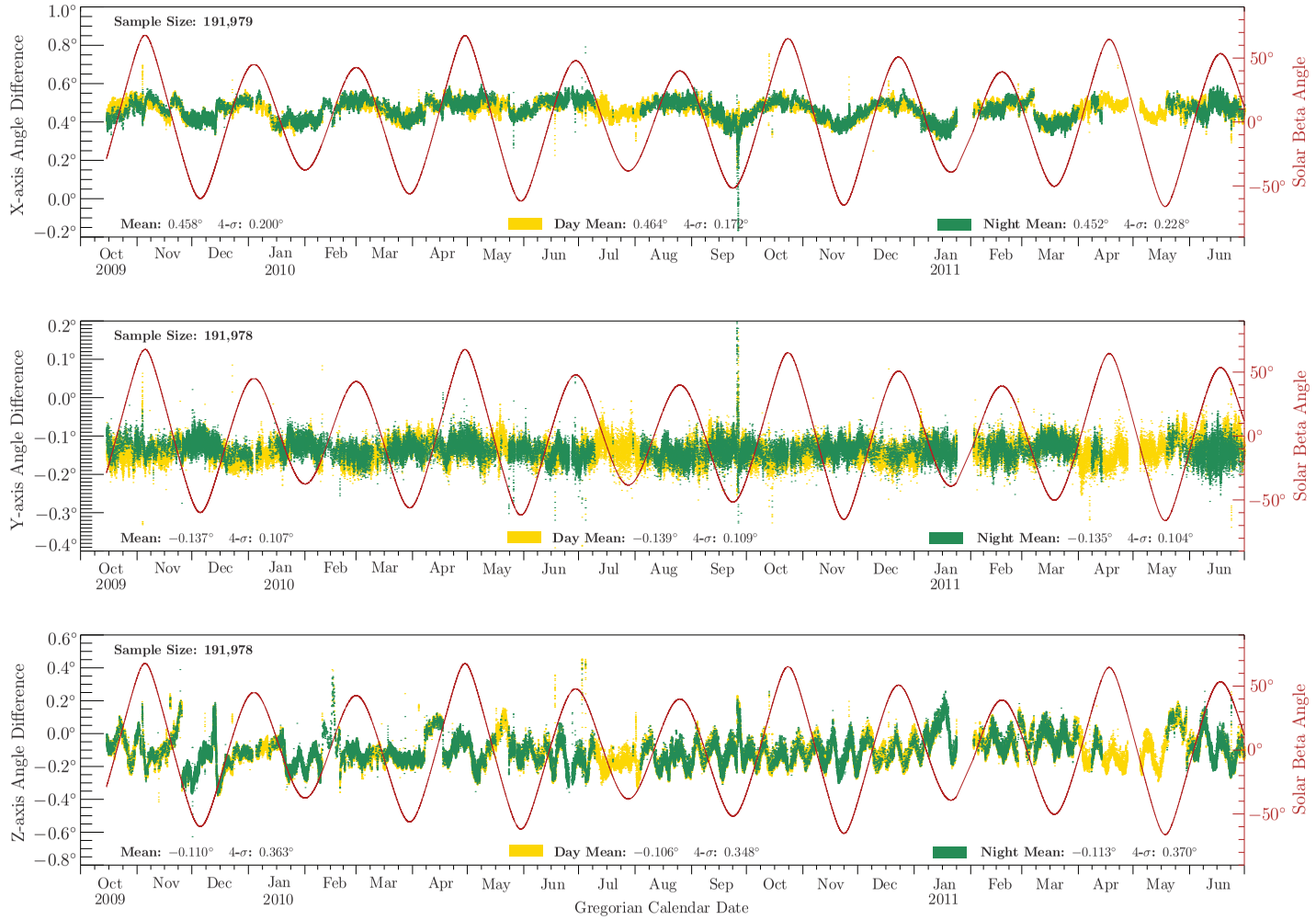


**Figure 9: Comparison of HREP Star Tracker with Reconstructed ISS Attitude.** The X-, Y-, and Z-axis angular differences are separated by day (direct sunlight) and night (solar umbra). The ISS solar beta angle is shown in red.

to the payloads. Later, NASA corrects the coarse attitude into a high-accuracy Reconstructed ISS Attitude data product. To illustrate why attitude determination local to the SAGE III payload is still a necessary substitute for the Reconstructed ISS Attitude in atmospheric retrievals, Figure 9 compares that data set with the HREP star tracker data for nearly two years. The discrepancy between the two data sets, meaning the excursions from the mean biases in each axis between the data sets over the time series, are caused by the difference in location aboard the ISS between the attitude determination systems. Thermal and external torque driven deflections of the ISS structure translate into measured attitude differences. The HREP star tracker was located on the Japanese Experiment Module (JEM) Kibo Exposed Facility, while SAGE III on ELC-4 will be located on the starboard truss segment #3. Figure 9 specifies the mean biases of each axis and the 4-$\sigma$ standard deviations. Correlations with the ISS orbit solar beta angle (depicted in red) can be discerned. The 4-$\sigma$ deviation in the Y-axis would translate to approximately 5 km in altitude at the limb for SAGE III measurements, which would adversely affect the science data product if used for absolute attitude determination.

The Hexapod Mechanical Assembly (HMA) shown in Figure 6 will be used to mitigate the effects of roll and pitch variations up to $\pm 8^{\circ}$ during science events. The instrument communicates with the HMA to position the SA, and the HMA returns the azimuth offset value to the instrument. The instrument assembly scan head accounts for variation in yaw as it has greater than $360^{\circ}$ rotation capability.

Solar occultation measurements are the primary science objective followed by lunar occultations and limb scattering events. If conditions are ideal, a typical orbit can consist of a Sunrise and Sunset, a Moonrise or Moonset, and a limb scatter event (Thornton and Hall, 2013) as shown in Figure 10.

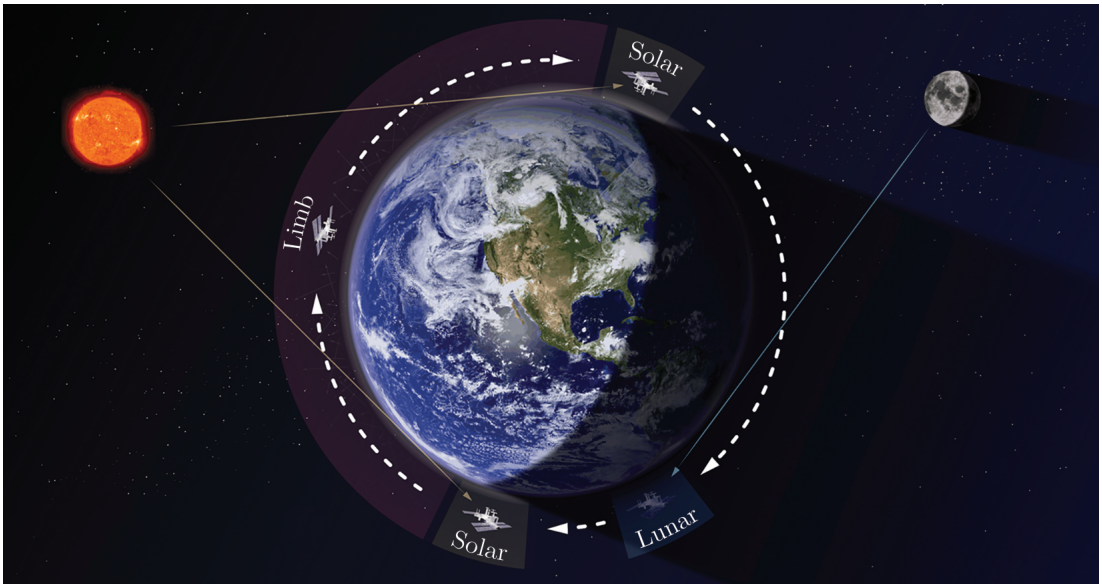


**Figure 10: SAGE III ISS Typical Orbit Operations.** All three science event types may be captured in one orbit.

#### *2.1.2.1 DMP Specifications and Requirements*

A trade study (Cutright, 2011) by the SAGE III ISS Project led to the selection of a Honeywell Miniature Inertial Measurement Unit (MIMU) to be used as the DMP for monitoring the mechanical environment of the payload. The MIMU employs three Honeywell GG1320 Ring Laser Gyroscopes (RLGs) to measure angular rates in three orthogonal axes. RLGs sense rotation rates similar to the Sagnac effect, which is observed in a beam of light that is split and made to travel the same closed path in opposite directions. The beams are then brought back together, and a detector measures their spatial interference pattern. The relative phase shift between the beams at the point of interference corresponds to the angular rotation rate of the apparatus on the sensitive axis. This is because the total path length traveled by the laser light around the ring in one direction will differ from the path length traveled by the counter propagating beam if the ring is rotating around its axis with respect to inertial space. RLGs are configured so that the laser resonance cavity itself forms the ring, and so a frequency shift is observed with rotation rather than a phase

shift because the effective length of the cavity differs depending on the direction of propagation around the ring. This produces two counter propagating lasing modes with frequencies that are increasingly different with greater rotation rates. Instead of a changing spatial interference pattern, the detector measures a beat frequency (temporal interference pattern) between the counter propagating modes. In the case of the three RLGs in the MIMU, each RLG will measure the rotation rate of the SAGE III payload in one axis. The gyros are orthogonal to each other creating a conventional right-handed X-Y-Z coordinate frame by which to measure rotations $\vec{\omega}_X$, $\vec{\omega}_Y$, and $\vec{\omega}_Z$.

To improve measurement accuracy, the SAGE III RLGs use mechanical dither, path length control, and random drift improvement (Armenise et al., 2011). While RLGs may be configured to operate without moving parts, such configurations are generally susceptible to effects that can severely diminish accuracy under certain mechanical conditions, such as occurs when rotation about the sensitive axis is very slow (smaller than about $100^\circ/hr$). In this case, the low rotation rate produces nearly identical frequencies in the two counter propagating laser modes. As with the SAGE III DMP, RLGs typically employ mirrors to establish a closed ring path. Injection locking occurs (in the conduction electrons) at the mirrors when the counter propagating frequencies are sufficiently close, causing the two laser modes to lock together in frequency and the measured rotation rate to be zero. This is referred to as "lock-in" and is similar to mechanical oscillator lock. At very low rotation rates, lock-in will cause the measured total rotation to be zero over an arbitrarily large rotation angle. To prevent lock-in the gyros are mechanically modulated on torsion springs around the ring axis with a peak-to-peak amplitude of about 500 arcseconds. This modulation, called "dither", ensures that the RLGs maintain a minimum angular rate at the center of oscillation to prevent lock-in and is subtracted from the output data in a process called "dither stripping". To reduce sensitivity to noise and improve

stability of gyro bias and scale factor performance, path length control is introduced to ensure maximum laser intensity and prevent laser mode hopping. The mirrors are piezoelectrically driven to control the length of the laser beam path around the gyro. Similarly, random drift improvement drives the mirrors differentially to determine the minimum mode coupling magnitude for the mirrors and controls them to maintain the minimum. Coupling between the laser modes can cause an increase in bias and random drift.

The SAGE III Project requested the implementation of a $2^{nd}$ order Butterworth lowpass digital filter with 100 Hz cutoff to limit higher frequency mechanical noise. The principal frequencies of concern to boresight pointing and hence the science product are 64 Hz and below derived from the instrument sampling rate. An ideal lowpass filter cannot be achieved in practical applications. Butterworth filters, however, provide a desired maximally flat gain and minimal phase shift in the passband below the cutoff frequency (Allred, 2010). The Butterworth digital filter is defined by the transfer function

$$H(z) = \frac{b_0 + b_1 z^{-1} + b_2 z^{-2}}{1 + a_1 z^{-1} + a_2 z^{-2}}. \tag{1}$$

The DMP filter coefficients are in Table 2.

**Table 2: Butterworth Filter Coefficients.** Values of the coefficients used in the DMP $2^{nd}$ order Butterworth filter.

| Coefficient | Value |
|---|---|
| $b_0$ | 0.0329951514 |
| $b_1$ | 0.0659903028 |
| $b_2$ | 0.0329951514 |
| $a_1$ | $-1.3486139865$ |
| $a_2$ | 0.4805945920 |

Two interfaces are used to retrieve data from the DMP: an RS-422 synchronous serial interface transmitted at 200 Hz and a military standard 1553 serial bus transmitted at 1 Hz. The interface adapter module (IAM) on the SAGE III payload stores and packages the DMP data into a telemetry matrix, and then streams the data to

the ISS for downlink to the ground. The telemetry stream consists of built-in test parameters to monitor system status and the compensated gyro angles from the three RLGs. The angles are compensated in software for bias, scale factor, temperature effects, and input axis misalignment or non-orthogonality. This 200 Hz output is the integral of the angular rates measured internally at 1600 Hz by the RLGs and digitally filtered with the above $2^{nd}$ order Butterworth filter. The RLGs output angle instead of rate to provide the end-user with a product that can account for data dropouts. If packet loss occurs the end-user can use the angular position differences to produce a mean rotation rate for the RLG covering the dropout period. Reporting angular rate, on the other hand, does not track how the RLG has rotated prior to the current measurement time period.

During launch vibration loading, the RLG sensor block is expected to move on the internal isolation grommets by up to 15 arcminutes. These grommets mechanically isolate the solid sensor block from the DMP mounting chassis to prevent dither-induced vibrations above 300 Hz from transmitting out to the payload. The sensor block itself is monolithic and will likely maintain the orthogonality of the three RLGs. Therefore, while there is almost no chance that RLG orthogonality will be affected during launch, the final coordinate system orientation of the DMP with respect to the payload will not be precisely known until SAGE III is on orbit and a calibration is completed. Deriving and testing a calibration procedure from simulated payload data is one of the principal drives of this thesis.

#### *2.1.2.2 SAGE III Attitude Measurements*

While there are many subsystems on the SAGE III ISS payload, the three that will be used for attitude determination are the DMP, HMA, and the instrument SA. Their configuration is shown in Figure 6 on page 15. The purpose of the HMA is to control the coarse pointing of the scan head (which is mounted directly on top of the HMA)

to correct for the drifting TEA. With course knowledge of the ISS TEA, the HMA will position the scan head to within 1° of nadir prior to a science event to ensure atmospheric scans are vertical. The SA initially senses the Sun or Moon position with wide-field bicells, and the pointing subsystem azimuth motor and elevation scan mirror control the fine azimuth and elevation pointing to conduct occultation scans. The DMP is positioned in the middle of the HMA directly below the SA.

For producing a simulated data set in the present investigation, the HMA and SA will be considered as one attitude measurement. Specifically, the data will be treated as if the instrument were a Sun position sensor, reporting the attitude of the center of the Sun at the beginning and ending exoatmospheric scan of a given event within a known attitude error. In practice, the Sun centers will be derived from the scan data. See Section 3.1.3 on page 37 for specifications on the simulated SA data. The HMA is a pointing system consisting of six linear actuators. It reports its attitude in telemetry in the form of quaternions, both a commanded quaternion and measured quaternion. This HMA attitude is defined as the HMA upper reference frame rotation (the top ring of the HMA) with respect to the ISS LVLH reference frame (Alenia Spazio, 2005). The SA boresight attitude with respect to the HMA upper reference frame is reported in spherical coordinates, where the elevation and azimuth angles are provided in SA telemetry. To view the HMA/SA system as one measurement the attitudes can be combined as shown in Thornton (2013). This method was used in ground testing during the Sunlook/Moonlook tests, which are outdoor ground tests of the instrument's solar and lunar measurements. In this test setup the Hexapod had not yet been integrated into the payload, so an external motor was used for coarse pointing.

When the DMP is mounted to the ExPA, the orientation of the measurement coordinate system with respect to the HMA/SA coordinate system will be known.

**Table 3: Measurement Accuracy.** A summary of the measurement accuracies for each subsystem that provides attitude measurements.

| Subsystem | Measurement | Type | Accuracy |
|---|---|---|---|
| SA | Scan Mirror Elevation Position | elevation angle | 12 arcseconds $3\sigma$ |
| | Scan Head Azimuth Position | azimuth angle | 6 arcminutes $3\sigma$ |
| HMA | Mechanical Accuracy | quaternion | $\pm 0.25^{\circ}$ |
| | Knowledge of Attitude | quaternion | $\pm 1$ arcminute |
| DMP | RLG Attitude | angle random walk | X-axis 0.005 $deg/\sqrt{hr}$ $1\sigma$<br>Y-axis 0.005 $deg/\sqrt{hr}$ $1\sigma$<br>Z-axis 0.005 $deg/\sqrt{hr}$ $1\sigma$ |

However, after being subjected to launch vibration loading, the DMP RLGs are expected to change orientation as the internal isolation grommets slip (as previously described at the end of Section 2.1.2.1).

The accuracy for each of the attitude measurements is described in Table 3 with SA information from Hill (2014) and Ball Aerospace & Technologies Corp. (2012), HMA from Alenia Spazio (1998), and DMP from Honeywell International Inc. (2010). Telemetry for the three subsystems will be downlinked daily on orbit from the solid state memory card (SSMC) in the IAM. The data rates for the three subsystems vary. The DMP reports science data at both 200 Hz and 1 Hz. The instrument control electronics (ICE) reports instrument science data at 64 Hz and health and status at 1 Hz. The HMA reports data only at 1 Hz. Therefore, when performing coordinate transformations and filtering (to be discussed in complete detail in Chapter 3), interpolations will be used. On orbit the 64 Hz data will be used for the SA since science events are the data portions of interest. The 200 Hz DMP data can be interpolated to find a corresponding attitude for each 64 Hz science packet. Ideally the HMA position reported at 1 Hz will be used for all 64 science packets for that second. HMA data

stability is assumed because the HMA will not move during a science event. Once it is commanded to a position just prior to a science event, that position is held until the event is completed.

## *2.2 Attitude Determination*

Attitude determination and control (also known as guidance, navigation, and control) is a well-recognized engineering discipline in space exploration and space science. Generally making use of two types of systems, sensors and actuators, the objective is to determine and correct spacecraft orientation based on mission objectives. In the case of SAGE III ISS the space station exercises an attitude control system without regard to the science needs of SAGE III. Although the ISS orbits in the TEA a majority of the time, even in this orientation it is unknown at the ELC-4 location how much mechanical disturbance and external torque-induced deflection will be observed. There are many possibilities for disturbances (energized ISS bending modes, crew movement, docking events, etc.) that cannot be known prior to the installation of SAGE III. Therefore, relative attitude determination (for post analysis disturbance corrections to the solar and lunar occultation scan rates) and absolute attitude determination (for limb scattering) will be employed at the site of the SAGE III payload using the sensors available. However, there will be no active feedback control aspect to the system during science events because the payload does not have a full attitude sensor/actuator control loop. While the HMA is in fact a set of attitude control actuators, it is not used as part of an active attitude sensor/actuator control loop during science events.

A brief overview of the coordinate transformation methods and parameterizations is adapted from Wertz (1978). The three most common attitude representations are the direction cosine matrix (DCM), Euler angles, and quaternions. The DCM defines a rotation between two coordinate systems as represented in Equation 2,

where $\boldsymbol{C}_{ij} = \hat{\boldsymbol{u}}_i \cdot \hat{\boldsymbol{a}}_j$, the cosine of the angle between unit vectors $\hat{\boldsymbol{u}}_i$ and $\hat{\boldsymbol{a}}_j$. The orthonormal basis of a rotated coordinate system is formed by $\hat{\boldsymbol{u}}_1$, $\hat{\boldsymbol{u}}_2$, and $\hat{\boldsymbol{u}}_3$, while $\hat{\boldsymbol{a}}_1$, $\hat{\boldsymbol{a}}_2$, and $\hat{\boldsymbol{a}}_3$ form the unrotated orthonormal basis.

$$\begin{bmatrix} \hat{\boldsymbol{u}}_1 \\ \hat{\boldsymbol{u}}_2 \\ \hat{\boldsymbol{u}}_3 \end{bmatrix} = \begin{bmatrix} C_{11} & C_{12} & C_{13} \\ C_{21} & C_{22} & C_{23} \\ C_{31} & C_{32} & C_{33} \end{bmatrix} \begin{bmatrix} \hat{\boldsymbol{a}}_1 \\ \hat{\boldsymbol{a}}_2 \\ \hat{\boldsymbol{a}}_3 \end{bmatrix}. \tag{2}$$

In most cases the matrix $\boldsymbol{C}_{ij}$ is orthonormal because the two sets of unit basis vectors are orthogonal.

Euler angles are perhaps the simplest parameterization to visualize because there is a more intuitive physical interpretation of yaw, pitch, and roll. A single sequence of three elemental rotations about moving coordinate axes is sufficient to define the rotation of one coordinate system to another using Euler angles. Twelve sequences of three elemental rotations exist for both extrinsic (fixed coordinate system) and intrinsic (rotating coordinate system, such as yaw-pitch-roll) rotations. An example of a 3-1-3 or $z$-$x$-$z$ sequence is shown in Equation 3.

$$\boldsymbol{A}_{313}(\phi, \theta, \psi) = \begin{bmatrix} \cos\phi & \sin\phi & 0 \\ -\sin\phi & \cos\phi & 0 \\ 0 & 0 & 1 \end{bmatrix} \begin{bmatrix} 1 & 0 & 0 \\ 0 & \cos\theta & \sin\theta \\ 0 & -\sin\theta & \cos\theta \end{bmatrix} \begin{bmatrix} \cos\psi & \sin\psi & 0 \\ -\sin\psi & \cos\psi & 0 \\ 0 & 0 & 1 \end{bmatrix}. \tag{3}$$

This transformation represents first a rotation of coordinate axes about the $z$-axis by angle $\psi \in [-\pi, \pi]$, followed by a rotation about the resulting $x$-axis by angle $\theta \in [0, \pi]$, and finishes with a rotation about the resulting $z$-axis by angle $\phi \in [-\pi, \pi]$. The leading disadvantage to any Euler angle sequence is the loss of a rotational degree of freedom when one of the Euler angles reaches a critical value. For example, when $\theta \to 0$ in the above sequence, the center rotation matrix is the identity matrix. The first rotation $\psi$ in this sequence leaves the $z$-axis unchanged, the second rotation is the identity matrix, and the third rotation $\phi$ is yet another rotation around the $z$-axis. Therefore, when $\theta \to 0$, the rotation axis locks to the $z$-axis and both $\psi$ and $\phi$

represent the same rotational degree of freedom around $z$. The rotational degree of freedom around $y$ is lost. This can be seen by setting $\theta = 0$, multiplying the two $z$ rotations, and recalling the sum and difference trigonometric identities for sine and cosine. The transformation at $\theta = 0$ becomes

$$\boldsymbol{A}_{313}(\phi, 0, \psi) = \begin{bmatrix} \cos(\phi + \psi) & \sin(\phi + \psi) & 0 \\ -\sin(\phi + \psi) & \cos(\phi + \psi) & 0 \\ 0 & 0 & 1 \end{bmatrix}. \tag{4}$$

This condition, a rotation around the initial $z$-axis by angle $\phi + \psi$, corresponds to the polar degeneracy that leads to rotational Gimbal lock, or the loss of the third degree of freedom in an attitude control system that employs Euler angles. Another example of this singularity in a yaw-pitch-roll (3-2-1) rotation sequence is when pitch $\rightarrow$ 90°. In this case, the rotated $x$-axis takes the place of the original $z$-axis, and the yaw and roll represent the same degree of freedom—namely the orientation of the coordinate system in space about the newly rotated $x$-axis.

Euler symmetric parameters, commonly referred to as quaternions, have some advantages over Euler angles. There are no trigonometric functions to reduce computational speed, no degeneracies that limit rotational degrees of freedom, and there is a convenient product rule for successive rotations. William Rowan Hamilton discovered quaternions in 1843 while searching for a way to multiply triples in an attempt to define points in three-dimensional space with a hypercomplex representation. Instead, he found a method (Hamilton, 1844) to multiply unit quadruples $q = q_0 + q_1\boldsymbol{i} + q_2\boldsymbol{j} + q_3\boldsymbol{k} = q_0 + \boldsymbol{q}$ to represent rotations based on the hypercomplex multiplication rules in Equation 5.

$$\boldsymbol{i}^2 = \boldsymbol{j}^2 = \boldsymbol{k}^2 = \boldsymbol{ijk} = -1. \tag{5}$$

This four-dimensional representation of three-dimensional rotations is an extension of the complex numbers. Quaternions are composed of a scalar $q_0$ and a three-vector $\boldsymbol{q}$

(with components $q_1$, $q_2$, and $q_3$). These four components are mapped to a complex number with three imaginary parts, or a hypercomplex number of rank 4. The additional topological dimension adds a degree of freedom that actually avoids the Gimbal lock degeneracy described previously. A caveat of the quaternion representation as will be seen shortly is that unit quaternions are a double-cover of the three dimensional rotations, meaning there exist two distinct quaternion rotation operators to describe every unique rotation in three dimensional space. This topology complicates some forms of computation, such as finding mean quaternions and derivatives.

All of the quaternion complex number multiplication rules can be derived from Equation 5. For example, to find $\boldsymbol{jk}$, take $\boldsymbol{ijk} = -1$ from Equation 5 and multiply on the left by $\boldsymbol{i}$. This yields $-\boldsymbol{jk} = -\boldsymbol{i}$ or $\boldsymbol{jk} = \boldsymbol{i}$. Note that these multiplication rules are not commutative. For example, $\boldsymbol{kj} = -\boldsymbol{i}$.

Unit quaternions are quaternions with norm $|q| \equiv \sqrt{q_0^2 + q_1^2 + q_2^2 + q_3^2} = 1$. Unit quaternions can be described by the Euler rotation angle $\Phi$ and the Euler rotational axis $\hat{\boldsymbol{e}}$ as shown in Equations 6 and 7. With a known Euler angle and axis, quaternions can be defined by Equation 8.

$$\hat{\boldsymbol{e}} = \frac{1}{2\sin\Phi}(\boldsymbol{A}^T - \boldsymbol{A}). \tag{6}$$

$$\cos\Phi = \frac{1}{2}[Tr(\boldsymbol{A}) - 1]. \tag{7}$$

$$q = \begin{bmatrix} q_0 \\ q_1 \\ q_2 \\ q_3 \end{bmatrix} = \begin{bmatrix} q_0 \\ \boldsymbol{q} \end{bmatrix} = \begin{bmatrix} \cos\frac{\Phi}{2} \\ \hat{\boldsymbol{e}}\sin\frac{\Phi}{2} \end{bmatrix}. \tag{8}$$

Note that for the rotation represented by a given quaternion, the direction of the axis of rotation $\hat{\boldsymbol{e}}$ is captured in the vector portion $\boldsymbol{q} = \hat{\boldsymbol{e}}\sin\frac{\Phi}{2}$, and the right-handed angle of rotation $\Phi$ around axis $\hat{\boldsymbol{e}}$ is captured in the scalar portion $q_0 = \cos\frac{\Phi}{2}$. (The $\sin\frac{\Phi}{2}$ constant term in the vector portion just serves to reduce the length of axis $\hat{\boldsymbol{e}}$

to normalize the quaternion when the scalar portion is added in quadrature with the vector portion. Multiplication by $\sin\frac{\Phi}{2}$ does not change the direction of the rotation axis.) Quaternion normalization is of particular importance in practical applications because unit quaternions are used to implement length-preserving rotations to three-vectors, and the set of all unit quaternions forms a double cover to the special orthogonal group $SO(3)$ of rotation matrices. Quaternion normalization should occur regularly during analysis to minimize creep from computational round-off error. The optimal method to normalize quaternions when computational error has been evenly partitioned among the four components as derived in Bar-Itzhack (1971) and Giardina et al. (1975) is

$$\hat{q} = \frac{q_0 + q_1\boldsymbol{i} + q_2\boldsymbol{j} + q_3\boldsymbol{k}}{\sqrt{q_0^2 + q_1^2 + q_2^2 + q_3^2}}. \tag{9}$$

In general, normalization by Equation 9 will not preserve the angle of rotation, although it will preserve the direction of the rotation axis. In some cases, the rotation angle will be precisely known, and normalizations to minimize computational round-off error will be applied to the length of the rotation axis only to preserve the angle. Note that for quaternion conjugate $q^* = q_0 - \boldsymbol{q}$ the norm of quaternion $|q| = \sqrt{qq^*} = \sqrt{q^*q} = \sqrt{q_0^2 + q_1^2 + q_2^2 + q_3^2}$. For the set of unit quaternions, the quaternion inverse $q^{-1}$ is equal to the quaternion conjugate $q^*$.

Multiplication of quaternions is not commutative, therefore quaternions form a non-commutative division ring (Kuipers, 1999). Quaternion multiplication is defined in Equation 10 where the dot and cross products retain their vector definitions.

$$pq = p_0q_0 - \boldsymbol{p}\cdot\boldsymbol{q} + p_0\boldsymbol{q} + q_0\boldsymbol{p} + \boldsymbol{p}\times\boldsymbol{q}. \tag{10}$$

Now that quaternions and their multiplication have been defined, sequences of quaternion rotation will be discussed. Quaternion rotation is defined as

$$\boldsymbol{a} = q\boldsymbol{b}q^*, \tag{11}$$

where the pre-rotated vector $\boldsymbol{b}$ is represented by the pure quaternion (scalar part equal to zero) in the multiplication sequence, and $q^*$ is the inverse or conjugate of unit rotation quaternion $q$. The rotated vector is represented by pure quaternion $\boldsymbol{a}$. Successive rotations are represented by quaternion multiplication. For example, a rotation $q$ applied to vector $\boldsymbol{b}$ followed by a second rotation $p$ applied to the result of $q$ is defined as

$$\boldsymbol{c} = p(q\boldsymbol{b}q^*)p^* = (pq)\boldsymbol{b}(pq)^*. \tag{12}$$

This is equivalent to applying $pq$ to $\boldsymbol{b}$ using quaternion multiplication rules.

To perform statistical analyses of the efficacy of methods in this thesis to find coordinate transformation quaternions, the mean of a sample of derived quaternions must be computed. Quaternion averaging cannot be performed in a conventional manner. There are two problems that prevent the traditional vector average from working correctly for quaternions. First, the resulting average quaternion would not in general be a unit quaternion, meaning not a length-preserving rotation. Second, as asserted earlier, the unit quaternions form a double cover of the space of three dimensional rotations. Note that quaternions $-q$ and $q$ represent the same rotation since $(-q)\boldsymbol{b}(-q^*) = q\boldsymbol{b}q^*$. The unit quaternions are therefore topologically distinct from the real number system. Because $q$ and $-q$ will define the same rotation, they should have the same effect on an average rather than averaging to zero. Accounting for quaternion topology to derive an average quaternion is well treated in Markley et al. (2007). The matrix $\boldsymbol{M}$ is found by

$$\boldsymbol{M} \equiv \sum_{i=1}^{n} w_i q_i^T q_i, \tag{13}$$

where $w_i$ is an optional weighting factor for each quaternion $q_i$ in the mean. The eigenvector corresponding to the maximum eigenvalue of $\boldsymbol{M}$ is the average quaternion.

Attitude measurements come in many forms. They can have different coordinate

systems and can be expressed in any of the parameterizations described above. Conversion between the direction cosine matrix, Euler angles, and quaternions exist and will be applied in this research when necessary. Quaternions will be extensively used for this thesis research and in the derivations that follow.

# CHAPTER III

# METHODOLOGY

## *3.1 Simulated Data*

High fidelity simulation is essential to robust vetting of the coordinate transformation and attitude determination algorithms before the SAGE III ISS launch. Modeling the behavior of the relevant subsystems is a complicated process that involves data from the Houston Operations Support Center (HOSC), documentation provided on the SA, Hexapod, and DMP, and ISS orbit and attitude modeling in Systems Tool Kit (STK). Simulations are performed to explore algorithmic error bars and sensitivities and to streamline the computation process. The goal is to provide a finished process that can be readily used when SAGE III is on orbit.

Several software programs and programming languages are utilized to simulate the relevant SAGE III data. Matrix Laboratory (MATLAB), produced by MathWorks, Inc. of Natick, Massachusetts, is used extensively to calculate the coordinate transformations and the attitude filter. MATLAB is an ideal platform for these computations since it was created for efficiency in matrix operations. The ISS orbit and attitude are modeled by STK along with data from CelesTrak, both of which are products of Analytical Graphics, Inc. of Exton, Pennsylvania. CelesTrak is managed by Dr. T.S. Kelso through the Center for Space Standards & Innovation (CSSI), a research arm of Analytical Graphics, Inc. that provides orbital element data sets for propagators. Python and awk are used to read and convert data files for portability between analysis tools, such as STK to MATLAB. All software products developed during the course of this research are controlled under the Apache Subversion revisioning and version control system in accordance with software best practices.

### 3.1.1 Broadcast Ancillary Data

To simulate ISS attitudes, realistic attitude data are obtained and converted to STK attitude files. ISS reports Broadcast Ancillary Data (BAD) detailing station vehicle information including location, attitude, and environmental states. On orbit the BAD packets are sent to all payloads via MIL-STD-1553. The historical data sets are ideal for use in simulation because they represent actual, measured attitudes and attitude rates from a given platform aboard ISS. As explained in detail in Section 2.1.2 with reference to Figure 9 on page 18, these data cannot be used to discern SAGE III payload attitudes on orbit to the precision needed by the science retrieval algorithm because of significant and uncharacterized internal bending degrees of freedom of the ISS structure. The HREP example in Chapter 2 illustrates the significant, time varying deviations between the HREP star tracker and the Reconstructed ISS Attitude caused by ISS bending modes. On orbit the DMP will support SAGE III attitude determination as it is directly mounted to the payload. But for purposes of simulating the expected DMP and SA data, the BAD is the most representative ISS attitude product available. There are two forms of BAD distinguished by Application Identifier (APID). The 10 Hz packet with APID 2000 is transmitted to all the payloads on station. In addition, a 1 Hz version of the BAD with APID 1074 is sent to the ground.

BAD with APID 1074 is available to ISS payload personnel by request via the HOSC using their secure Enhanced HOSC System (EHS) web interface. The binary packets for the specified time period are transferred via File Transfer Protocol (FTP). To simulate the packets that will be received by the SAGE III payload, the binary format is converted to resemble the on-orbit APID 2000 packet. Once this has been completed, the BAD attitude data are exported to the STK attitude file format. A Python program was developed to pull the LVLH attitude quaternions from the binary packets and arrange them in an STK-readable American Standard Code for

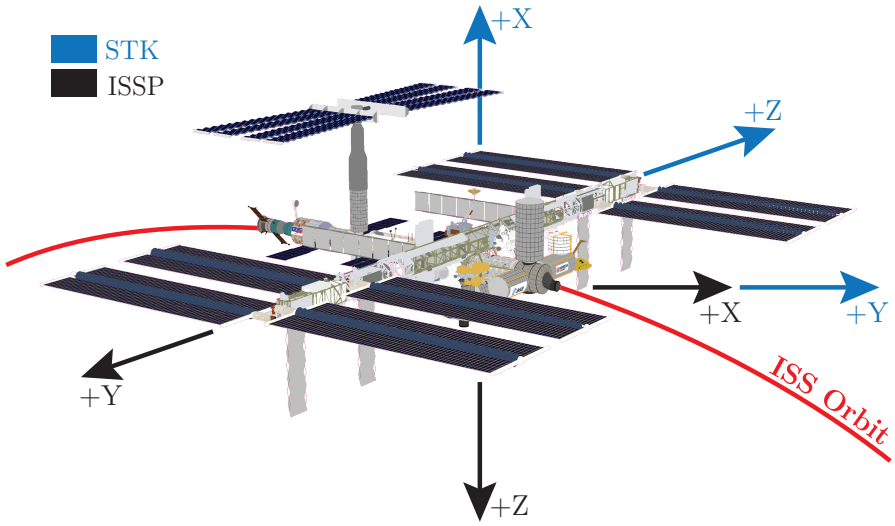


**Figure 11: ISS Axes Definitions.** The ISSP defined custom axes are a rotation of the STK LVLH default. The ISSP X-axis is coincident with the LVLH Y-axis, the ISSP Y-axis is in the opposite direction of the LVLH Z-axis, and the ISSP Z-axis is in the opposite direction of the LVLH X-axis.

Information Interchange (ASCII) attitude file. The ISS LVLH coordinate system is depicted in Figure 7 on page 16 and described in Section 2.1.2. To apply BAD to the ISS satellite in STK a custom set of axes is necessary to rotate the predefined ISS body axes to match the International Space Station Program (ISSP) definition. Both sets of axes are shown in Figure 11 with the STK LVLH default in blue and the custom axes derived from the ISSP definition in black. For the purposes of this simulation BAD were obtained for the time period 2 February 2014 through 6 April 2014.

### 3.1.2 Simulating the ISS Orbit

Converting the high fidelity attitude data from BAD and utilizing it in STK is computationally and procedurally intensive. Creating and using STK-readable orbital ephemerides from BAD would be equally complex and time consuming but would lack any benefit for attitude simulation in comparison to more typical and less time consuming method of orbit propagation. North American Aerospace Defense Command (NORAD) two-line element (TLE) sets are obtained from CelesTrak at

http://celestrak.com/ to determine the orbital position of the ISS for the analysis time period. TLEs define the six Keplerian orbital elements at an epoch time: eccentricity, inclination, mean anomaly, argument of perigee, right ascension of the ascending node, and mean motion. The TLE data are imported into STK. Perturbations from the classical Keplerian (or osculating) orbits are not captured within any individual TLE set. To model perturbations from both gravitational asymmetries and drag forcing it is essential to choose an accurate propagator empirically tuned to the orbital regime. The Simplified General Perturbations 4 (SGP4) propagator is used to propagate ephemerides for objects and spacecraft in Low Earth Orbit (LEO) with an error of approximately 1 km at epoch. SGP4 provides the high fidelity orbital perturbations that are more than sufficient for this simulation.

ISS Solar beta angle, or the signed angle between the ISS osculating orbital plane and the vector to the Sun, has a significant influence on the SAGE III mission. Science events cannot be performed at beta angles less than $-60°$ or greater than $+60°$ because of the stratospheric homogeneity assumption used in the post-processing science inversion algorithm. Stratospheric occultation measurements that remain within a small latitude band during a single science event are altitude layer homogeneous because the stratosphere has a high degree of zonal homogeneity. The problem at more extreme beta angles occurs when SAGE III tracks the Sun slowly over the course of a single event as it rises or sets through a large variation in tangent point latitudes. In this case, the assumption of altitude layer homogeneity in the stratosphere is not valid, and the science retrieval is poor. Therefore, the simulated data sets were generated over a full beta cycle within the beta angle constraints to see if and how measurements differ over the full beta angle range. As shown in Figure 12 the time period of 2 February 2014 through 6 April 2014 covers a beta angle range of approximately $-59.0°$ to $58.8°$. The data from this time period will be the focus of the simulations.

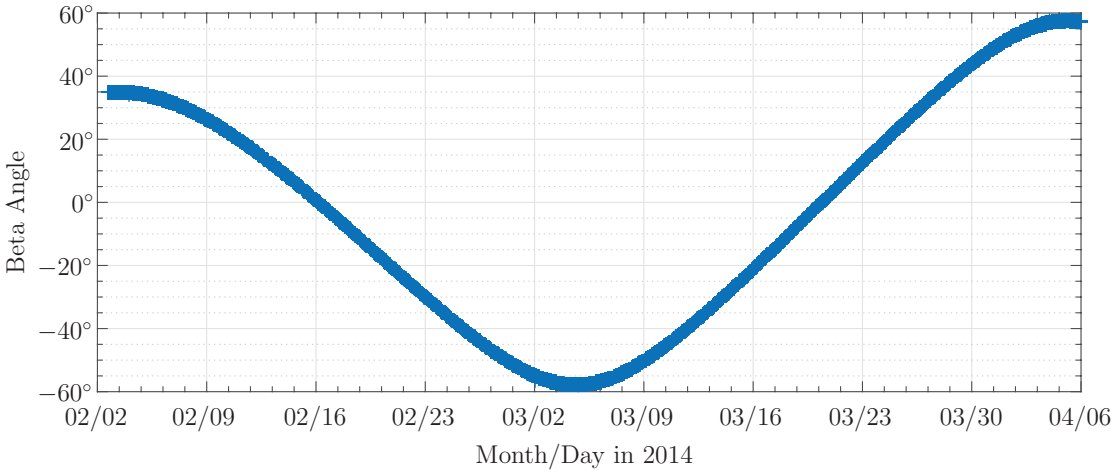


**Figure 12: ISS Beta Angle.** Shown is the range of beta angles over the chosen time period of simulated ISS data.

### 3.1.3 Modeling the SA in STK

The SA is modeled as a sensor attached to the ISS object in STK. The SA pointing subsystem azimuth resolver data are simulated at the same rate and precision as SAGE III will provide on orbit. The elevation resolver data track the center of the Sun unlike the vertical boresight scanning that happens on orbit. Since only two Sun vectors are used during each occultation measurement to derive the DMP-to-SA coordinate transformation, one near the beginning of the exoatmospheric scan series and one near the end, it is assumed that the position of the center of the Sun will be extracted from the scan data to construct these vectors. Avoiding unnecessary complexity, the STK sensor object specifications are as follows:

- Located at the center of mass of ISS
- Simple conic with half angle of 1°
- Tracking the Sun in "Receive" mode to correct for the speed of light
- Grazing altitude access constraint of 100 km to 280 km

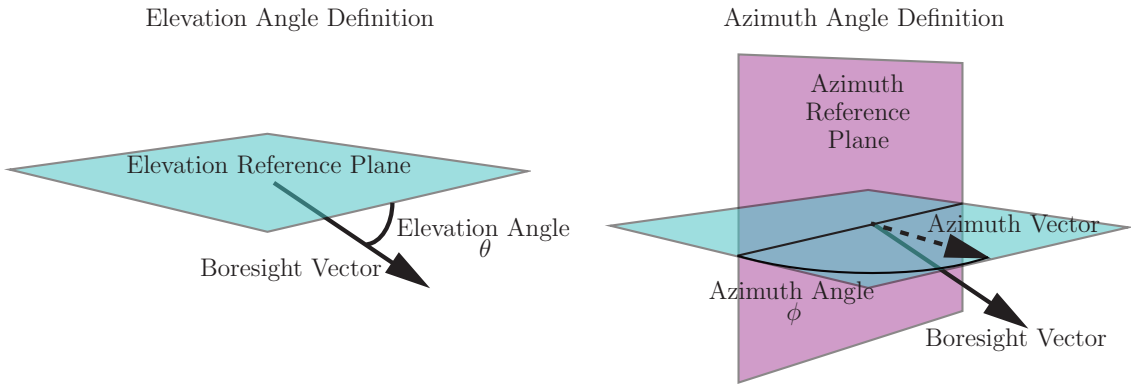


**Figure 13: STK Azimuth and Elevation Angle Definitions.** The simulated SA boresight azimuth and elevation are measured with respect to ISS body reference planes in STK.

The grazing altitude access constraint was initially modeled as 0 km to 280 km, however, on-orbit Sun measurements lower than 100 km begin to introduce an excursion of the apparent Sun position from its inertial position because of atmospheric refraction, which is not ideal for correlation with the DMP. Because exoatmospheric measurements will be used on orbit to track rotation in inertial space, the simulated data reflect this.

As discussed in Chapter 2, the SA provides a boresight azimuth and elevation angle for each Sun center measurement. In STK these two angles are referenced to the SAGE III sensor object as follows. As shown in Figure 13, the azimuth reference plane is defined as the plane normal to the ISSP body Y-axis. The elevation reference plane is defined as the plane normal to the ISSP body Z-axis. Because these planes are defined by body axes, they will rotate with ISS attitude changes. Both planes pass through the center of ISS and serve as reference planes to the actual azimuth and elevation motions of the SA boresight. The elevation angle is defined as the angle between the boresight vector and the elevation reference plane (i.e., the plane of 0° elevation) with positive elevations opposite the direction of the ISSP body +Z-axis. The boresight azimuth reference vector is a projection of the boresight vector into the

elevation plane. The azimuth angle $\phi$ is then the angle between the azimuth reference vector and the azimuth reference plane, with 0° azimuth mapped to the ISSP +X-axis ram direction. STK always reports the smallest signed angle between a vector and a plane. To map this angle into an azimuth range of $[-180°, 180°]$, an "azimuth sign angle" was defined as the angle between the ISSP body +X-axis and the projection of the boresight vector into the azimuth reference plane. The azimuth sign angle is used to correct the azimuth angle in MATLAB using the logic in Table 4.

**Table 4: Azimuth Correction Logic Table.** The STK azimuth angle is mapped into the range $[-180°, 180°]$ using the azimuth sign angle.

| Azimuth Sign Angle (°) | STK Azimuth Angle $\phi$ (°) | Correction Applied |
|---|---|---|
| $> 90$ | $> 0$ | $\phi \rightarrow 180° - \phi$ |
| $> 90$ | $< 0$ | $\phi \rightarrow -180° - \phi$ |
| $< 90$ | $> 0$ | None |
| $< 90$ | $< 0$ | None |

The STK report generation tool is used to extract simulated azimuth and elevation data from the SAGE III sensor. Figure 14 illustrates a simulated Sun sensor during a science event. This was achieved by importing ISS TLE into STK and using the SGP4 propagator as described above. The STK output file reports solar acquisition data consisting of azimuth and elevation angles in degrees at 64 Hz closely simulating SA on-orbit data during science events. Only solar events are simulated in STK. Limb scattering events cannot be used to derive a coordinate transformation because no reference is being tracked by the SA scan head. The scan head tracks the Moon during lunar occultation events, but the apparent position of the Moon deviates much faster from the inertial stars or International Celestial Reference Frame (ICRF) than the Sun. The orbital period of the Moon is $\approx 27.3$ days, while it takes the Sun $\approx 365.25$ days to move through the zodiac. Inherently inferior to the Sun as an inertial reference point, the Moon position is also more difficult for the SA to accurately track. The elevation angle registration of the center of the Moon is expected to be

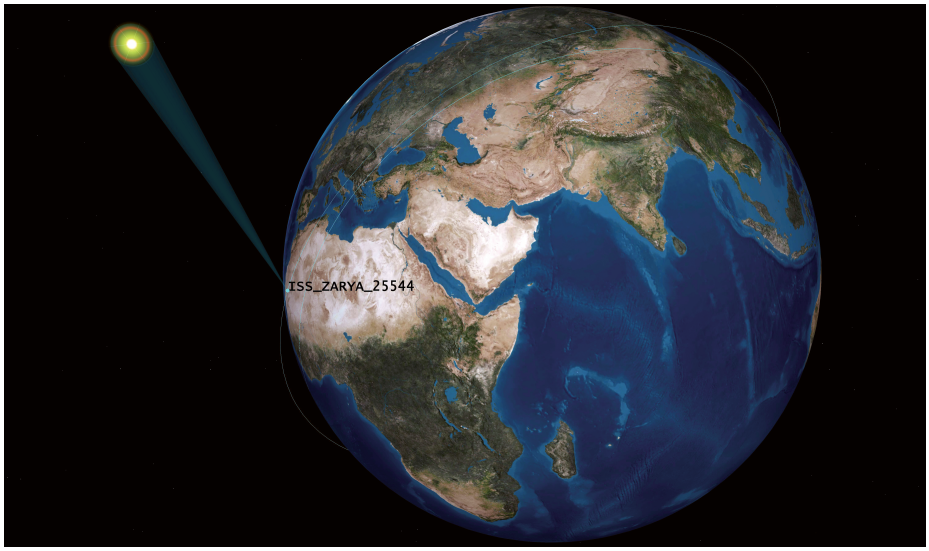


**Figure 14: STK SA Simulation.** SAGE III solar occultation events are simulated for ISS with date-specific, SGP4-propagated orbits and date-specific, high-fidelity BAD attitudes.

comparatively poor because of the highly nonuniform reflectivity of the lunar surface and the changing phase. Although the Sun is not a perfect inertial reference, the Moon would contribute error to the coordinate transformation analysis without improving the variation in orientation of the ISS rotation axis. (See Sections 3.2.3.1 and 4.2 for a treatment of the apparent motion of the Sun with respect to the fixed stars during an occultation event.) The SAGE III Project expects to only examine solar events on orbit for DMP coordinate system calibration, and therefore solar simulation is sufficient. Data files are generated for each day of the approximately two month period of the chosen beta cycle shown in Figure 12.

### 3.1.4 Modeling the DMP in STK

DMP data are reported as the angle of rotation about each of three axes. A MIMU natively measures change in position, but rates measured in the DMP RLGs are internally integrated over time to output position. It is most convenient to simulate the data in their original form, and thus the data are generated as a rate. To replicate DMP data in STK it is necessary to choose a coordinate frame and

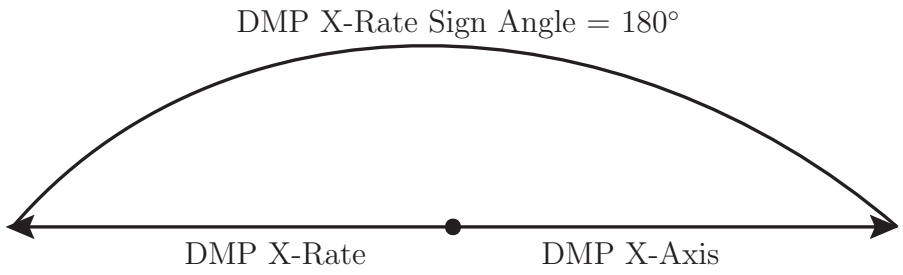


**Figure 15: STK DMP Simulation.** The DMP orthogonal X-axis, X-rate, and X-rate sign angle are shown on 3 February 2014.

calculate the rate around each DMP axis. Several DMP coordinate frames were constructed: an orthogonal frame to match the expected condition on orbit, a slightly non-orthogonal frame, and a largely non-orthogonal coordinate frame. The basis vectors of the orthogonal coordinate frame are defined with respect to the ISS body frame as [1, 0, 0], [0, 1, 0], and [0, 0, 1] for X, Y, and Z, respectively. Similarly, the slightly non-orthogonal frame is defined as [0.99999995769203, 0.00020568902198, 0.00020568902198], [0.00020568902198, 0.99999995769203, 0.00020568902198], and [0.00020568902198, 0.00020568902198, 0.99999995769203] for X, Y, and Z, respectively. The frame with large non-orthogonality is defined as [1, 0.02, 0.01], [0.02, 1, 0.02], and [0.03, 0.01, 1] for X, Y, and Z, respectively. These selections of DMP coordinate frames are explained in Section 4.4.7. Since the DMP RLGs will be subjected to mechanical launch loading, there is a minor possibility of RLG displacements on the sensor block that could manifest as coordinate system non-orthogonality, so the additional coordinate frames are included in simulation to test the consequences and manifestations of such a condition. It should be noted that guidance from DMP manufacturer Honeywell asserts that loss of RLG orthogonality is not expected and has not been exhibited in past deployments of this model of MIMU. Nevertheless, the SAGE III Project prefers to understand how axis non-orthogonality would manifest.

The rate of rotation around each axis is defined as the projection of the angular velocity vector along the direction of the defined DMP axes. Both the rate and axis definition for nominal DMP X are shown in Figure 15.

STK generated DMP output consists of X-, Y-, and Z-rates (as described above) at a data rate of 200 Hz. These data capture the orbital motion of the ISS and the attitude perturbations introduced by the BAD. Because of the high data rate, data are not generated for every day of the two month time period as is done for the SA. Data are generated for 24 hour periods, and they are strategically chosen to represent high, low, and mid beta angles in addition to off nominal ISS orientations and operational rotations. A summary of STK generated DMP data is provided in Table 5.

**Table 5: STK DMP Data Generation.** Shown is a summary of the dates, beta angles, and ISS orientations used to generate DMP data.

| Date (UTCG) | Beta Angle Range (°) | ISS Orientation |
|---|---|---|
| 2 February 2014 | 34.62 – 35.03 | Rotating ≈ 180° around Z-axis |
| 5 February 2014 | 34.15 – 32.90 | Average TEA, then rotating ≈ 90° around Z-axis at the end of day |
| 8 February 2014 | 28.94 – 26.33 | Average TEA |
| 12 February 2014 | 16.58 – 12.86 | Average TEA |
| 14 February 2014 | 8.91 – 4.85 | Average TEA |
| 16 February 2014 | 0.66 – -3.63 | Average TEA |
| 23 February 2014 | -29.97 – -34.23 | Average TEA |
| 5 March 2014 | -57.83 – -57.08 | Average TEA |
| 9 March 2014 | -50.28 – -46.90 | Average TEA |
| 12 March 2014 | -39.08 – -34.82 | Average TEA |
| 20 March 2014 | -1.94 – 2.90 | Average TEA |
| 25 March 2014 | 22.05 – 26.68 | Rotating ≈ 180° around Z-axis |
| 27 March 2014 | 31.21 – 35.59 | Oriented ≈ 180° around Z-axis |
| 4 April 2014 | 57.00 – 57.58 | Average TEA |
| 5 April 2014 | 57.57 – 57.27 | Average TEA |

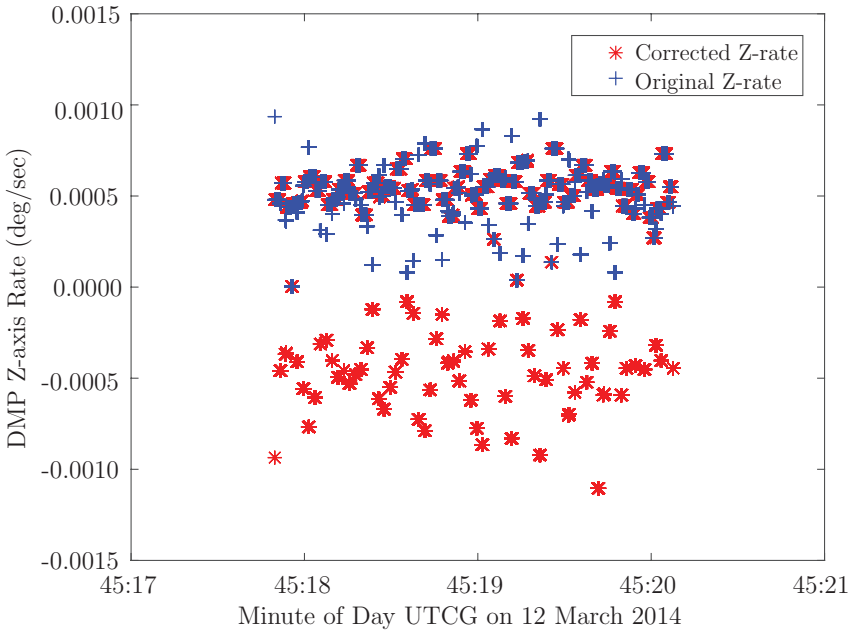


**Figure 16: DMP Rate Correction.** DMP Z-rate corrected for direction.

STK outputs unsigned rates when projected onto body axes. To generate flight-like DMP data the simulated STK rate magnitudes require a direction correction. The angle between the defined DMP axis of rotation and the rate vector (shown in Figure 15 as DMP X-Rate Sign Angle) contains the necessary information regarding the sign of rotation that the DMP would measure on orbit. This angle is either 0° or 180°. The direction correction is shown in Figure 16. This correction is applied in MATLAB.

Extensive ground testing has been performed with the DMP flight unit. Major assessments included acceptance, environmental, and integrated payload testing. The top half of Figure 17 depicts the typical rotation angles (internally integrated from rate) experienced by the DMP while sitting stationary during a functional test at KSC in May 2016. The mean averaged total rotation measured by the DMP for this test is $7.375 \times 10^{-5}$ radians per second (Johnson, 2016). This compares closely ($\approx$1.14% difference) to the yearly mean sidereal rate of rotation of the Earth of $7.292 \times 10^{-5}$

radians per second. The bottom half of Figure 17 shows simulated data (generated as described above) showing a day of nominal TEA. The simulated data are capturing orbital and tumbling motions as opposed to the Earth's sidereal rate, but there is similarity in the shape of the trends. As expected, the largest motion is about the Y-axis, which most closely aligns with the normal to the orbital plane. The average total rotation is about $1.125 \times 10^{-3}$ radians per second (or about 358.1° per nominal orbital period) which gives very high confidence in the model because the total motion should be about $360° \pm 2°$ in 92.6 minutes for the orbit of the ISS varying by the change in ISS attitude such as shown in Figure 8 on page 17.

## *3.2 Coordinate Transformation*

The relationship between the SA and DMP coordinate systems is paramount in deriving payload attitudes. It is an essential step in understanding how to relate disturbances at the base of the SAGE III ISS payload to the science measurements acquired at the SA scan head.

Both the SA and DMP data files output from STK are in the Comma Separated Value (CSV) format that can be readily ingested in MATLAB. STK outputs lines and columns that are not necessary for data analyses and are removed. After the data are imported into MATLAB the DMP rate data are corrected for direction as described in Section 3.1.4. Random error based on known measurement noise (described in Table 3 on page 25) can be added to both the DMP and SA data sets.

### 3.2.1 Coordinate Transformation Methods

To fully derive a coordinate transformation, two linearly independent vectors need to be (perfectly) measured in each of the two coordinate systems. A single vector measured in each of the coordinate systems lacks knowledge of one coordinate degree of freedom to fully constrain the transformation. One measured vector may be rotated into the other, but the coordinate system clocking around the measured vector

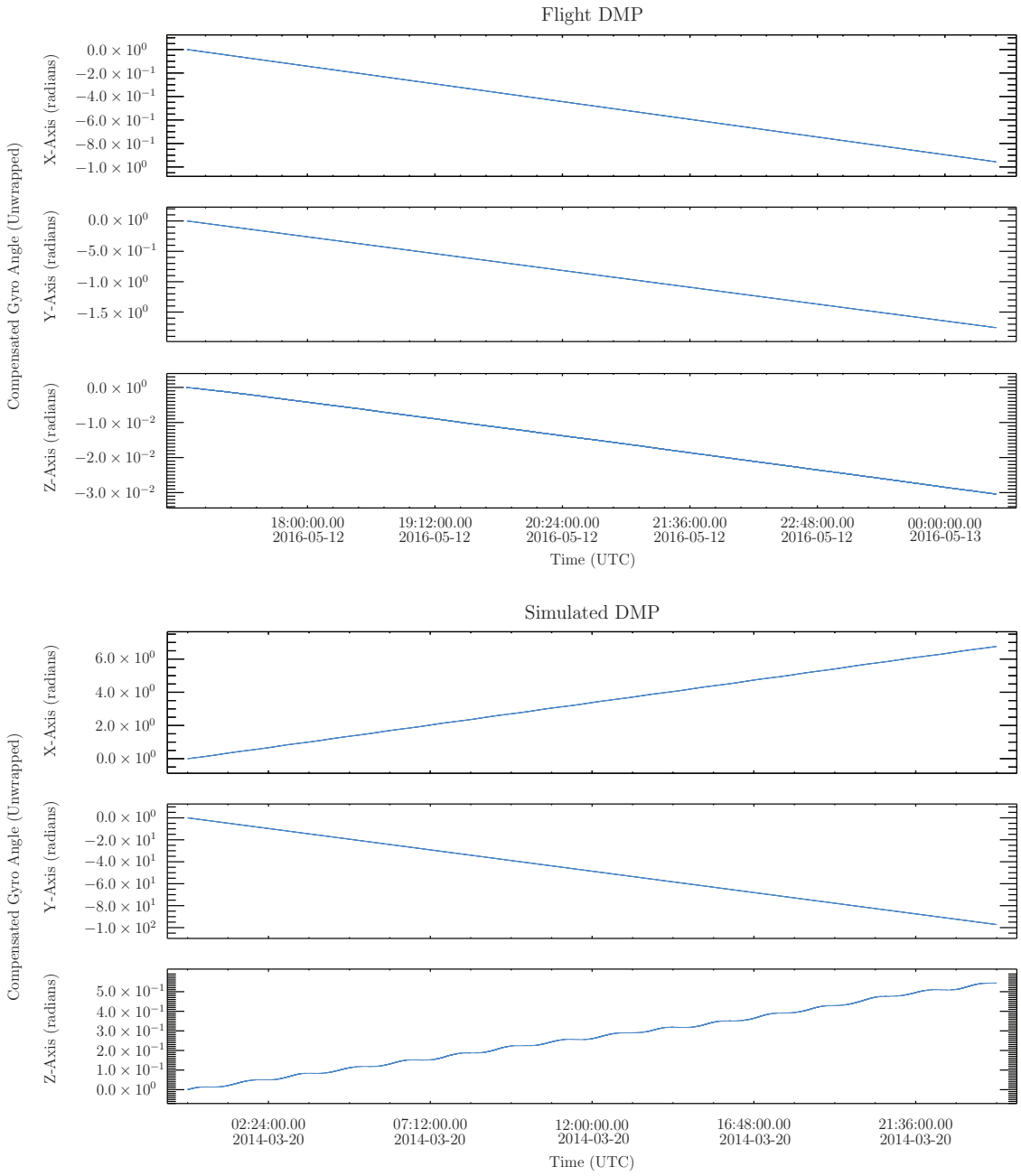


**Figure 17: DMP Flight Unit Data vs Simulated Data.** The top three plots are flight DMP data during ground testing at KSC for the X-, Y-, and Z-axes in radians. The bottom three plots are simulated on-orbit DMP data for the X-, Y-, and Z-axes.

remains unconstrained. A second, linearly independent vector measured in each of the coordinate frames would constrain the clocking because a coordinate transformation would have to match both vectors. On orbit two vectors (i.e., rotation axes) will be measured by the DMP at distinct times, and the same two vectors will be derived from the SA as it tracks the Sun during occultation measurements to derive one coordinate transformation.

A transformation from DMP measurements of rates of rotation about each of its RLG axes ($d_1$, $d_2$, $d_3$) to rates derived from the SA ($s_1$, $s_2$, $s_3$) could be thought of as

$$\begin{bmatrix} s_1 \\ s_2 \\ s_3 \end{bmatrix} = \boldsymbol{M} \begin{bmatrix} d_1 \\ d_2 \\ d_3 \end{bmatrix}, \tag{14}$$

where $\boldsymbol{M}$ is the transformation matrix. To discover the elements of matrix $\boldsymbol{M}$, and assuming that the DMP basis space is potentially non-orthogonal, the goal of the above construction might be to take enough linearly independent measurements to find $\boldsymbol{M}$ uniquely by

$$\begin{bmatrix} s_{1A} & s_{1B} & & s_{1N} \\ s_{2A} & s_{2B} & \dots & s_{2N} \\ s_{3A} & s_{3B} & & s_{3N} \end{bmatrix} = \boldsymbol{M} \begin{bmatrix} d_{1A} & d_{1B} & & d_{1N} \\ d_{2A} & d_{2B} & \dots & d_{2N} \\ d_{3A} & d_{3B} & & d_{3N} \end{bmatrix}, \tag{15}$$

for measurements $A, B, \ \dots, N$. Non-orthogonality implies at least nine linearly independent measurements for the nine independent matrix unknowns. Linear dependence can be tested by checking that the determinant of the matrix of vector measurements is non-zero. The astute reader will already have detected obstacles to this approach.

Finding $\boldsymbol{M}$ using the Singular Value Decomposition (SVD) or some other technique to invert the matrix of DMP measurements is unlikely to be satisfactory. This method assumes the measurements are free from error. With perfect measurements from all measurement systems, matrix $\boldsymbol{M}$ would capture only the non-orthogonality

contained in the basis spaces of the coordinate frames if any. In practice, measurements cannot be perfect, and the resulting DMP matrix will either be unstable on inversion because a reasonable solution will not always exist or will incorporate measurement errors into matrix $\boldsymbol{M}$ increasing the apparent non-orthogonality. There is no clear way to separate non-orthogonality in the coordinate systems from measurement error in this approach. The attitude determination and control literature provides direction in computing a transformation using imperfectly measured sets of vectors.

Similar to the above approach and for historical context, the tri-axial attitude determination (TRIAD) algorithm is a simple, deterministic method published by Harold D. Black (1964) that derives the DCM relating the frames of the two measured vectors. The TRIAD solution was one of the first computational solutions to the attitude determination problem described in the last few paragraphs. It was a key innovation developed for the Navy Navigation Satellite System, which was the first satellite navigation system (Black, 1990). The estimate of the DCM is given by Equation 16, where measurement-based vectors $\hat{b}_1$ and $\hat{b}_{12}$ and their cross product $\hat{b}_1 \times \hat{b}_{12}$ are used as the orthonormal body frame triad, and similarly measurement-based $\hat{r}_1$ and $\hat{r}_{12}$ and cross product $\hat{r}_1 \times \hat{r}_{12}$ are the orthonormal reference frame triad.

$$\boldsymbol{A}_{TRIAD} = [\hat{b}_1 \vdots \hat{b}_{12} \vdots \hat{b}_1 \times \hat{b}_{12}][\hat{r}_1 \vdots \hat{r}_{12} \vdots \hat{r}_1 \times \hat{r}_{12}]^T. \tag{16}$$

Similar to Equation 15 with $N = 3$, matrix $\boldsymbol{A}_{TRIAD}$ therefore estimates the DCM as the solution to the above linear system of equations with the exception that the measurement-based unit vectors must be orthonormal. TRIAD employed the following to construct these vectors and to better handle measurement noise. A measurement of a vector in the body frame yields unit vector $\hat{b}_1$, and a measurement of that same vector in the reference frame yields $\hat{r}_1$. A measurement of a second vector in

body and reference frames are recorded as $\hat{b}_2$ and $\hat{r}_2$ respectively. Construct

$$\hat{b}_{12} = \frac{\hat{b}_1 \times \hat{b}_2}{|\hat{b}_1 \times \hat{b}_2|} \quad \text{and} \quad \hat{r}_{12} = \frac{\hat{r}_1 \times \hat{r}_2}{|\hat{r}_1 \times \hat{r}_2|} \tag{17}$$

to form orthonormal vectors from the measured vectors. The third vectors in the triads, $\hat{b}_1 \times \hat{b}_{12}$ and $\hat{r}_1 \times \hat{r}_{12}$, are therefore natively unit vectors. Although the TRIAD method is one of the simplest methods to implement, it does not find the optimal attitude fit to the measured vectors in the general case as described by Markley (1993). Clearly, despite measurement noise, the TRIAD method matches one pair of vectors $\hat{b}_1$ and $\hat{r}_1$ exactly, and then rotates coordinate systems to fit the directed planes formed by the measurement pairs. Because all measurements are noisy, an optimal fit would be an attitude transform that minimizes error residuals for both measurement pairs.

The q-method (Wahba, 1966) is one of the many statistical methods that minimizes the Wahba loss function $J(\mathbf{A})$ shown in Equation 18, where $\hat{u}^i_B$ and $\hat{u}^i_R$ are the vector measurements in the body and reference coordinate frames respectively, $w_i$ is the weight of the $i^{\text{th}}$ vector measurement, and $\mathbf{A}$ is the attitude matrix with $+1$ determinant that minimizes $J(\mathbf{A})$ when optimized.

$$J(\mathbf{A}) = \frac{1}{2}\sum_{i=1}^{n} w_i |\hat{u}^i_B - \mathbf{A}\hat{u}^i_R|^2. \tag{18}$$

Grace Wahba proposed the above minimization problem to optimize the coordinate transformation estimation $\mathbf{A}$ in 1965. The equation includes the sum of squared differences between the measured body frame vectors and their transformed counterparts from the reference frame, and the weights can be related to the estimated measurement errors or set equal. The q-method proposes to minimize the loss function by stating the problem in terms of quaternions and rearranging to form an eigenvalue equation. The quaternion eigenvector that corresponds to the largest eigenvalue is the least-squares optimal estimate of the attitude. The q-method has become a basis for many other algorithms since its derivation by Davenport in 1968. Subsequent

algorithms (including the following two discussed) have built upon the q-method by addressing shortcomings such as computing eigenvectors and vector weighting.

The quaternion estimator (QUEST) algorithm is a statistical method derived by Shuster in 1981 and is used in many spacecraft today. It differs from the q-method because it computes the maximum eigenvalue $\lambda_{max}$ by using the Newton-Raphson method and substitutes Rodrigues parameters for quaternions. (For an extensive description of Rodrigues parameters see Section 3.3.1.) The Newton-Raphson method is a simple, well-known numerical method that iteratively approaches the root of a real-valued function that is close to an initial guess. The number of computations performed is dependent upon the quality of the initial guess. The maximum eigenvalue of the q-method is one of the roots of the characteristic equation of the Davenport matrix shown in Equation 19. See Shuster and Oh (1981) for a derivation and definitions of the constants. The equation is included to show that there are four roots. For sufficiently accurate and low-noise measurements of the attitude vector pairs, something available in 1981 to state-of-the-art spacecraft, the initial guess for the root of the characteristic polynomial $\lambda_{opt} = \sum w_i$ is close to $\lambda_{max}$. After iterating the Newton-Raphson method on the order of three times $\lambda_{max}$ is found to high precision.

$$p(\lambda) = \lambda^4 - (a+b)\lambda^2 - c\lambda + (ab + c\sigma - d). \tag{19}$$

Instead of directly finding the eigenvector as a quaternion, the Rodrigues parameters are calculated using Equation 20, the eigenvector is found, and the Rodrigues parameters can be converted back into a quaternion.

$$p = \frac{\vec{q}}{q_1} = \hat{e} \tan \frac{\Phi}{2}. \tag{20}$$

Because it finds an optimal, least-squares fit, the QUEST method has better accuracy than TRIAD, and it is an improvement to the q-method because it is computationally faster.

The final development in this brief historical summary is the optimal fast quaternion estimation method developed by F. Landis Markley (2002) and is the fit method chosen for the present research. This method was created to improve the speed of solving Wahba's loss function over existing methods. Remarkably, it is as efficient and fast as the quick but suboptimal TRIAD fit. Markley takes particular care to ensure computational stability and avoids explicit trigonometric function evaluations. The following presentation is adapted from Markley (2002) using the quaternion definition from Section 2.2 and rotating the body frame into the inertial frame.

With two vectors $\boldsymbol{r}_1$ and $\boldsymbol{r}_2$ in the inertial frame and $\boldsymbol{b}_1$ and $\boldsymbol{b}_2$ in the body frame, define the normalized cross products as

$$\begin{aligned} \boldsymbol{r}_3 &= \frac{\boldsymbol{r}_1 \times \boldsymbol{r}_2}{|\boldsymbol{r}_1 \times \boldsymbol{r}_2|} \quad \text{and} \\ \boldsymbol{b}_3 &= \frac{\boldsymbol{b}_1 \times \boldsymbol{b}_2}{|\boldsymbol{b}_1 \times \boldsymbol{b}_2|}. \end{aligned} \tag{21}$$

For computational stability avoiding the possibility of a mathematical singularity when constructing the optimum quaternion in Equations 27 and 28, the original reference coordinate frame can be rotated. The rotation is chosen based on the maximum of the set

$$\left\{ \boldsymbol{r}_{31}\boldsymbol{b}_{31}, \boldsymbol{r}_{32}\boldsymbol{b}_{32}, \boldsymbol{r}_{33}\boldsymbol{b}_{33}, \boldsymbol{r}_3 \cdot \boldsymbol{b}_3 \right\}. \tag{22}$$

Dependent upon the computed maximum, the algorithm rotates the input vectors as

$$\begin{aligned} \boldsymbol{r}_{31}\boldsymbol{b}_{31} &\Rightarrow \boldsymbol{r}_i \equiv [\boldsymbol{r}_{i1}, -\boldsymbol{r}_{i2}, -\boldsymbol{r}_{i3}], \\ \boldsymbol{r}_{32}\boldsymbol{b}_{32} &\Rightarrow \boldsymbol{r}_i \equiv [-\boldsymbol{r}_{i1}, \boldsymbol{r}_{i2}, -\boldsymbol{r}_{i3}], \\ \boldsymbol{r}_{33}\boldsymbol{b}_{33} &\Rightarrow \boldsymbol{r}_i \equiv [-\boldsymbol{r}_{i1}, -\boldsymbol{r}_{i2}, \boldsymbol{r}_{i3}], \quad \text{and} \\ \boldsymbol{r}_3 \cdot \boldsymbol{b}_3 &\Rightarrow \boldsymbol{r}_i \equiv [\boldsymbol{r}_{i1}, \boldsymbol{r}_{i2}, \boldsymbol{r}_{i3}], \end{aligned} \tag{23}$$

with $i = 1, 2, 3$. When $\boldsymbol{r}_3 \cdot \boldsymbol{b}_3$ is the maximum of the set, no rotation is necessary.

The optimum quaternion $q$ with weighting factors $a_i$ is found using the following set of equations.

$$\alpha \equiv (1 + \boldsymbol{r}_3 \cdot \boldsymbol{b}_3)(a_1\boldsymbol{r}_1 \cdot \boldsymbol{b}_1 + a_2\boldsymbol{r}_2 \cdot \boldsymbol{b}_2) + (\boldsymbol{r}_3 \times \boldsymbol{b}_3) \cdot (a_1\boldsymbol{r}_1 \times \boldsymbol{b}_1 + a_2\boldsymbol{r}_2 \times \boldsymbol{b}_2). \tag{24}$$

$$\beta \equiv (\boldsymbol{r}_3 + \boldsymbol{b}_3) \cdot (a_1 \boldsymbol{r}_1 \times \boldsymbol{b}_1 + a_2 \boldsymbol{r}_2 \times \boldsymbol{b}_2). \tag{25}$$

$$\gamma \equiv \sqrt{\alpha^2 + \beta^2}. \tag{26}$$

If $\alpha \geq 0$ then compute $\delta = \gamma + \alpha$, and

$$q = \frac{1}{2\sqrt{\gamma\delta(1 + \boldsymbol{r}_3 \cdot \boldsymbol{b}_3)}} \begin{bmatrix} \delta(1 + \boldsymbol{r}_3 \cdot \boldsymbol{b}_3) \\ \delta(\boldsymbol{r}_3 \times \boldsymbol{b}_3) + \beta(\boldsymbol{r}_3 + \boldsymbol{b}_3) \end{bmatrix} \equiv \begin{bmatrix} q_0 \\ q_1 \\ q_2 \\ q_3 \end{bmatrix}. \tag{27}$$

If $\alpha < 0$ then compute $\delta = \gamma - \alpha$, and

$$q = \frac{1}{2\sqrt{\gamma\delta(1 + \boldsymbol{r}_3 \cdot \boldsymbol{b}_3)}} \begin{bmatrix} \beta(1 + \boldsymbol{r}_3 \cdot \boldsymbol{b}_3) \\ \beta(\boldsymbol{r}_3 \times \boldsymbol{b}_3) + \delta(\boldsymbol{r}_3 + \boldsymbol{b}_3) \end{bmatrix} \equiv \begin{bmatrix} q_0 \\ q_1 \\ q_2 \\ q_3 \end{bmatrix}. \tag{28}$$

To "undo" the rotation introduced by Equation 23 adjust the quaternion with

$$\begin{aligned} &\boldsymbol{r}_{31}\boldsymbol{b}_{31} \Rightarrow q = [-q_1, q_0, q_3, -q_2], \\ &\boldsymbol{r}_{32}\boldsymbol{b}_{32} \Rightarrow q = [-q_2, -q_3, q_0, q_1], \\ &\boldsymbol{r}_{33}\boldsymbol{b}_{33} \Rightarrow q = [-q_3, q_2, -q_1, q_0], \quad \text{and} \\ &\boldsymbol{r}_3 \cdot \boldsymbol{b}_3 \Rightarrow q = [q_0, q_1, q_2, q_3]. \end{aligned} \tag{29}$$

The optimal fast quaternion estimation method is used to find the quaternion that defines the coordinate transformation between the DMP and SA.

### 3.2.2 DMP Quaternions

DMP quaternions are constructed by summing the DMP attitude rates that fall between SA event start and stop times. This is accomplished by adding the angular velocities at 200 Hz between SA measurement times to get a total change in angular position. Adding rotations is not commutative, but rates can be assumed constant over 1/200 of a second allowing DMP axes to be added in quadrature to obtain a

rate vector. Each partial quaternion $q_{rate}$ corresponding to each 1/200 of a second rotation is constructed by building a quaternion out of the rate vector $\boldsymbol{d}_{rate}$ and rate vector norm $n$.

$$q_{rate} = \begin{bmatrix} \cos\frac{n}{2} \\ \boldsymbol{d}_{rate}\frac{\sin\frac{n}{2}}{n} \end{bmatrix}. \tag{30}$$

The final rotation is an ordered multiplication of all the partial quaternions.

Clearly the total angle of rotation $\omega$ observed by the DMP for each quaternion is

$$\omega = 2\arccos q_s, \tag{31}$$

where $q_s$ is the scalar term of the quaternion. This angle is used in Section 3.2.3 to derive the total SA quaternions.

### 3.2.3 SA Quaternions

SA pointing subsystem measurements of boresight directions while tracking the Sun are an incomplete representation of total payload rotation. The SA reports azimuth and elevation angles but does not measure the clocking angle about the Sun. Therefore, additional computation making use of the DMP total angle of rotation is necessary to construct an SA quaternion of total rotation. Rotation axes of these occultation event total rotation quaternions are ultimately used to find the optimal coordinate transformation between DMP and SA coordinate frames. The axes of rotation, which include measurement error, become the vector inputs to Markley's optimal fast quaternion estimation method described at the end of Section 3.2.1. The following were derived for the present research.

Given two normalized measurements of the Sun center by the SA scan head at an occultation event start time $t = 1$ and end time $t = 2$, construct $\boldsymbol{v}_1$ and $\boldsymbol{v}_2$, such that

$$\begin{aligned} \boldsymbol{v}_1 &= [\cos\theta_1\cos\phi_1, -\cos\theta_1\sin\phi_1, -\sin\theta_1], \quad \text{and} \\ \boldsymbol{v}_2 &= [\cos\theta_2\cos\phi_2, -\cos\theta_2\sin\phi_2, -\sin\theta_2], \end{aligned} \tag{32}$$

where $\phi$ is the azimuth angle, and $\theta$ is the elevation angle of the SA measurement. A partial quaternion $q_1$ can be constructed between the two Sun measurements that excludes only the clocking rotation of the payload around the Sun vector.

$$q_1 = q_{10} + \boldsymbol{q}_1, \quad q_{10} = \sqrt{\frac{1 + \boldsymbol{v}_2 \cdot \boldsymbol{v}_1}{2}}, \quad \text{and} \quad \boldsymbol{q}_1 = \sqrt{\frac{1 - \boldsymbol{v}_2 \cdot \boldsymbol{v}_1}{2}} \frac{\boldsymbol{v}_2 \times \boldsymbol{v}_1}{|\boldsymbol{v}_2 \times \boldsymbol{v}_1|}. \tag{33}$$

Constructing a subsequent clocking quaternion $q_2$ about the spacecraft-Sun vector (with unknown $\omega'$ rotation about $\boldsymbol{v}_2$) leads to

$$q_2 = q_{20} + \boldsymbol{q}_2, \quad q_{20} = \cos\frac{\omega'}{2}, \quad \text{and} \quad \boldsymbol{q}_2 = \sin\frac{\omega'}{2}\boldsymbol{v}_2. \tag{34}$$

Then, the quaternion $q'$ of total rotation with unknown total $\omega$ and axis $\hat{\boldsymbol{n}}$ is

$$q' = q_1 q_2 = q'_0 + \boldsymbol{q'}, \quad q'_0 = \cos\frac{\omega}{2}, \quad \text{and} \quad \boldsymbol{q'} = \sin\frac{\omega}{2}\hat{\boldsymbol{n}}. \tag{35}$$

The DMP magnitude of the total rotation is highly accurate over the course of an occultation event. For the purpose of statistically obtaining over time the best-fit coordinate transformation between DMP and SA coordinate frames, the DMP total rotation can be used for $\omega$. Building an independent statistical assessment of the coordinate transformation errors over many events allows auditing of the validity of this approach. All that remains to find $q'$ is to solve for clocking rotation $\omega'$ in terms of total rotation $\omega$. Intuitively, knowing the partial rotation between $\boldsymbol{v}_1$ and $\boldsymbol{v}_2$ as measured by the SA and knowing the total rotation $\omega$ as measured by the DMP completely constrains the unmeasured clocking rotation $\omega'$. Begin by defining $q_1$ and $\boldsymbol{q}_1$ components as

$$q_1 \equiv (q_{10}, q_{11}, q_{12}, q_{13}) \quad \text{and} \quad \boldsymbol{q}_1 \equiv (q_{11}, q_{12}, q_{13}). \tag{36}$$

Then the matrix form of the quaternion product $q_1 q_2 = q'$ after factoring is

$$\begin{bmatrix} q_{10} & -q_{11} & -q_{12} & -q_{13} \\ q_{11} & q_{10} & q_{13} & -q_{12} \\ q_{12} & -q_{13} & q_{10} & q_{11} \\ q_{13} & q_{12} & -q_{11} & q_{10} \end{bmatrix} \begin{bmatrix} \cos\frac{\omega'}{2} \\ v_{21}\sin\frac{\omega'}{2} \\ v_{22}\sin\frac{\omega'}{2} \\ v_{23}\sin\frac{\omega'}{2} \end{bmatrix} = \pm \begin{bmatrix} \cos\frac{\omega}{2} \\ n_1\sin\frac{\omega}{2} \\ n_2\sin\frac{\omega}{2} \\ n_3\sin\frac{\omega}{2} \end{bmatrix}. \tag{37}$$

Hence, the first matrix equation (the scalar component) is

$$q_{10} \cos \frac{\omega'}{2} - \boldsymbol{q}_1 \cdot \boldsymbol{v}_2 \sin \frac{\omega'}{2} = \pm \cos \frac{\omega}{2}. \tag{38}$$

Because $\boldsymbol{q}_1$ is orthogonal to $\boldsymbol{v}_2$ by definition, Equation 38 can be simplified and solved for $\omega'$ resulting in

$$\omega' = \pm 2 \arccos \frac{\cos \frac{\omega}{2}}{q_{10}}. \tag{39}$$

This defines the relationship between $\omega$ and $\omega'$. There are two solutions for clocking rotation $\omega'$ because the total rotation constraint $\omega$ is a magnitude, and so either clocking direction around $\boldsymbol{v}_2$ will sum with $q_1$ to yield the correct total $\omega$. Only one of these solutions is correct for a given occultation scenario. The positive angle is arbitrarily chosen to solve for $\omega'$, and for the final quaternion $q_2$ the angle between $\boldsymbol{v}_2$ and the DMP quaternion vector is used to test if the Sun clocking axis needs to be flipped to correspond to the occultation event. This occurs when the angle is greater than 90°. Note the assumption here that the DMP axes are sufficiently orthogonal to derive an accurate total $\omega$. This assumption is the origin of the desire to test how non-orthogonal DMP axes manifest in the statistical audit of this process that is documented in Chapter 4. With $\omega'$ known, Equation 34 can be solved for $q_2$, and then Equation 35 can be solved for the SA quaternion of total rotation.

#### *3.2.3.1 Apparent Sun Motion Correction*

The ecliptic plane is defined by the path of the Earth around the Sun (Prussing and Conway, 1993). As viewed from the Earth the Sun is not a fixed inertial point; it moves through the celestial sphere with respect to the distant stars of the zodiac. Similar motion is observed from the perspective of the ISS. The ephemeris source used for the Sun in STK is the Jet Propulsion Laboratory's Planetary and Lunar Development Ephemerides DE430 model (Folkner et al., 2014). Over the course of an average SAGE III simulated solar event the noninertial motion of the Sun as viewed by the ISS is on the order of several arcseconds. This is included in simulated data

because this motion will present itself as error in the coordinate transformation. The underlying assumption of the coordinate transformation algorithm is that both the DMP and SA are measuring the rotation of the payload—the DMP using RLGs and the SA as essentially a star tracker but without measurements of clocking rotations around the Sun vector. The solar clocking problem is resolved in Equations 32–39, but because the SA tracks the Sun during an occultation event, the noninertial Sun motion will cause a small discrepancy between the DMP and SA observations. To investigate the degree to which the noninertial motion of the Sun is problematic in calibrating the coordinate transformation, a method was devised to correct the SA observations for this motion and compare coordinate transformation results with the uncorrected calibration.

The process for removing this apparent motion requires additional STK information. An attitude quaternion $q_a$ is needed to define the payload attitude in ICRF coordinates. Furthermore, the vectors $\boldsymbol{v}_{1,ICRF}$ and $\boldsymbol{v}_{2,ICRF}$ are necessary to directly correspond to $\boldsymbol{v}_1$ and $\boldsymbol{v}_2$ but in the ICRF coordinate system. The inertial motion of the Sun can be tracked using these ICRF Sun vectors because ICRF is defined with origin at the barycenter of the Solar System and with 212 relatively fixed extragalactic sources that establish axes orientations.

A "correction" is found by constructing a quaternion between the Sun vectors in ICRF coordinates ($q_{correction}$), which amounts to the change in the inertial position of the Sun between the event exoatmospheric start and stop times. This quaternion is being called a correction because it will be applied to one of the Sun vectors in the SA coordinate frame to remove the apparent Sun motion. The quaternion representing

the rotation between the start ($\boldsymbol{v}_{1,ICRF}$) and end ($\boldsymbol{v}_{2,ICRF}$) in ICRF is found by

$$\begin{aligned} q_{correction} &= q_{10c} + \boldsymbol{q}_{1c}, \\ q_{10c} &= \sqrt{\frac{1 + \boldsymbol{v}_{2,ICRF} \cdot \boldsymbol{v}_{1,ICRF}}{2}}, \quad \text{and} \\ \boldsymbol{q}_{1c} &= \sqrt{\frac{1 - \boldsymbol{v}_{2,ICRF} \cdot \boldsymbol{v}_{1,ICRF}}{2}} \frac{\boldsymbol{v}_{2,ICRF} \times \boldsymbol{v}_{1,ICRF}}{|\boldsymbol{v}_{2,ICRF} \times \boldsymbol{v}_{1,ICRF}|}. \end{aligned} \tag{40}$$

Application of a Sun correction allows the SA to track the inertial attitude of its initial $\boldsymbol{v}_1$ measurement by applying a correction to $\boldsymbol{v}_2$. Because the correction quaternion is known in ICRF, the event end vector in the SA frame, $\boldsymbol{v}_2$, is transformed into the ICRF frame resulting in $\boldsymbol{v}_{2,T}$.

$$\boldsymbol{v}_{2,T} = q_a \boldsymbol{v}_2 q_a^*. \tag{41}$$

The Sun motion correction is applied to vector $\boldsymbol{v}_{2,T}$ by

$$\boldsymbol{v}'_{2,T} = q_{correction} \boldsymbol{v}_{2,T} q^*_{correction}. \tag{42}$$

Finally, the now corrected event end vector $\boldsymbol{v}'_{2,T}$ is transformed back into the SA coordinate frame and redefined as $\boldsymbol{v}_2$.

$$\boldsymbol{v}_2 = \boldsymbol{v}'_2 = q_a^* \boldsymbol{v}'_{2,T} q_a. \tag{43}$$

### 3.2.4 Coordinate Transformation Code Flow

The coordinate transformation algorithm code developed for this thesis is not provided because it is proprietary software owned by NASA Langley Research Center. Consequently, the diagram shown in Figure 18 outlines the details of how the methods described in the preceding sections of Chapter 3 are combined into a single algorithm. The general flow is described as follows.

- The algorithm begins with the ingest of STK CSV data files.
- Both the SA and DMP data require a correction, described in Sections 3.1.3 and 3.1.4, respectively.

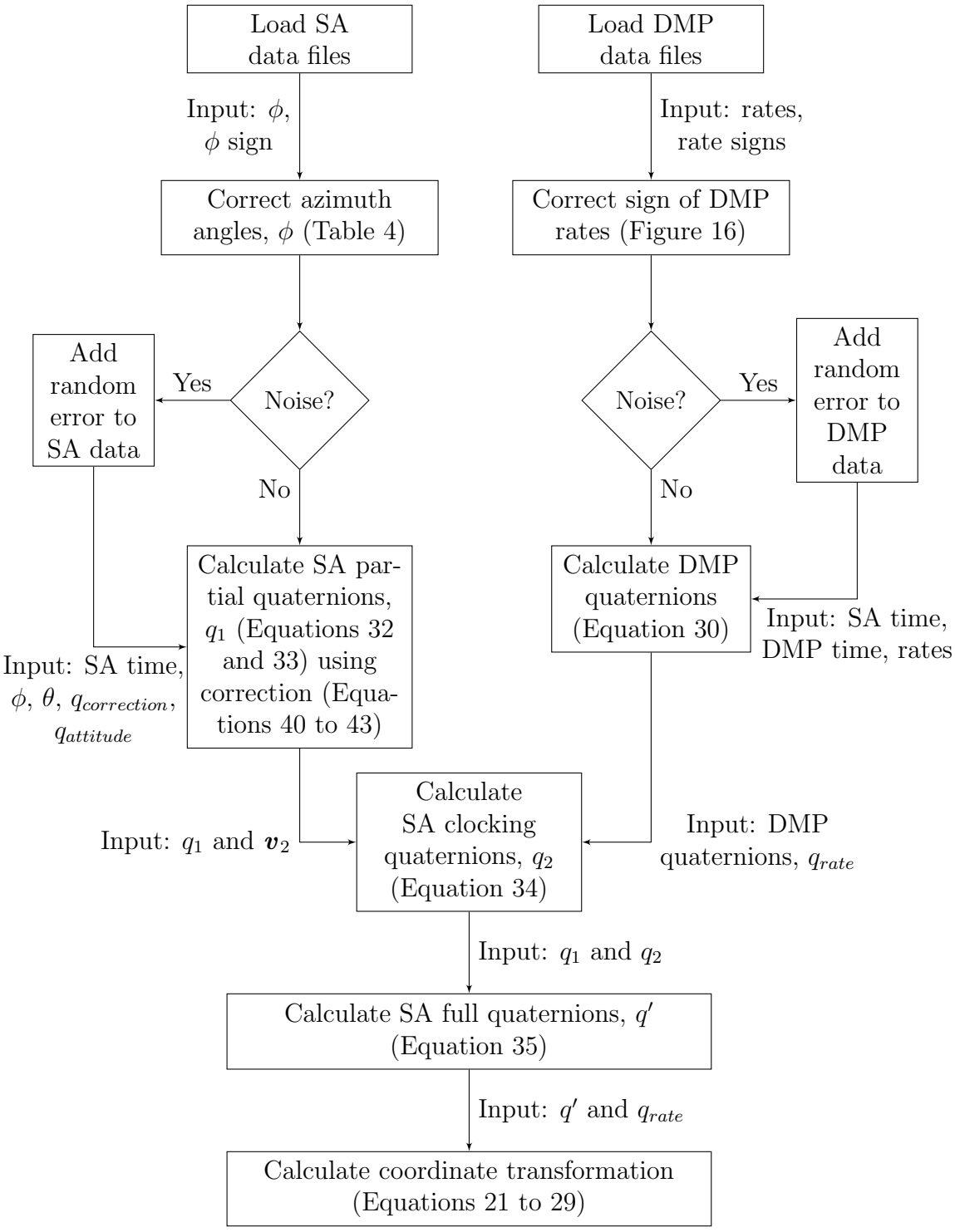


**Figure 18: Coordinate Transformation Algorithm Flow.** The algorithm to calibrate the DMP-to-SA coordinate transformation illustrated above was implemented in MATLAB code.

- Gaussian noise can be added to all simulated measurements, if desired, to simulate flight-like conditions as described in detail in Chapter 4.
- Quaternions are calculated for each of the SA and DMP measurements as described in Sections 3.2.3 and 3.2.2, respectively.
- Finally, the coordinate transformation is derived from SA and DMP quaternion vectors using the fast quaternion method described in Section 3.2.1.

## *3.3 Kalman Filter*

Digital filtering is a mathematical tool to manipulate discrete-time signal inputs to return an improved output. Improved is a vague term, but in the case of attitude determination the goal of a digital signal filter is to combine attitude measurements from different systems in an optimal way to produce an output with less noise and increased accuracy. The 200 Hz DMP measurements have very high precision and accuracy, but measure only relative attitude changes. Over increasing time intervals the small error in each measured RLG attitude rate will sum to an increasingly large absolute attitude error. The DMP attitude calculated from summing the individual rate measurements will deviate on a random walk from the actual attitude. With sufficient time, even extremely accurate rate measurements will sum to yield an attitude arbitrarily far from the real attitude. The SA measurements of attitude are more coarse but can be used to provide an absolute measurement of attitude in inertial coordinates. A blending of the two measurements can vastly improve the overall attitude knowledge of the payload because the absolute measurement provided by the SA can correct the DMP Angular Random Walk (ARW) during each solar occultation event.

The Kalman filter, named after Rudolf Emil Kálmán of Kalman (1960)—although also accredited to Thorvald Nicolai Thiele, Peter Swerling, and Richard Snowden Bucy—is an algorithm that can be applied to combine past and current attitude

measurements from multiple measurement systems with the goal of finding the most robust and accurate attitude estimate. Having a wide variety of applications, the Kalman filter is a common approach to attitude determination problems and was applied as early as the Apollo guidance system in 1961. At its heart, the Kalman filter is a low pass digital filter with multiple discrete-time inputs that are combined by a weighted average. These inputs are actually weighted dynamically according to a running estimate of their measurement uncertainties. Typical for low pass digital filters, the Kalman filter method is a recursive infinite impulse response (IIR) filter. Its versatility includes both linear and non-linear problems. The non-linear version is called the extended Kalman filter. The general flow, as described in Wertz (1978), is an initialization of the state vector followed by a cycle of propagating the state vector by a physical model and correcting the state vector with a measurement update. The filter uses a recursive least-squares estimator for both the state vector and a state vector error covariance matrix.

It is important to note that the filtering performed for SAGE III will be done on the ground in post processing unlike many spacecraft that use filtered output to make attitude control decisions realtime. This alleviates much of the computational and time concerns. Because intensive computation will not be needed onboard the payload, the steady-state Kalman filter, which has a fixed gain $\boldsymbol{K}$ and reduces computation time, is also not necessary. The filtered output will be used to correct the science data product and will be one algorithm within a complex computational process. Based on this assessment and given its superior performance in estimating attitude, the Kalman filter will be the method used for the SAGE III attitude determination problem. Although it is not the simplest method, the use of weighted averages and the estimation of the error covariance matrix make it attractive for the SAGE III ISS payload.

The Kalman filter is designed to predict the system behavior based on a physical model and to correct that prediction based on actual measurements. The more measurements that are incorporated into the filter, the more accurate the estimated attitude state. It is a balance between propagating the state which increases covariance and injecting a new measurement which decreases covariance (Crassidis and Junkins, 2012). In practice for attitude determination when rate gyroscopes are present, the physical model is taken directly from the gyroscope measurements rather than *a priori* tumbling physics. This can be understood by examining the DMP/SA problem. The DMP yields a dead reckoning measurement of attitude by calculating the current state based on a previously determined state and a rate of change measurement analogous to a physical model. While the rate measurements are extremely precise and accurate, the propagated state has diminishing accuracy and increasing covariance because of the creep caused by random walk over time. If the state propagation is modeled by the DMP, the estimate creeps proportionally to the magnitude of the DMP rate error, or ARW, with each propagation, behaving as a physical model propagation would. In contrast, when a new SA measurement is introduced during an occultation event into the filter, the state is corrected to an absolute attitude to within the SA measurement error. Rigid body tumbling physics involving the mass moments of inertia of the spacecraft are generally not used when rate gyroscopes are available. The measured gyroscope rates behave like a physical model for the purposes of propagation and tend to be far more accurate than a physical model because of external torques from drag, magnetism, radiation pressure, and gravitation which are too complicated to model. In the case of ISS, attitude is not left only to free fall dynamics but is internally adjusted by control moment gyroscopes. Additionally, the inertia tensor is dynamic because of ISS configuration changes and visiting vehicles and because of significant internal bending modes that are poorly characterized. A physics model in the attitude Kalman filter based on ISS tumbling dynamics is

practically impossible.

When parameterizing attitude, numerous options exist, several of which are discussed in Section 2.2. How these parameterizations behave in conjunction with the Kalman filter is a topic that has long been explored in the literature. Support for the use of quaternions arose because of the absence of polar degeneracies. Quaternions carry a redundant degree of freedom as a result of the double-covering of the 3-dimensional rotation group $SO(3)$, meaning $q$ represents the same rotation as $-q$. The difficulties in using quaternions with either the linear Kalman filter or the extended Kalman filter (EKF) include the violation of the quaternion normalization constraint and estimating the covariance. Henceforth, the Multiplicative Extended Kalman Filter (MEKF) laid out in Lefferts et al. (1982) will be implemented for the DMP/SA attitude determination to circumvent this problem. In the MEKF method, the attitude is represented by a quaternion, and the attitude difference is a 3-component representation, the latter of which is to be discussed in more detail later in this section. Quaternions lend themselves to this method in part because successive rotations are embodied by simple quaternion multiplication, and the quaternion kinematic equation is given by

$$\dot{q} = \frac{1}{2}\mathbf{\Omega}(\omega)q, \tag{44}$$

where $\mathbf{\Omega}(\omega)$ and $\lfloor \boldsymbol{\omega} \times \rfloor$ are defined by

$$\begin{aligned} \mathbf{\Omega}(\omega) &= \begin{bmatrix} 0 & -\boldsymbol{\omega} \\ \boldsymbol{\omega}^{\boldsymbol{T}} & -\lfloor \boldsymbol{\omega} \times \rfloor \end{bmatrix} \quad \text{and} \\ \lfloor \boldsymbol{\omega} \times \rfloor &= \begin{bmatrix} 0 & -\omega_3 & \omega_2 \\ \omega_3 & 0 & -\omega_1 \\ -\omega_2 & \omega_1 & 0 \end{bmatrix}. \end{aligned} \tag{45}$$

The $\omega_i$ terms denote angular velocities, and the $\lfloor \boldsymbol{\omega} \times \rfloor$ matrix is referred to as the angular velocity tensor or cross product matrix defined so that $\lfloor \boldsymbol{\omega} \times \rfloor \boldsymbol{u} = \boldsymbol{\omega} \times \boldsymbol{u}$.

The MEKF operates on the change in attitude, while the attitude state vector is maintained outside of the traditional filter structure. The attitude state vector is updated in an additional "reset" step in which the attitude difference is also reinitialized to zero. The use of the MEKF as opposed to an Additive Extended Kalman Filter (AEKF) is further supported by Markley (2004b,a), where the computational savings and a conceptual clarification are treated in detail. In addition, the MEKF does not require quaternion normalization to maintain unit quaternions.

### 3.3.1 3-Component Representations

A common problem encountered in the literature during early implementations of Kalman filters using the quaternion attitude representation was instability in the attitude estimate caused by the quaternion double cover of rotation group $SO(3)$. The real orthogonal $3 \times 3$ matrices $O(3)$ form a group under matrix multiplication that represent the distance preserving transformations of 3-dimensional vector space, including vector rotations and reflections. The inverse and transpose of any orthogonal matrix are equivalent, so that $\boldsymbol{M}^T\boldsymbol{M} = \boldsymbol{M}\boldsymbol{M}^T = \boldsymbol{I} \quad \forall \quad \boldsymbol{M} \in O(3)$, and so the determinant of any orthogonal matrix is $\pm 1$. The subgroup of $O(3)$ consisting of orthogonal matrices of determinant $+1$ is the special orthogonal group $SO(3)$. Every matrix of $SO(3)$ is a rotation of 3-dimensional vector space, and every rotation of 3-dimensional vector space can be represented by a matrix of $SO(3)$. The group formed by all quaternions of unit length also represents rotations of 3-dimensional vector space, but for every matrix of $SO(3)$ there are two quaternions that represent the same rotation—a double cover. As described in Section 2.2, quaternions $q$ and $-q$ represent the same rotation. While $q$ and $-q$ are equivalent as rotations, they are different in the space of 4-dimensional hypercomplex numbers. Suppose a spacecraft reports an attitude nearly constant at $q$ as tracked by a Kalman filter. If a measurement at some time indicates an attitude near $-q$, the Kalman gain applied to

the measurement can become unstable because this yields an unduly large difference quaternion. The current practice employs a stereographic projection of the quaternions using Rodrigues parameterization to a 3-dimensional hyperplane to reduce the dimensionality of the attitude representation by one while simultaneously ensuring that only half of the quaternion group is used for the representation to avoid the filter instability. A fascinating and complete treatment of quaternion topology and stereographic projection by Rodrigues and modified Rodrigues parameters can be found in Schaub and Junkins (1996).

Maintaining the quaternion normalization is challenging in the propagation of the covariance matrix because of roundoff error as discussed in detail in Lefferts et al. (1982). Although it is possible to project the $4 \times 4$ quaternion covariance onto a $3 \times 3$ matrix without loss of information, it is conceptually simpler to store the attitude difference in a 3-component representation. There are several options for a 3-component representation of attitude difference, two of which will be covered here: the Gibbs vector (Rodrigues parameters) and modified Rodrigues parameters (Markley, 2003). The Gibbs vector is described by

$$\boldsymbol{g} \equiv \frac{\boldsymbol{q}}{q_1} = \frac{\hat{\boldsymbol{e}} \sin \frac{\alpha}{2}}{\cos \frac{\alpha}{2}} = \hat{\boldsymbol{e}} \tan \frac{\alpha}{2}, \tag{46}$$

where $\alpha$ is the magnitude of rotation along the unit vector rotation axis $\hat{\boldsymbol{e}}$. The Gibbs vector reduces the representation from 4-dimensional to 3-dimensional, mapping $q$ and $-q$ to the same point on a 3-dimensional hyperplane. The chief problem with this representation is that $\boldsymbol{g}$ is infinite for 180° rotations. This singularity is similar to the polar degeneracy seen when using Euler angles, and so the Rodrigues representation eliminates the original advantage gained by choosing quaternions to represent attitudes.

In contrast, the modified Rodrigues parameters shown in Equation 47 are a 2-1

mapping where $q$ and $-q$ have unique representations.

$$\boldsymbol{a} \equiv \frac{\boldsymbol{q}}{1+q_1} = \frac{\hat{\boldsymbol{e}} \sin\frac{\alpha}{2}}{1+\cos\frac{\alpha}{2}} = \hat{\boldsymbol{e}} \tan\frac{\alpha}{4}. \tag{47}$$

The modified Rodrigues parameterization reduces the dimensionality of the quaternions by one and lacks the Gibbs vector singularity at 180°. The singularity at 360° in the modified Rodrigues parameterization is avoided by constraining the attitude representation to ±180°. The modified Rodrigues parameterization also avoids the Kalman gain instability caused by the quaternion double cover of $SO(3)$. For these reasons the following formulation will incorporate modified Rodrigues parameters.

### 3.3.2 MEKF

As explained in Section 3.3, measurements from the set of three RLGs contained in the SAGE III ISS DMP will serve as the filter's physical model. The DMP sample rate is sufficiently fast to assume continuous capture of payload rotation. In addition, the Kalman filter state vector will estimate and propagate the gyroscope bias. This will be particularly significant during the orbital time periods in which there are an absence of SA measurements. As described in Farrenkopf (1978), a gyro measurement of an angular rate $\boldsymbol{\omega}$ and its associated bias can be described by

$$\boldsymbol{\omega} = \boldsymbol{\omega}_m - \boldsymbol{b} - \boldsymbol{\eta}_\nu, \tag{48}$$

where $\boldsymbol{\omega}_m$ is the gyro measurement, $\boldsymbol{b}$ is the gyro drift rate or bias, and $\boldsymbol{\eta}_\nu$ is zero mean white Gaussian measurement noise.

The MEKF follows the same flow as the traditional Kalman filter: Initialization (Section 3.3.2.1), Prediction/Propagation (Section 3.3.2.2), and Measurement Update (Section 3.3.2.3). An additional step is included in Section 3.3.2.4 for the aforementioned "reset" step. Figure 19 shows a simplified flow diagram of the sections to come.

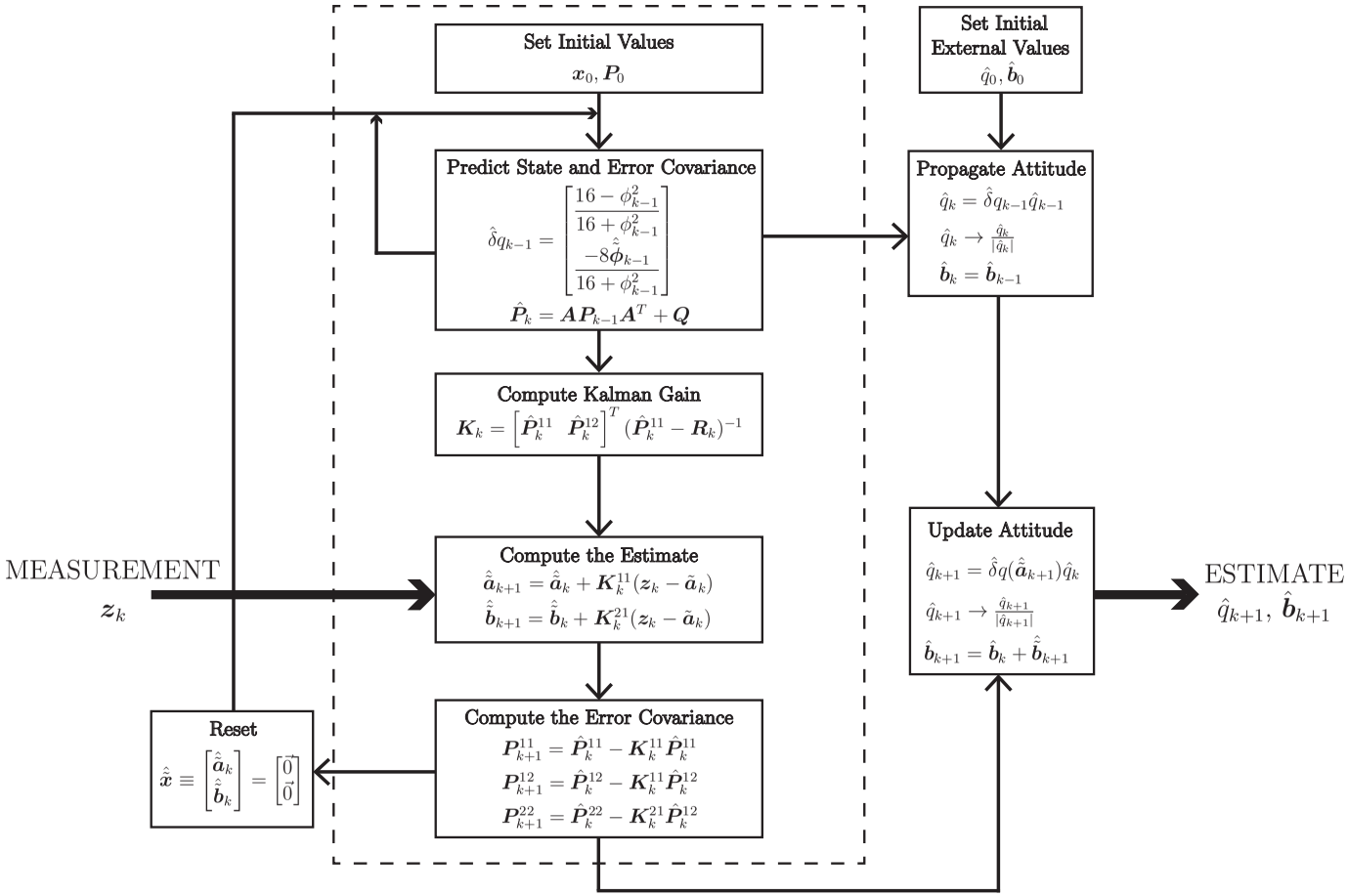


**Figure 19: Multiplicative Extended Kalman Filter Algorithm Flow.** The Kalman filter is a low pass digital filter with multiple discrete-time measurements that are combined by a weighted average to estimate the attitude quaternion and gyroscope bias. The DMP input serves as the physical model, while the absolute SA attitude is measurement $z_k$.

#### *3.3.2.1 Initialization*

The Kalman filter first initializes the state vector $\boldsymbol{x}$, covariance matrix $\boldsymbol{P}$, attitude quaternion $q$, and bias $\boldsymbol{b}$. In the following sections, the notation $\hat{\boldsymbol{c}}$ denotes an estimated value of some variable $\boldsymbol{c}$, and the notation $\tilde{\boldsymbol{c}}$ denotes the difference in a variable $\boldsymbol{c}$ between one filter cycle and the next.

The state vector $\hat{\tilde{\boldsymbol{x}}}$ tracks the difference or change in the estimated attitude $\hat{\boldsymbol{a}}$ and in the estimated bias $\hat{\boldsymbol{b}}$, with the change in attitude being expressed in modified Rodrigues parameterization. With subscripts counting the cycle number of the recursive digital Kalman filter, the initial value is

$$\hat{\tilde{\boldsymbol{x}}}_0 = \begin{bmatrix} \hat{\tilde{\boldsymbol{a}}} \\ \hat{\tilde{\boldsymbol{b}}} \end{bmatrix} = \begin{bmatrix} \vec{0} \\ \vec{0} \end{bmatrix}. \tag{49}$$

Because $\hat{\tilde{\boldsymbol{x}}}$ is $6 \times 1$, the covariance matrix $\boldsymbol{P}$ will be $6 \times 6$. Let covariance $\boldsymbol{P}$ be a symmetric matrix such that

$$\boldsymbol{P} = \begin{bmatrix} \boldsymbol{P}^{11} & \boldsymbol{P}^{12} \\ \boldsymbol{P}^{12^T} & \boldsymbol{P}^{22} \end{bmatrix}, \tag{50}$$

where each subset of $\boldsymbol{P}$ is a $3\times3$ matrix. Let $\boldsymbol{I}_3$ denote the $3\times3$ identity matrix, and let $\boldsymbol{0}_3$ denote a $3 \times 3$ matrix of zeroes. To initialize the covariance let $\boldsymbol{P}_0^{11} = \varepsilon_1^2 \boldsymbol{I}_3$, $\boldsymbol{P}_0^{12} = \boldsymbol{0}_3$, and $\boldsymbol{P}_0^{22} = \varepsilon_2^2 \boldsymbol{I}_3$ where $\varepsilon_1$ and $\varepsilon_2$ are the initial guesses of the standard deviations in total model noise, with variances $\varepsilon_1^2$ and $\varepsilon_2^2$. Using process noise for the initial guess, $\varepsilon_1$ is set to four times the standard deviation in the gyro measurement of the modified Rodrigues parameters, $\sigma_1$, and $\varepsilon_2$ is set to the standard deviation in the gyro bias, $\sigma_2$. Recall that modified Rodrigues parameters are defined by Equation 47. Assuming the state vector is tracking small differences, $\tan\frac{\alpha}{4} \approx \frac{\alpha}{4}$. Hence, the covariance can be estimated using only $4\times$ the gyro errors because the modified Rodrigues parameters

are approximated by $\frac{\alpha}{4}$. This leads to initial covariance matrix

$$\boldsymbol{P}_0 = \begin{bmatrix} 4\sigma_1^2 & 0 & 0 & 0 & 0 & 0 \\ 0 & 4\sigma_1^2 & 0 & 0 & 0 & 0 \\ 0 & 0 & 4\sigma_1^2 & 0 & 0 & 0 \\ 0 & 0 & 0 & \sigma_2^2 & 0 & 0 \\ 0 & 0 & 0 & 0 & \sigma_2^2 & 0 \\ 0 & 0 & 0 & 0 & 0 & \sigma_2^2 \end{bmatrix}. \tag{51}$$

The estimated attitude $\hat{q}$ and bias $\hat{\boldsymbol{b}}$ are tracked outside of the Kalman filter. They are initialized by

$$\hat{q}_0 = \begin{bmatrix} 1 \\ 0 \\ 0 \\ 0 \end{bmatrix} \quad \text{and} \quad \hat{\boldsymbol{b}}_0 = \begin{bmatrix} 0 \\ 0 \\ 0 \end{bmatrix}. \tag{52}$$

*3.3.2.2 State Propagation and Covariance Prediction*

After initialization, the next step in the Kalman filter is to propagate the state and predict the covariance matrix. As described in Crassidis and Junkins (2012), Markley (2003), and Trawny and Roumeliotis (2005), among others, the MEKF is designated "multiplicative" because the propagation of attitude is represented as a quaternion product between a reference quaternion and a difference quaternion. The preliminary step for this propagation begins with the DMP gyro measurements $\boldsymbol{\omega}_m$ such that

$$\hat{\boldsymbol{\omega}}_{k-1} = \boldsymbol{\omega}_m - \hat{\boldsymbol{b}}_{k-1}. \tag{53}$$

This equation states that the estimated vector of payload angular rates for filter cycle $k-1$ is the DMP rates measurement minus the estimate of the gyro bias. Cycle $k-1$ is used to signify that numbers from the cycle previous to cycle $k$ will be used to propagate the estimates of attitude and bias for cycle $k$. For DMP measurement time

interval $\Delta t$, the expected change in the vector of rotation angles $\boldsymbol{\phi}$ is given by

$$\begin{aligned} \hat{\hat{\boldsymbol{\phi}}}_{k-1} &= \hat{\boldsymbol{\omega}}_{k-1}\Delta t, \quad \text{and let} \\ \phi_{k-1}^2 &\equiv |\hat{\hat{\boldsymbol{\phi}}}_{k-1}|^2. \end{aligned} \tag{54}$$

With the expected change in $\boldsymbol{\phi}$ defined as above, the multiplicative difference quaternion $\hat{\delta}q$ to propagate the attitude is derived from Markley (2003) as

$$\hat{\delta}q_{k-1} = \begin{bmatrix} \dfrac{16 - \phi_{k-1}^2}{16 + \phi_{k-1}^2} \\ \dfrac{-8\hat{\hat{\boldsymbol{\phi}}}_{k-1}}{16 + \phi_{k-1}^2} \end{bmatrix}. \tag{55}$$

Outside of the filter the quaternion $q$ is propagated using Equation 56 and normalized using Equation 57 to avoid propagating computer roundoff error. Note that there is no need to directly calculate the modified Rodrigues parameters $\hat{\boldsymbol{a}}$ as $\hat{\delta}q$ is used to propagate attitude $q$.

$$\hat{q}_k = \hat{\delta}q_{k-1}\hat{q}_{k-1}. \tag{56}$$

$$\hat{q}_k \rightarrow \frac{\hat{q}_k}{|\hat{q}_k|}. \tag{57}$$

At this step there is no new absolute measurement to estimate gyro bias, therefore $\hat{\boldsymbol{b}}_k = \hat{\boldsymbol{b}}_{k-1}$.

To predict the error covariance $\hat{\boldsymbol{P}}_k$ use

$$\hat{\boldsymbol{P}}_k = \boldsymbol{A}\boldsymbol{P}_{k-1}\boldsymbol{A}^T + \boldsymbol{Q}, \tag{58}$$

where $\boldsymbol{A}$ is the state transition matrix, and $\boldsymbol{Q}$ is the process error. The matrix $\boldsymbol{A}$ can be described by

$$\boldsymbol{A} = \begin{bmatrix} \boldsymbol{\Theta} & \boldsymbol{\Psi} \\ \boldsymbol{0}_3 & \boldsymbol{I}_3 \end{bmatrix}. \tag{59}$$

Using the linearized approximations given in Trawny and Roumeliotis (2005) $\boldsymbol{\Theta}$ and $\boldsymbol{\Psi}$ are given by

$$\begin{aligned} \lim_{|\hat{\boldsymbol{\omega}}\Delta t|\rightarrow 0} \boldsymbol{\Theta} &= \boldsymbol{I}_3 - \Delta t\lfloor\hat{\boldsymbol{\omega}}\times\rfloor + \frac{\Delta t^2}{2}\lfloor\hat{\boldsymbol{\omega}}\times\rfloor^2, \quad \text{and} \\ \lim_{|\hat{\boldsymbol{\omega}}\Delta t|\rightarrow 0} \boldsymbol{\Psi} &= -\boldsymbol{I}_3\Delta t + \frac{\Delta t^2}{2}\lfloor\hat{\boldsymbol{\omega}}\times\rfloor - \frac{\Delta t^3}{6}\lfloor\hat{\boldsymbol{\omega}}\times\rfloor^2. \end{aligned} \tag{60}$$

Linearizations are used to avoid computer computational instability from $\frac{\sin\boldsymbol{\omega}}{\boldsymbol{\omega}}$ and $\frac{\cos\boldsymbol{\omega}}{\boldsymbol{\omega}}$ that appear in the exact form solutions. An independent derivation of the state transition matrix $\boldsymbol{A}$ is shown in the Appendix to this thesis on page 138.

For $\boldsymbol{Q}$, use the discrete noise covariance $\boldsymbol{Q}_d$ from Trawny and Roumeliotis (2005).

$$\boldsymbol{Q}_d = \begin{bmatrix} \boldsymbol{Q}_{11} & \boldsymbol{Q}_{12} \\ \boldsymbol{Q}_{12}^T & \boldsymbol{Q}_{22} \end{bmatrix}. \tag{61}$$

$$\lim_{|\hat{\boldsymbol{\omega}}\Delta t|\to 0} \boldsymbol{Q}_{11} = \sigma_1^2 \Delta t \boldsymbol{I}_3 + \sigma_2^2 (\boldsymbol{I}_3 \frac{\Delta t^3}{3} + \frac{2\Delta t^5}{5!} \lfloor \hat{\boldsymbol{\omega}} \times \rfloor^2). \tag{62}$$

$$\lim_{|\hat{\boldsymbol{\omega}}\Delta t|\to 0} \boldsymbol{Q}_{12} = -\sigma_2^2 (\boldsymbol{I}_3 \frac{\Delta t^2}{2} - \frac{\Delta t^3}{3!} \lfloor \hat{\boldsymbol{\omega}} \times \rfloor + \frac{\Delta t^4}{4!} \lfloor \hat{\boldsymbol{\omega}} \times \rfloor^2). \tag{63}$$

$$\boldsymbol{Q}_{22} = \sigma_2^2 \Delta t \boldsymbol{I}_3. \tag{64}$$

These linearizations are valid for small $\hat{\delta} q_{k-1}$, meaning small $\hat{\boldsymbol{\omega}}\Delta t$, which is expected for 200 Hz DMP rates on ISS. The propagation step is repeated for the 200 Hz dead reckoning until an absolute attitude update interrupts.

#### *3.3.2.3 Update Measurement and Covariance*

The goal of the measurement update step is to derive new estimates $\hat{q}_k$ and $\hat{\boldsymbol{b}}_k$ by incorporating absolute measurements from the SA. Matrix $\boldsymbol{H}$ is referred to as the observational model, or how a state vector translates to a measurement vector. In this case, $\boldsymbol{H}$ extracts the modified Rodrigues measurements from the state vector. An absolute measurement $\boldsymbol{z}_k$ can be thought of as an absolute measurement of modified Rodrigues attitude parameters with respect to ICRF coordinates plus measurement noise such that

$$\boldsymbol{z}_k \equiv \boldsymbol{H}\boldsymbol{x}_k + \boldsymbol{\nu}. \tag{65}$$

With this in mind, $\boldsymbol{H}$ is defined as

$$\boldsymbol{H} \equiv \begin{bmatrix} \boldsymbol{I}_3 & \boldsymbol{0}_3 \end{bmatrix}. \tag{66}$$

The absolute attitude covariance matrix $\boldsymbol{R}_k$ is defined as

$$\boldsymbol{R}_k \equiv E\left[\boldsymbol{\nu}_k \boldsymbol{\nu}_k^T\right], \tag{67}$$

constructed of the standard deviations $\boldsymbol{\nu}_k$ of the measurement white noise in $\boldsymbol{z}_k$.

When an absolute attitude measurement update is provided with variances in $\boldsymbol{R}_k$, the Kalman gain is calculated from Markley (2003) by

$$\boldsymbol{K}_k = \begin{bmatrix} \hat{\boldsymbol{P}}_k^{11} & \hat{\boldsymbol{P}}_k^{12} \end{bmatrix}^T (\hat{\boldsymbol{P}}_k^{11} - \boldsymbol{R}_k)^{-1} \equiv \begin{bmatrix} \hat{\boldsymbol{K}}_k^{11} & \hat{\boldsymbol{K}}_k^{21} \end{bmatrix}^T. \tag{68}$$

In practice an absolute attitude measurement will be a quaternion with respect to ICRF that is denoted as $q_{z,k}$. The state vector $\hat{\hat{\boldsymbol{x}}}$ tracks differences internal to the Kalman filter, so the goal is to find the difference quaternion $\delta q_{z,k}$ between measured attitude $q_{z,k}$ and estimated attitude $\hat{q}_k$. In this case,

$$\delta q_{z,k} \hat{q}_k = q_{z,k} \Rightarrow \delta q_{z,k} = q_{z,k} \hat{q}_k^*. \tag{69}$$

To convert into the modified Rodrigues form with $\delta q_{z,k} \equiv \delta q_{0z,k} + \delta \vec{q}_{z,k}$ use

$$\boldsymbol{z}_k = \frac{4\delta \vec{q}_{z,k}}{1 + \delta q_{0z,k}}. \tag{70}$$

Note that for the first measurement update in a series of measurement updates, state difference $\hat{\hat{\boldsymbol{x}}} \equiv \begin{bmatrix} \hat{\hat{\boldsymbol{a}}} & \hat{\hat{\boldsymbol{b}}} \end{bmatrix}^T = \begin{bmatrix} \vec{\boldsymbol{0}} & \vec{\boldsymbol{0}} \end{bmatrix}^T$. With successive measurements in a series, $\hat{\hat{\boldsymbol{x}}}$ will be nonzero.

The Kalman gain in Equation 68 can be separated into

$$\begin{aligned} \boldsymbol{K}_k^{11} &= \hat{\boldsymbol{P}}_k^{11} (\hat{\boldsymbol{P}}_k^{11} - \boldsymbol{R}_k)^{-1}, \quad \text{and} \\ \boldsymbol{K}_k^{21} &= \hat{\boldsymbol{P}}_k^{12^T} (\hat{\boldsymbol{P}}_k^{11} - \boldsymbol{R}_k)^{-1}. \end{aligned} \tag{71}$$

Using this notation for $\boldsymbol{K}$ the estimates can be computed as

$$\begin{aligned} \hat{\hat{\boldsymbol{a}}}_{k+1} &= \hat{\hat{\boldsymbol{a}}}_k + \boldsymbol{K}_k^{11} (\boldsymbol{z}_k - \tilde{\boldsymbol{a}}_k), \quad \text{and} \\ \hat{\hat{\boldsymbol{b}}}_{k+1} &= \hat{\hat{\boldsymbol{b}}}_k + \boldsymbol{K}_k^{21} (\boldsymbol{z}_k - \tilde{\boldsymbol{a}}_k), \end{aligned} \tag{72}$$

which updates both the change in attitude and gyro bias. The error covariance is then updated by

$$\begin{aligned} \boldsymbol{P}_{k+1}^{11} &= \hat{\boldsymbol{P}}_k^{11} - \boldsymbol{K}_k^{11}\hat{\boldsymbol{P}}_k^{11}, \\ \boldsymbol{P}_{k+1}^{12} &= \hat{\boldsymbol{P}}_k^{12} - \boldsymbol{K}_k^{11}\hat{\boldsymbol{P}}_k^{12}, \quad \text{and} \\ \boldsymbol{P}_{k+1}^{22} &= \hat{\boldsymbol{P}}_k^{22} - \boldsymbol{K}_k^{21}\hat{\boldsymbol{P}}_k^{12}. \end{aligned} \tag{73}$$

The treatment of the measurement and covariance update in this section, while comprehensive, does not delve into the details of transforming the SA azimuth and elevation angles into an absolute attitude quaternion. This is because constructing this quaternion with respect to the ICRF coordinate frame requires external knowledge. Just as the DMP measurements were incorporated in Section 3.2.3 to calculate SA quaternions used to derive the coordinate transformation, the SA measurements alone are not sufficient information because they lack the clocking component of rotation around the Sun. In this case another absolute measurement or attitude assumption is necessary, whether derived from STK or another source. For example, if it is assumed that the HMA has placed the SAGE III scan head in a correct nadir orientation, then solar scans will be vertical with respect to LVLH. The top and bottom edges of the Sun can then be used to construct an absolute attitude clocking vector, and therefore the SA can provide an absolute attitude correction as a Kalman filter input that will estimate the payload attitude and attitude errors for the limb scattering measurement portion of the orbit. DMP measurements cannot be used to find the missing component of rotation because as previously discussed DMP data are relative measurements, not absolute. There are no other absolute attitude measurements available from the SAGE III subsystems. This does not present a problem, however, because as previously mentioned, the MEKF will not be used onboard the payload and is not used for real time attitude decision making. The scope of this thesis does not include the selection of an external absolute measurement source or the details of how the attitude quaternion is constructed. This is left as future work. The Kalman filter

as constructed above will of course quantify the attitude errors associated with the method chosen on orbit.

#### *3.3.2.4 Reset the State*

As described in Markley (2003), following a series of absolute measurements the attitude quaternion and gyro bias need to be stored outside of the filter, and the state vector needs to be reset. The process of updating the attitude quaternion is similar to the steps laid out in Equations 55–57. The difference quaternion is constructed by

$$\hat{\delta}q(\hat{\tilde{\boldsymbol{a}}}_{k+1}) = \begin{bmatrix} \dfrac{16 - a_{k+1}^2}{16 + a_{k+1}^2} \\ \dfrac{8\hat{\tilde{\boldsymbol{a}}}_{k+1}}{16 + a_{k+1}^2} \end{bmatrix}, \tag{74}$$

where $a_{k+1}^2 \equiv |\hat{\tilde{\boldsymbol{a}}}_{k+1}|^2$. Next, the attitude quaternion is propagated and normalized for computer roundoff error using Equations 75 and 76, respectively.

$$\hat{q}_{k+1} = \hat{\delta}q(\hat{\tilde{\boldsymbol{a}}}_{k+1})\hat{q}_k. \tag{75}$$

$$\hat{q}_{k+1} \rightarrow \frac{\hat{q}_{k+1}}{|\hat{q}_{k+1}|}. \tag{76}$$

The bias from Equation 72 is stored as

$$\hat{\boldsymbol{b}}_{k+1} = \hat{\boldsymbol{b}}_k + \hat{\tilde{\boldsymbol{b}}}_{k+1}. \tag{77}$$

Finally, the state vector is reset after the series of absolute measurements, but before returning to propagate the DMP state, with

$$\hat{\tilde{\boldsymbol{x}}}_{k+1} \equiv \begin{bmatrix} \hat{\tilde{\boldsymbol{a}}}_{k+1} \\ \hat{\tilde{\boldsymbol{b}}}_{k+1} \end{bmatrix} = \begin{bmatrix} \vec{0} \\ \vec{0} \end{bmatrix}. \tag{78}$$

As can be seen in Figure 19, after a reset the state propagation and covariance prediction step is entered again until additional absolute measurements are available.

The general flow of the MEKF as applied to SAGE III ISS is dead reckoning propagation using DMP measurements for approximately half an ISS orbit followed

by an approximately three minute time period of absolute SA solar measurements. This is repeated twice per orbit, once for a Sunrise event and once for a Sunset. In post processing, the low pass digital Kalman filter can be run forward in time on the data set, then run backward in time on the corrected data set to improve the time series attitude estimates and reduce the noise. Multiple forward and backward passes of the filter may be tried to improve the estimate and reduce the attitude discontinuities at the measurement updates.

# CHAPTER IV

# RESULTS

This chapter presents the implementation and analysis of the coordinate transformation algorithm described in Chapter 3. A discussion of algorithm performance, accuracy criteria, and future on-orbit applications are provided herein.

## *4.1 Algorithm Performance Criteria and Research Questions*

As previously discussed, it is the author's intent that the method of deriving a coordinate transformation from this thesis be incorporated into the SAGE III science inversion algorithm illustrated in Figure 4 on page 12 once SAGE III is on orbit. The coordinate transformation is also an integral part of the measurement update portion of the Kalman filter.

Several criteria must be considered to verify the accuracy and applicability of the algorithm for use during on-orbit operations. The first consideration is the error in the derived transformation quaternion between the DMP and SA coordinate systems. Table 6 defines the simulation parameters used to construct the DMP axes described in Section 3.1.4. The nominal orthogonal RLG configuration and two hypothetical non-orthogonal configurations were tested to explore how non-orthogonality would manifest itself during the calibration process. Provided in the table is the expected angular offset of each axis from nominal to quantify the non-orthogonality of each coordinate system tested. These offsets represent a rotation from the orthogonal axes. The orientations of both the DMP and SA are known and explicitly defined in the simulation prior to the addition of measurement noise and simulation runs, so the error in the final derived transformation quaternion is directly calculated from the

**Table 6: Defined Coordinate Systems and Expected Angular Error.** The STK DMP axes definitions are described by the matrices. The expected angular error is the angular difference between the standard axis and the non-orthogonal axis.

| DMP Definition | Defined Matrix | Expected Angular Error |
|---|---|---|
| Orthogonal | $\begin{bmatrix} 1 & 0 & 0 \\ 0 & 1 & 0 \\ 0 & 0 & 1 \end{bmatrix}$ | 0° |
| Non-orthogonal Small Error | $a = 0.99999995769203$, $b = 0.00020568902198$ $\begin{bmatrix} a & b & b \\ b & a & b \\ b & b & a \end{bmatrix}$ | X: 0.017° Y: 0.017° Z: 0.017° |
| Non-orthogonal Large Error | $\begin{bmatrix} 1 & 0.02 & 0.01 \\ 0.02 & 1 & 0.02 \\ 0.03 & 0.01 & 1 \end{bmatrix}$ | X: 1.281° Y: 1.620° Z: 1.811° |

known transformation quaternion. A statistical analysis of the errors in the derived coordinate transformation quaternions and the sampling dependence of reaching acceptable levels of angular error will be presented, thus illustrating that the estimation technique is sufficiently accurate.

Angular error in the coordinate transformation is found for each axis by rotating a given DMP axis unit vector, $\hat{\boldsymbol{D}}_{\boldsymbol{i}}$, by the calculated coordinate transformation, $q$, and finding the angle between the resulting rotated axis and the respective SA axis, $\hat{\boldsymbol{S}}_{\boldsymbol{i}}$.

$$\text{angular error} = \arccos\left[(q\ \hat{\boldsymbol{D}}_{\boldsymbol{i}}\ q^*) \cdot \hat{\boldsymbol{S}}_{\boldsymbol{i}}\right], \quad \text{for } i \in \{x, y, z\}. \tag{79}$$

Total angular error is found using the scalar term of the quaternion and Equation 31 on page 52. The angular error is expected to decrease as the number of rotation axis pairs used to calculate an average coordinate transformation increases, meaning the transformation error will decrease with time as the mission progresses. The goal imposed by the SAGE III DMP science team is to continue increasing the number

of occultation samples to produce a quaternion representing a coordinate transformation with less than 60 arcseconds of total error. This allows the total error and Monte Carlo error bars to be plotted as a function of total combinations of rotation axes to assess the amount of time needed on orbit to achieve a specified error. The 60 arcsecond goal is not an alignment requirement for the mission, but rather represents an insignificant coordinate transformation error and sets a limit to govern the number of statistical runs that will be performed during the present research. More importantly, this is an assessment of the validity of the method chosen to derive a coordinate transformation—a method in which the total SA attitude is dependent on the total rotation measured by the DMP. Given the measurement noise constraints of Table 3 on page 25, 60 arcseconds of coordinate transformation error can only be achieved through sufficiently unbiased statistical sampling.

Answers to the following questions for on-orbit operation can be derived from analysis of the orbit simulation:

- How many samples (or solar occultation events) are needed to derive a coordinate transformation of a specified accuracy?
- How does the derived transformation change with different ISS orientations, and are any exclusions needed?
- How does measurement noise impact the coordinate transformation?
- If DMP axes are non-orthogonal, how does this impact the coordinate transformation, and how does it manifest in the data?

The following sections will answer these questions with the goal of incorporating the coordinate transformation in the SAGE III algorithm post-launch.

## *4.2 Effects of ISS Orientation, Beta Angle, and Apparent Sun Motion*

Several key factors impact the results presented in the subsequent sections, namely ISS orientation, beta angle, and apparent Sun drift during occultation events. ISS orientation during an occultation event dictates the coordinate orientations of the measured SA and DMP total rotation axes used in the fast quaternion estimation method described in Section 3.2. It was found during this investigation that the accuracy of the derived coordinate transformation is highly dependent upon the angular separation between the pairs of SA and pairs of DMP quaternion vector components selected. This can be expected, since a pair of total rotation axes measured by the DMP during two occultation events can be thought of as defining a plane for the coordinate transformation to match with the plane defined by the corresponding pair of SA rotation axes. For a given solar beta angle, the ISS orientation determines the angular separation between pairs of measured rotation axes. The errors in the plane orientations are more significant for small separations between the axes that define the planes—meaning a steady ISS TEA will result in larger derived coordinate transformation error because the axis of total ISS rotation will only change marginally. A coordinate transformation derived using SA or DMP quaternion vector component pairs with either an angular separation of approximately 0° or approximately 180° degrees is suboptimal compared to one found with an angular separation between those two extremes. As an example, consider a plane defined by two vectors each having measurement noise of $\approx 1$ arcsecond. If the two vectors were 90° separated, then the error in the orientation of the plane in which they rest would be very small compared to the case where the vectors were separated by only 0.01 arcseconds, which is much smaller than the measurement noise. A similar situation is encountered when the vectors are almost exactly 180° separated.

Figure 20 illustrates both the prevalence of this problem and favorable conditions

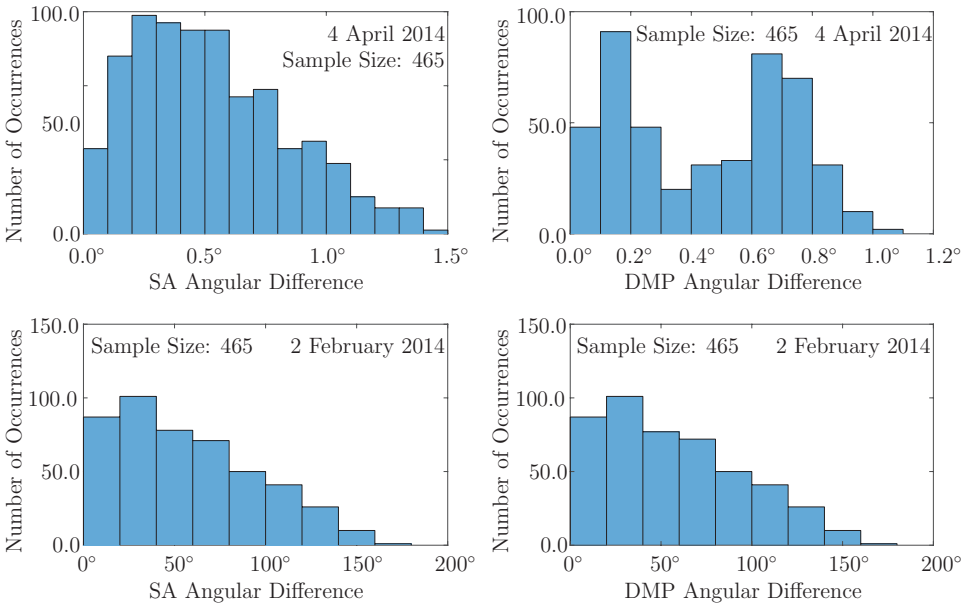


**Figure 20: Number of Occurrences by Angular Separation of Pairs.** The angular separations between pairs of SA and DMP measured rotation axes used for the fast quaternion estimation are shown for all combinations that can be made over a single day for both 4 April and 2 February 2014.

under which this situation can be avoided. A single solar occultation event will yield one measurement by the DMP and one measurement by the SA of the total ISS rotation during the exoatmospheric scans. The same axis of rotation is therefore measured in the DMP coordinate system and in the SA coordinate system. The fast quaternion estimation method described in Section 3.2 requires measurements in each coordinate system of two linearly independent rotation axes to fully define a transformation quaternion. So a pair of occultation measurements having linearly independent total rotation axes must be used to fully constrain the coordinate transformation. The histograms in Figure 20 show the angular differences in pairs of DMP and SA rotation axes formed by all combinations available on a given day. When using events with similar ISS orientations, the angular difference is quite small, often less than 1° as shown in the histograms of angular separation for 4 April 2014 displayed in the top panels of the figure. This occurs because the axis of rotation for the ISS is stable

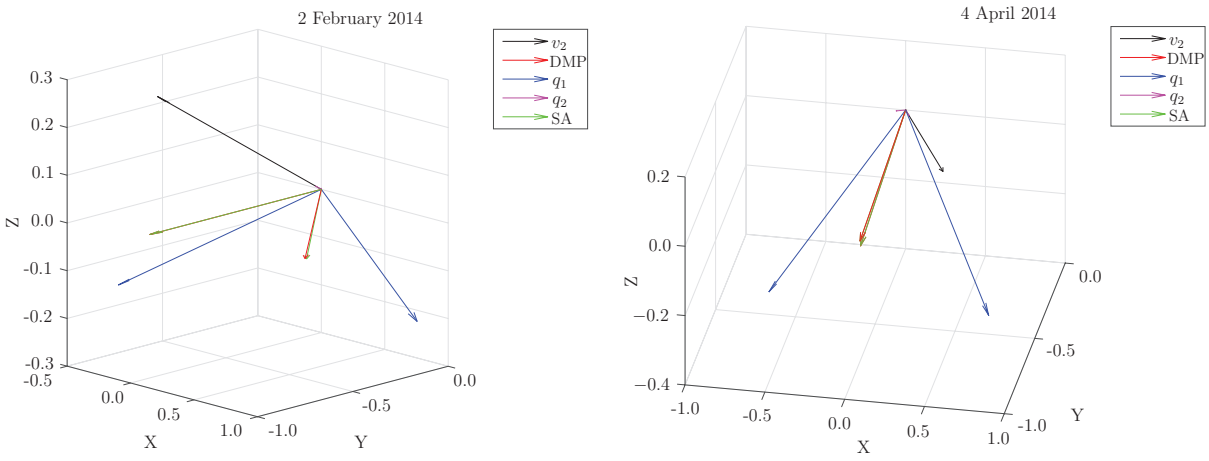


**Figure 21: Visualization of Vector Angular Separation.** Separation between SA and DMP vectors pairs used for fast quaternion estimation on 4 April and 2 February 2014.

for nominal TEA conditions. During extreme ISS maneuvers, however, the angular separation can span the entire range between 0° and 180°, as illustrated in the bottom panels of the figure for 2 February 2014.

Shown another way in Figure 21, the vectors forming the SA pairs and DMP pairs (green and red, respectively) are nearly collocated, such that it appears that only a single SA vector is present for two events on 4 April 2014. In contrast, on 2 February 2014 the vectors rotate mostly about the Z-axis. The $v_1$, $q_1$, and $q_2$ quantities are included in the figure for completeness and to help visualize the construction of the SA quaternion as described in Section 3.2.3.

Analysis of the fast quaternion estimation method as applied to this test configuration indicates that a restriction on the angular separation of the input vectors is necessary. The inclusion of small angular separation cases results in coordinate transformations that do not accurately represent the actual orbital environment. The dependence of coordinate transformation accuracy on the set of available ISS TEAs highlights the importance of obtaining a diverse set of ISS orientations during on-orbit operation, since vector pairs obtained from a single, nominal TEA do not provide sufficient angular separation. The benefits of using various ISS orientations to produce

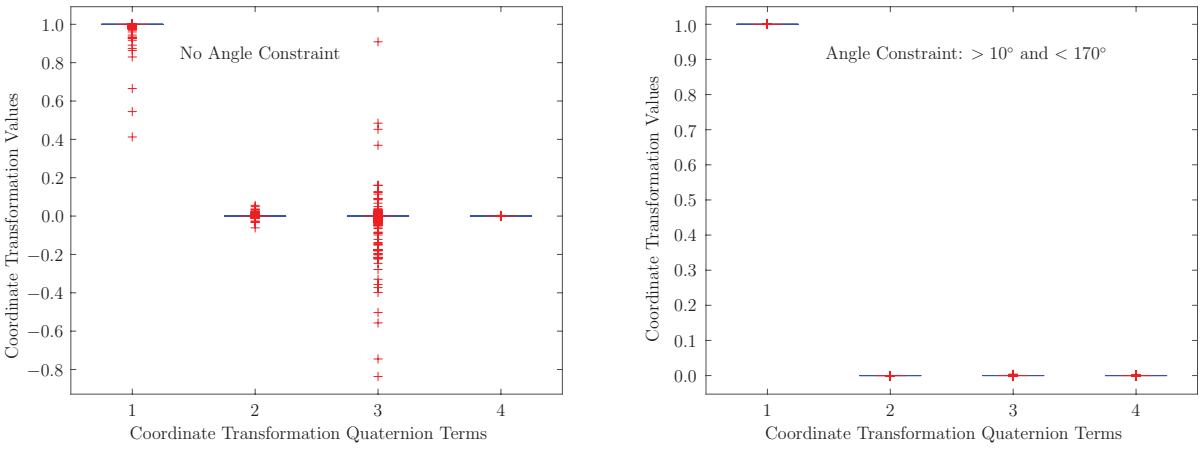


**Figure 22: Box Plots Illustrating the Need for Angle Constraint.** The plot on the left has no angle constraint and the plot on the right uses angular separation greater than 10° and less than 170°.

a stable coordinate transformation over time are presented in Section 4.4.

Figure 22 illustrates both the effectiveness and necessity of applying an angular constraint via box plot of the terms in the coordinate transformation quaternion. The figure is generated using data from 2 February 2014 and 4 April 2014 as sampled in Figures 20 and 21. The applied angle constraint in the right hand box plot of Figure 22 restricts the SA angle difference to within the interval (10°, 170°). The SA vectors were chosen instead of the DMP vectors because the SA showed larger angular separation between events. The expected quaternion based on orthogonal DMP and SA definitions is $[1\ 0\ 0\ 0]^{\mathrm{T}}$ (where T denotes transpose). The largest variance is primarily seen in the scalar and Y-components of the quaternion because there is comparatively little motion observed in the X- and Z-components. The chosen constraint thresholds are conservative cutoffs that balance eliminating error and preserving the total number of samples. An entire order of magnitude of error is reduced in the first 10° of margin, but up to an additional 30° is required for another order of magnitude. It is possible to further optimize the angular separation constraint, but it is left as future work to reevaluate these thresholds on orbit.

As discussed previously in Section 3.1.2, the solar beta angle experienced by

SAGE III will vary greatly during the year, with occultation events constrained to between $-60°$ to $+60°$ solar beta angle. Attitude variations to maintain TEA are expected with changing beta angle. When the beta angle is near zero, the partial quaternion representing clocking, $q_2$ (described in Section 3.2.3), will be at a minimum. Conversely, when beta is at the highest or lowest extreme, the clocking quaternion will be significantly larger than the partial quaternion $q_1$. The apparent Sun motion described in Section 3.2.3.1 is a more significant source of error in the clocking quaternion when beta angle is zero because the rotation represented by $q_2$ will be almost non-existent at zero beta. Using total DMP rotation to solve for clocking, the Sun movement will cause clocking to be either smaller or larger than it actually is by a large percentage (discussed in more detail in Section 4.4.6), supporting the use of the correction. This is a noteworthy source of error for calculations with unmodified STK data.

Finally, the amount of apparent Sun motion changes during the course of the year. The Earth's orbit around the Sun is an ellipse; thus, it does not maintain constant velocity. As the Earth's velocity varies, so does the apparent Sun motion against the fixed stars. Extremes of Sun motion are observed at perihelion and aphelion. The difference between the extremes, however, is slight. The average apparent Sun motion can be calculated by the Earth's mean motion, $n$, using the sidereal period of 365.256 days as

$$n = \frac{360°}{365.256 \text{ days}} = 0.98561009 \frac{°}{\text{day}}. \tag{80}$$

This mean motion corresponds to an average of 7.39 arcseconds for an average three minute solar occultation event. Accounting for orbit perihelion and aphelion, the range of motion is from 7.21 to 7.58 arcseconds over an average event. The apparent Sun motion during an STK event is consistent with these expected numbers. With error on the order of 7 arcseconds it is expected that a Sun motion correction will be necessary on orbit. Since none of the apparent Sun motion is captured by the DMP,

it can be interpreted by the algorithm as entirely affecting Sun clocking. Because the present research seeks to validate the accuracy of the derived technique for finding the coordinate transformation, a comparison will be shown with and without the addition of a correction for the apparent Sun motion.

## *4.3 Description of Analysis Methods*

The results presented in Sections 4.4.1 through 4.4.4 vary the inclusion of Gaussian error and the apparent Sun motion correction one variable at a time. Although each case is unique, the presentation follows a standard format. First, the mean, median, and standard deviation, referred to as the standard statistics, are examined for each term in the coordinate transformation quaternion. Then, a Monte Carlo analysis of total angular error and angular error for each coordinate axis is performed. Percentage error is not calculated for the mean and median of the three zero-value quaternion terms because percentage error is undefined for a "true" value of zero. Therefore, only absolute error is considered for these terms.

One of the goals of this analysis is to determine the number of samples necessary to produce a stable and accurate transformation quaternion. The fast quaternion estimation method requires two pairs of vectors, one pair derived from SA quaternions, and the other pair from corresponding DMP quaternions. With $n$ sample measurements the number of DMP/SA parings are found by

$$\text{number of comparisons} = \frac{n(n-1)}{2}. \tag{81}$$

The word "comparison" is used to describe the number of total coordinate transformations that can be formed by sampling $n$ DMP/SA vector pairs without replacement. The possible number of pairs is captured by $n(n-1)$ and the uniqueness is captured by the division by two because vector pairs (A, B) and (B, A) are not unique. Each vector is a sample that is used more than once in combination with other vectors. For

the full suite of 15 days in Table 5 there are 104,653 possible coordinate transformations using every combination of SA and DMP vectors. Applying the aforementioned angle constraint, this number decreases to 19,946 possible combinations, or a reduction to approximately 20%. The 15 days selected are representative of the wide range of beta angles ($-57.83°$ to $57.58°$) at which SAGE III can obtain occultation data. Also present are large ISS maneuvers representative of the conditions that can be experienced on orbit.

The presented Monte Carlo simulations calculate a mean coordinate transformation using a varied number of random pairings of SA vectors with the corresponding DMP vector pairs. Each vector pair is from a single solar event. As an example case, a subset of 1,000 quaternion vector pairs is randomly sampled from the set of all possible angle-constrained SA measurement pairings. The corresponding DMP measurement pairs are then retrieved, and a quaternion-averaged coordinate transformation is derived. This process is carried out for a sample space ranging from 2 to 75,000 comparisons. The method and considerations for calculating an average quaternion are presented in Section 2.2. Each Monte Carlo case is run 1,000 times to generate statistics on the mean of the distribution of coordinate transformations.

## *4.4 Results*

Analysis of the coordinate transformation algorithm described in Chapter 3 and shown in Figure 3.2.4 is performed using STK simulated data with and without apparent Sun motion correction, with noise introduced on the order expected on orbit, and with non-orthogonal DMP axes. Analysis of error around the Sun vector is also provided.

### 4.4.1 Unmodified STK Data

Using the process described in Chapter 3 the coordinate transformation quaternion is found as the mean coordinate transformation of all combinations of axes from simulated STK data for all days in Table 5 on page 42. Only rotation axes separated by

an angular range of 10° to 170° are paired. Key quaternion statistics are summarized in the first half of Table 7. The mean and median are shown for each term in the quaternion. The error in each term from the expected unity quaternion $[1\ 0\ 0\ 0]^{\mathrm{T}}$ is, at worst, on the order of 0.000135. The largest standard deviation is observed in the Y-term. This is most likely because the majority of the ISS motion is around the Y-axis, since the Y-axis is nearly normal to the orbital plane.

Because the sampled quaternion components are not normally distributed, a Student's t-test is not the correct tool to test statistical hypotheses. Therefore, the Wilcoxon signed-rank test (Wilcoxon, 1945) is used to non-parametrically test if the mean of each term is statistically identical to zero and if the mean and median are statistically different. The scalar quaternion term is converted to angle space for this test using Equation 31. With a p-value of less than 0.006 the null hypothesis that the mean of each parameter is statistically identical to zero is rejected for all four quaternion terms to 98.8% significance. This suggests that a statistically meaningful error in the coordinate transformation exists and warrants further characterization. The mean and median for all four terms are not statistically different with a p-value of 1.0, suggesting that distribution of errors is not skewed. A more complete description of distribution skewness will be provided in subsequent sections.

Table 8 is created by running 1,000 Monte Carlo simulations that calculate an average quaternion constructed by random pairings of DMP and SA vectors for each of the displayed number of comparisons: 2, 10, 100, 500, 1,000, and 10,000 comparisons per mean. No measurement noise is included, and no correction for the apparent Sun position was used. The quantities of interest that result from this analysis are the total angular error (error in the scalar term) and angular error in each of the X-, Y-, and Z-axes. The Monte Carlo standard deviation is also included for each quantity. Angular error as discussed in Section 4.1 is reported in both degrees and arcseconds.

At 500 comparisons in a mean the 60 arcsecond goal is met for total error and error

**Table 7: Coordinate Transformation Statistics With No Sun Correction.** The table lists a summary of statistics for the coordinate transformation quaternion terms derived using STK data for all days in Table 5 on page 42 with and without expected Gaussian noise introduced into the SA measurement system.

| Quaternion Statistics | Scalar Term | X-term | Y-term | Z-term |
|---|---|---|---|---|
| **Without Noise** | | | | |
| **Mean** | 0.999999990897231 | $9.24414976316018 \times 10^{-6}$ | 0.000134586383104 | $2.56690747529319 \times 10^{-6}$ |
| **Median** | 0.999999994658830 | 0.000022693736186 | 0.000100669349005 | $5.74604021232447 \times 10^{-6}$ |
| **Standard Deviation** | $4.86166080896281 \times 10^{-6}$ | 0.000385053570620 | 0.000846867364284 | 0.000711924756268 |
| **With Noise** | | | | |
| **Mean** | 0.999999985790585 | 0.000141806308887 | 0.000091122911224 | $2.53280581855259 \times 10^{-6}$ |
| **Median** | 0.999999959042587 | 0.000248206042264 | 0.000141014561167 | −0.000020578605702 |
| **Standard Deviation** | 0.000168923572443 | 0.003559860926845 | 0.009881135093880 | 0.001446109055304 |

**Table 8: Monte Carlo Results Using Unmodified STK Data.** The mean angular error and standard deviation of the error for 1,000 Monte Carlo runs for various numbers of rotation axis pairings reveals how the error decreases with an increasing number of unique pairings. For a number of comparisons $\frac{1}{2}n(n-1)$ only $n$ occultation events are needed.

| **Number of Comparisons in Mean** | **2** | **10** | **100** | **500** | **1,000** | **10,000** |
|---|---|---|---|---|---|---|
| **Total Angular Error (°)** | 0.067212727 | 0.044035781 | 0.021980601 | 0.016800404 | 0.016141166 | 0.015563934 |
| **Total Angular Error (arcseconds)** | 242 | 159 | 79 | 60 | 58 | 56 |
| **Total Angular Error Std (°)** | 0.14461104 | 0.045193517 | 0.010695409 | 0.005958281 | 0.004371413 | 0.001321591 |
| **X-axis Angular Error (°)** | 0.061362115 | 0.041089765 | 0.020798869 | 0.016674547 | 0.015926012 | 0.015500738 |
| **X-axis Angular Error (arcseconds)** | 220 | 148 | 75 | 60 | 57 | 56 |
| **X-axis Angular Error Std (°)** | 0.116202673 | 0.04575448 | 0.010620767 | 0.005848558 | 0.00435223 | 0.001373606 |
| **Y-axis Angular Error (°)** | 0.04258492 | 0.027056963 | 0.011067084 | 0.005156179 | 0.003808932 | 0.001576871 |
| **Y-axis Angular Error (arcseconds)** | 153 | 97 | 40 | 19 | 14 | 6 |
| **Y-axis Angular Error Std (°)** | 0.085036486 | 0.029779876 | 0.006777779 | 0.002864624 | 0.00210708 | 0.000706907 |
| **Z-axis Angular Error (°)** | 0.049652852 | 0.034358269 | 0.018598354 | 0.016086255 | 0.015631548 | 0.015500848 |
| **Z-axis Angular Error (arcseconds)** | 178 | 124 | 67 | 58 | 56 | 56 |
| **Z-axis Angular Error Std (°)** | 0.098397897 | 0.041767839 | 0.010319293 | 0.005974009 | 0.004410909 | 0.001371771 |

in each axis. Although, taking into account standard deviation the 10,000 comparison case is the best choice because at the worst-case the angular error is 61 arcseconds for total angular error. The trend of the angular errors and their associated standard deviations continue to substantially decrease with increasing number of comparisons implying that true stability is achieved at a higher number of comparisons than is necessary to meet the angular error goal.

The Y-axis angular error is the smallest out of the three axes. The total, X-axis, and Z-axis error values are comparable. The same results are observed in the standard deviation terms. The rate of error convergence follows a power fit. The angular errors (with the exception of the Y-axis) decrease approximately raised to the $-0.1$ power, whereas the angular error standard deviations decrease approximately to the $-0.5$ power. The Y-axis angular error is unique and decreases to a power of approximately $-0.4$. The exact values of these convergence trends are not of particular importance. The trends are used to estimate the number of samples needed for a given coordinate transformation accuracy constraint when the instrument is on orbit.

### 4.4.2 Gaussian Error Added To SA Measurement

The case presented in Section 4.4.1 provides a needed baseline of comparison, but does not accurately reflect on-orbit conditions. To simulate more flight-like conditions the same analysis is performed with Gaussian measurement errors introduced. Using values in Table 3 on page 25, noise on the order of the actual measurement error found during instrument characterization is added to the azimuth and elevation positions reported from STK. Error is not introduced for the DMP measurements. ARW can be an important source of error for the gyroscopes, but not for the DMP within the three minutes or so that is experienced during a solar event. This error is expected to be 0.432 arcseconds in the worst case over the course of a three minute science event,

which is less than 0.5% of the SA error.

With the addition of Gaussian error, the same process of calculating coordinate transformation quaternions is followed as in Section 4.4.1 for the 15 test days. Key quaternion statistics are summarized in the second half of Table 7. The mean and median are shown for each term in the quaternion. The error in each term from the expected unity quaternion $[1\ 0\ 0\ 0]^{\mathrm{T}}$ is, at worst, on the order of 0.000248. Compared to Section 4.4.1 without noise, the scalar term is about 1 arcminute from ideal and the standard deviation increased three orders of magnitude. The X-term value and standard deviation increased by one to two orders of magnitude. The Y-term mean and median values are similar in both cases, but the standard deviation increased by an order of magnitude. The Z-term mean is almost the same in both cases and the standard deviation increased by a factor of two. A distinct increase in error between the noisy and noiseless cases is expected considering the level of Gaussian error injected into the measurements. The azimuth noise is the most significant with $1\sigma$ error of 2 arcminutes.

As discussed in the previous section, a Wilcoxon signed-rank test is used to non-parametrically assess the statistical hypotheses that the mean of each term is statistically identical to zero and the mean and median are statistically different. The scalar quaternion term is converted to angle space for this test using Equation 31. With a p-value of less than 0.0001 the null hypothesis that the mean of each parameter is statistically identical to zero is rejected for all four quaternion terms. This suggests that a statistically meaningful error in the coordinate transformation exists and warrants further characterization. The mean and median for all four terms are not statistically different with a p-value of 1.0, suggesting that distribution of errors is not skewed. The statistics on the mean and median provide insight into the distribution of quaternion terms, but the forthcoming Monte Carlo simulations provide a clearer understanding of stability and accuracy.

Similar to Section 4.4.1, Table 9 is created by running 1,000 Monte Carlo simulations for each of the displayed number of comparisons: 2, 10, 100, 500, 1,000, 10,000, and 50,000 comparisons per mean. The quantities of interest are the total angular error (error in the scalar term) and angular error in each of the X-, Y-, and Z-axes. The standard deviation is also included for each quantity.

The 60 arcsecond goal on the mean is not met by any of the combinations for the total angular error. The goal was set by the DMP science team as the low limit for generating a plot of the coordinate transformation total error as a function of number of rotation axis pairings. Although the total angular error decreases as expected with an increasing number of comparisons in the mean, with the level of error in the combined azimuth and elevation positions, this shortcoming seems an inevitability for the number of comparisons that can be made with the currently available simulated data set. The quaternion generated with 50,000 comparisons in the mean has on average 73 arcseconds of total angular error. With the same level of instrumentation error in the azimuth and elevation positions on orbit, it is expected that a similar error will be achieved with 317 solar occultation events with total event rotation axes that are sufficiently linearly independent, or about 10 days worth of occultation data distributed over at least one full beta cycle. The X- and Y-axis angular errors drop below the 60 arcsecond goal, whereas the Z-axis error is on par with the total angular error.

With Gaussian noise added to the SA data, the convergence for the angular errors range from the power of $-0.28$ to $-0.41$. The rate of error convergence for the standard deviations are consistent with Table 8 following a power of $-0.5$. Compared to Table 8, the angular errors achieved at high number of comparisons per mean are about a 30% increase.

**Table 9: Monte Carlo Results With Added Gaussian Measurement Noise.** The mean angular error and standard deviation of the error for 1,000 Monte Carlo runs for various numbers of rotation axis pairings reveals how the error decreases with an increasing number of unique pairings. For a number of comparisons $\frac{1}{2}n(n-1)$ only $n$ occultation events are needed.

| **Number of Comparisons in Mean** | **2** | **10** | **100** | **500** | **1,000** | **10,000** | **50,000** |
|---|---|---|---|---|---|---|---|
| **Total Angular Error (°)** | 0.794254888 | 0.449496259 | 0.144350259 | 0.069991302 | 0.049257299 | 0.024225753 | 0.020349765 |
| **Total Angular Error (arcseconds)** | 2859 | 1618 | 520 | 252 | 177 | 87 | 73 |
| **Total Angular Error Std (°)** | 0.762335345 | 0.350348145 | 0.08796482 | 0.04196589 | 0.027021546 | 0.008961589 | 0.004006864 |
| **X-axis Angular Error (°)** | 0.696344352 | 0.380277769 | 0.130783777 | 0.060797922 | 0.042257581 | 0.016171822 | 0.010885224 |
| **X-axis Angular Error (arcseconds)** | 2507 | 1369 | 471 | 219 | 152 | 58 | 39 |
| **X-axis Angular Error Std (°)** | 0.888185587 | 0.341141284 | 0.095458644 | 0.043495704 | 0.030381557 | 0.01150169 | 0.006314932 |
| **Y-axis Angular Error (°)** | 0.322452756 | 0.15919637 | 0.053038391 | 0.02717322 | 0.022214362 | 0.016452212 | 0.016322214 |
| **Y-axis Angular Error (arcseconds)** | 1161 | 573 | 191 | 98 | 80 | 59 | 59 |
| **Y-axis Angular Error Std (°)** | 0.272494952 | 0.125376504 | 0.033995859 | 0.016947196 | 0.013554645 | 0.005754682 | 0.002581123 |
| **Z-axis Angular Error (°)** | 0.808326 | 0.427216659 | 0.144148603 | 0.068494861 | 0.049407919 | 0.024604347 | 0.020341742 |
| **Z-axis Angular Error (arcseconds)** | 2910 | 1538 | 519 | 247 | 178 | 89 | 73 |
| **Z-axis Angular Error Std (°)** | 0.871343103 | 0.331885247 | 0.09163994 | 0.041357878 | 0.028791657 | 0.009031018 | 0.003891724 |

### 4.4.3 Unmodified STK Data With Apparent Sun Motion Correction

To provide another baseline case, the apparent Sun motion correction described in Sections 3.2.3.1 and 4.2 is applied to the STK data without the addition of Gaussian noise. It was expected that this case should be an improvement over the results from Section 4.4.1.

With the addition of an apparent Sun motion correction, the same process of calculating coordinate transformation quaternions is followed as in Section 4.4.1 for the 15 test days. Key statistics for the quaternions are summarized in the first half of Table 10. The mean and median are shown for each term in the quaternion. The error in each term from the expected unity quaternion $[1\ 0\ 0\ 0]^{\mathrm{T}}$ is, at worst, on the order of $4.48 \times 10^{-5}$. The results are consistent with the case with no noise and no Sun correction in Section 4.4.1. All variation between the two cases are well within the standard deviations, and the standard deviations are almost identical for the vector terms of the quaternion. There is improvement in the scalar term for the Sun corrected case, but the difference is not statistically significant at the 95% confidence level. Although the purpose of a Sun correction is to improve the quaternion end result, it is entirely possible that the additional computation and roundoff errors associated with a correction offset the improvement.

As discussed in previous sections, a Wilcoxon signed-rank test is used to non-parametrically assess the statistical hypotheses that the mean of each term is statistically identical to zero, and the mean and median are statistically different. The scalar quaternion term is converted to angle space for this test using Equation 31. With a p-value of less than 0.0001 the null hypothesis that the mean of each parameter is statistically identical to zero is rejected for all four quaternion terms. This suggests that a statistically meaningful error in the coordinate transformation exists and warrants further characterization. The mean and median for all four terms are not statistically different with a p-value of 1.0, suggesting that distribution of errors

**Table 10: Coordinate Transformation Statistics With Sun Correction.** The table lists a summary of statistics for the coordinate transformation quaternion terms derived using STK data for all days in Table 5 on page 42 with an apparent Sun motion corrected applied, with and without expected Gaussian noise introduced into the SA measurement system.

| Quaternion Statistics | Scalar Term | X-term | Y-term | Z-term |
|---|---|---|---|---|
| **Without Noise** | | | | |
| **Mean** | 0.999999998488916 | 0.000025214382134 | 0.000043083909140 | 0.000023025612807 |
| **Median** | 0.999999998806016 | $-1.83110751505291 \times 10^{-6}$ | 0.000044818349847 | 0.000019388934372 |
| **Standard Deviation** | 0.000011996469554 | 0.000423606261702 | 0.000810615810932 | 0.000704739944005 |
| **With Noise** | | | | |
| **Mean** | 0.999999982681914 | 0.000136851185992 | 0.000035969195680 | 0.000120888966805 |
| **Median** | 0.999999970504722 | 0.000235342109096 | 0.000059166511302 | −0.000010196650866 |
| **Standard Deviation** | 0.000169453243020 | 0.003537277855406 | 0.009826620398051 | 0.001397479947816 |

is not skewed.

Similar to Section 4.4.1, Table 11 is created by running 1,000 Monte Carlo simulations for each of the displayed number of comparisons: 2, 10, 100, 500, 1,000, 10,000, and 50,000 comparisons per mean. The quantities of interest are the total angular error (error in the scalar term) and angular error in each of the X-, Y-, and Z-axes. The standard deviation is also included for each quantity.

At 100 comparisons in a mean the 60 arcsecond goal is met, although this can be further reduced with larger comparison size. Taking into account standard deviation, the 500 comparisons has a worst-case angular error of 50 arcseconds. This is an improvement over the number of comparisons needed in Section 4.4.1. Unlike the results in Table 10, the Sun correction provides significant improvement over the case with no correction when averaging several comparisons. Similar to Section 4.4.1 the Y-axis angular error is smaller than the total, X-, and Z-axis errors. The standard deviations for all four errors are increasingly similar with larger comparison size.

With the apparent Sun correction applied the rate of angular error convergence follows a fit raised to the power of $-0.16$ and $-0.5$ for the standard deviations. These results are consistent with the trends in Section 4.4.1.

### 4.4.4 Gaussian Error Added To SA Measurement With Sun Correction

The case presented in Section 4.4.3 provides a baseline for the addition of an apparent Sun motion correction. To simulate more flight-like conditions the same analysis is performed with Gaussian error introduced to the SA measurements. Similar to Section 4.4.2, the values in Table 3 on page 25 are used to add noise on the order of the error observed during instrument characterization to the azimuth and elevation positions reported from STK. Error is not introduced for the DMP measurements.

With the addition of both Gaussian error and apparent Sun motion corrections, the same process of calculating coordinate transformation quaternions is followed as

**Table 11: Monte Carlo Results With Sun Correction But Without Gaussian Measurement Noise.** The mean angular error and standard deviation of the error for 1,000 Monte Carlo runs for various numbers of rotation axis pairings reveals how the error decreases with an increasing number of unique pairings. For a number of comparisons $\frac{1}{2}n(n-1)$ only $n$ occultation events are needed.

| **Number of Comparisons in Mean** | **2** | **10** | **100** | **500** | **1,000** | **10,000** | **50,000** |
|---|---|---|---|---|---|---|---|
| **Total Angular Error (°)** | 0.039234518 | 0.029178125 | 0.015873309 | 0.009411137 | 0.008033540 | 0.006466470 | 0.006317047 |
| **Total Angular Error (arcseconds)** | 141 | 105 | 57 | 34 | 29 | 23 | 23 |
| **Total Angular Error Std (°)** | 0.150993216 | 0.054294139 | 0.014573675 | 0.004481264 | 0.003279593 | 0.001132224 | 0.000506610 |
| **X-axis Angular Error (°)** | 0.030227058 | 0.028045467 | 0.01421512 | 0.008446588 | 0.007268957 | 0.005759637 | 0.005609217 |
| **X-axis Angular Error (arcseconds)** | 109 | 101 | 51 | 30 | 26 | 21 | 20 |
| **X-axis Angular Error Std (°)** | 0.094054015 | 0.063709701 | 0.0124399 | 0.004428192 | 0.003148266 | 0.001134853 | 0.000507663 |
| **Y-axis Angular Error (°)** | 0.018205434 | 0.01864373 | 0.010056674 | 0.005658111 | 0.00488493 | 0.003969239 | 0.003917223 |
| **Y-axis Angular Error (arcseconds)** | 66 | 67 | 36 | 20 | 18 | 14 | 14 |
| **Y-axis Angular Error Std (°)** | 0.097990728 | 0.044953179 | 0.010491776 | 0.004026962 | 0.003033649 | 0.001107052 | 0.000520737 |
| **Z-axis Angular Error (°)** | 0.025997387 | 0.023211262 | 0.012003648 | 0.007691904 | 0.006863918 | 0.005817026 | 0.005711239 |
| **Z-axis Angular Error (arcseconds)** | 94 | 84 | 43 | 28 | 25 | 21 | 21 |
| **Z-axis Angular Error Std (°)** | 0.070194293 | 0.056326243 | 0.010943411 | 0.004096307 | 0.002970737 | 0.001136845 | 0.000513531 |

in Section 4.4.1 for the 15 test days. Key quaternion statistics are summarized in the second half of Table 10. The mean and median are shown for each term in the quaternion. The error in each quaternion term from the expected unity quaternion $[1\ 0\ 0\ 0]^{\mathrm{T}}$ is, at worst, on the order of 0.000235. Compared to the case without noise the scalar term is almost 1 arcminute farther from ideal, and the standard deviation increased by an order of magnitude.

The results are consistent with the differences seen between Sections 4.4.1 and 4.4.2 when noise was added to SA measurements without an apparent Sun motion correction. There are sign changes in all three vector terms between the mean and median with and without noise. The standard deviations are on par with what was found in Section 4.4.2 with noise.

As discussed in previous sections, a Wilcoxon signed-rank test is used to non-parametrically assess the statistical hypotheses that the mean of each term is statistically identical to zero, and the mean and median are statistically different. The scalar quaternion term is converted to angle space for this test using Equation 31. With a p-value of less than 0.0004 the null hypothesis that the mean of each parameter is statistically identical to zero is rejected for all four quaternion terms. This suggests that a statistically meaningful error in the coordinate transformation exists and warrants further characterization. The mean and median for all four terms are not statistically different with a p-value of 1.0, suggesting that distribution of errors is not skewed.

Similar to Section 4.4.1, Table 12 is created by running 1,000 Monte Carlo simulations for each of the displayed number of comparisons: 2, 10, 100, 500, 1,000, 10,000, 50,000, and 75,000 comparisons per mean. The quantities of interest are total angular error (error in the scalar term) and angular error in each of the X-, Y-, and Z-axes. The standard deviation is also included for each quantity.

Similar to Section 4.4.2, for the total angular error the 60 arcsecond goal is not

**Table 12: Monte Carlo Results With Sun Correction And With Gaussian Measurement Noise.** The mean angular error and standard deviation of the error for 1,000 Monte Carlo runs for various numbers of rotation axis pairings reveals how the error decreases with an increasing number of unique pairings. For a number of comparisons $\frac{1}{2}n(n-1)$ only $n$ occultation events are needed.

| **Number of Comparisons in Mean** | **2** | **10** | **100** | **500** | **1,000** | **10,000** | **50,000** | **75,000** |
|---|---|---|---|---|---|---|---|---|
| **Total Angular Error (°)** | 0.783082398 | 0.453104361 | 0.144689325 | 0.067488588 | 0.05028989 | 0.026129349 | 0.022642529 | 0.021989572 |
| **Total Angular Error (arcseconds)** | 2819 | 1631 | 521 | 243 | 181 | 94 | 82 | 79 |
| **Total Angular Error Std (°)** | 0.778859302 | 0.323463223 | 0.090245933 | 0.03765871 | 0.025830176 | 0.007242733 | 0.003002202 | 0.002190816 |
| **X-axis Angular Error (°)** | 0.671251137 | 0.375579271 | 0.13272446 | 0.059688615 | 0.044205933 | 0.020063162 | 0.015985651 | 0.015513607 |
| **X-axis Angular Error (arcseconds)** | 2417 | 1352 | 478 | 215 | 159 | 72 | 58 | 56 |
| **X-axis Angular Error Std (°)** | 0.840578929 | 0.33018812 | 0.095508675 | 0.041116102 | 0.028779557 | 0.007042709 | 0.002723038 | 0.002199079 |
| **Y-axis Angular Error (°)** | 0.295135373 | 0.150265861 | 0.055088135 | 0.030791358 | 0.0254249 | 0.021323639 | 0.021045616 | 0.020994535 |
| **Y-axis Angular Error (arcseconds)** | 1062 | 541 | 198 | 111 | 92 | 77 | 76 | 76 |
| **Y-axis Angular Error Std (°)** | 0.271369345 | 0.114268959 | 0.033514421 | 0.016158989 | 0.012049338 | 0.004483655 | 0.001993432 | 0.001673317 |
| **Z-axis Angular Error (°)** | 0.776202152 | 0.416803424 | 0.144746399 | 0.0653136 | 0.047869814 | 0.02174184 | 0.017636459 | 0.017187278 |
| **Z-axis Angular Error (arcseconds)** | 2794 | 1500 | 521 | 235 | 172 | 78 | 63 | 62 |
| **Z-axis Angular Error Std (°)** | 0.823161231 | 0.317487673 | 0.092150976 | 0.040308658 | 0.028735271 | 0.007943698 | 0.003358212 | 0.002842551 |

reached by any number of the available comparisons. This reinforces that with noise in azimuth and elevation measurements the angular error goal is not reachable with the limited number of simulated samples. The quaternion generated with 75,000 comparisons in the mean has on average 79 arcseconds of total angular error. The X-axis angular error does drop below 60 arcseconds, however, the Y- and Z-axis errors do not.

The convergence for the angular errors range from the power of $-0.25$ to $-0.37$. The rate of error convergence for the standard deviations follows a power of $-0.53$ on average. These results are consistent with Section 4.4.2.

The added benefit of correcting for apparent Sun position is not distinct when measurement error is included. There was noticeable difference between the cases in Sections 4.4.1 and 4.4.3, but this does not translate when comparing Sections 4.4.2 and the current case. This provides a basis for the argument that an apparent Sun motion correction should not be applied for SAGE III in flight.

### 4.4.5 Combined Results

The presentation of results in Sections 4.4.1 through 4.4.4 can be graphically combined to draw further conclusions about the coordinate transformation error. The following Figures 23 to 26 show the total, X-, Y-, and Z-axis angular errors for all test cases.

The total angular error for the four test cases is graphed in Figure 23. The two cases without additional noise are noticeably smaller in magnitude than the two with noise. The two cases with noise most closely reflect flight conditions. The total angular error for these two cases does not drop below the 60 arcsecond goal proposed for the trend study by the DMP science team, unlike the two cases without noise. This does not imply that an accuracy of less than 60 arcsecond cannot be reached, however. The number of comparisons used for this thesis are limited by the generation of simulated data. On orbit there will be daily data downlinks of approximately 32 solar

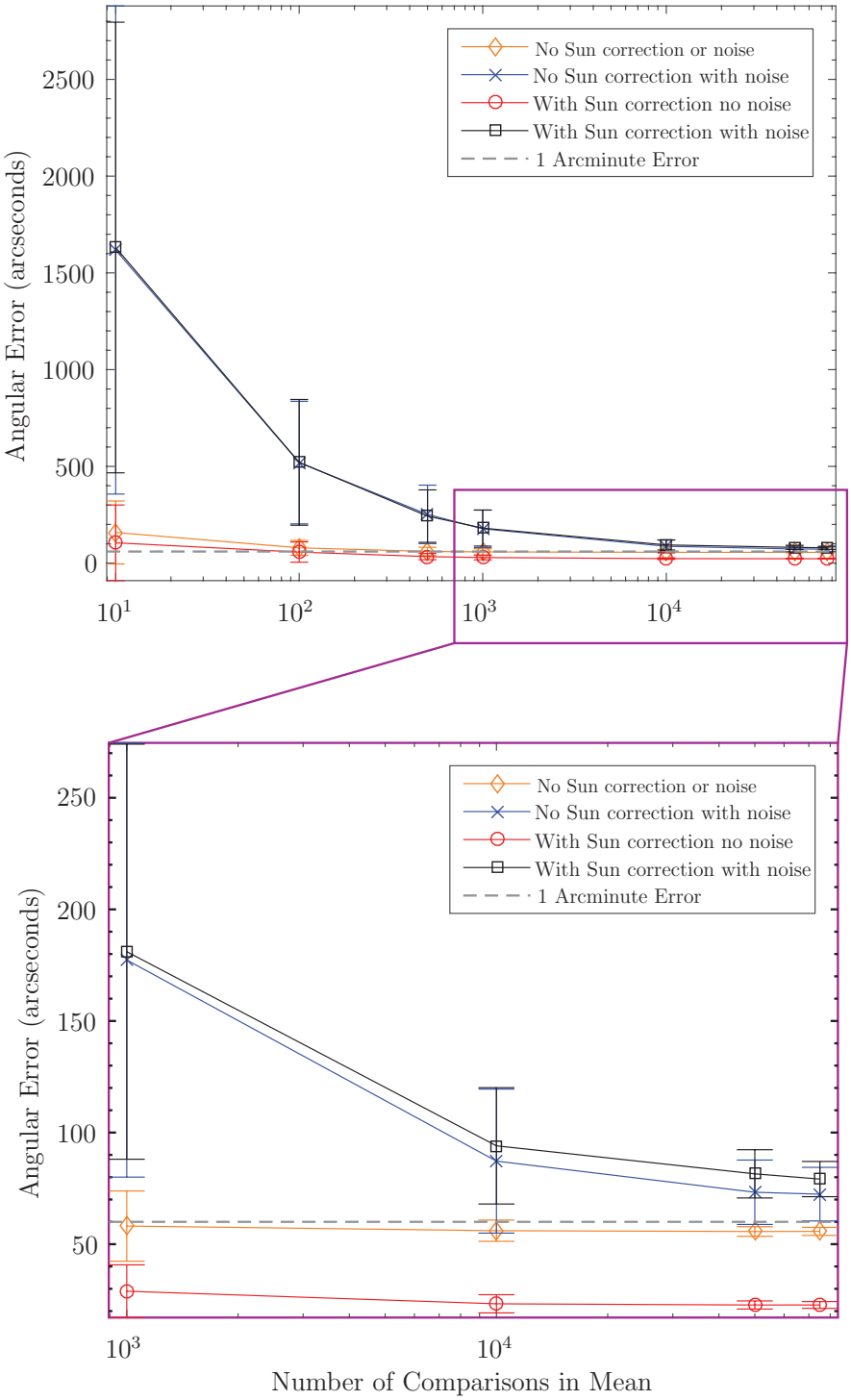


**Figure 23: Total Angular Error versus Number of Comparisons in Mean.** The plot on the top displays comparison sizes 10 to 75,000, and the plot on the bottom displays comparison sizes 1,000 to 75,000. Monte Carlo error bars are $1\sigma$.

events. The number of comparisons will grow during instrument commissioning (the first three months of operation) and when routine operations commence, it is likely a coordinate transformation can be provided using the method found during this investigation. The total angular error trend fit from Sections 4.4.2 and 4.4.4 implies that the number of comparisons needed to reach an error under 60 arcseconds is approximately 58,000 and 75,000 comparisons, respectively. The trend fit to the data slightly underestimates the values suggested towards the tail end of the tables because the fit is imperfect. Nevertheless, the data suggest that the number of comparisons needed to reach 60 arcseconds is ultimately achievable.

The X-axis angular error for the four test cases is graphed in Figure 24. Similar to total angular error in Figure 23, the two cases without measurement noise display a shallow decrease and smaller magnitude than the test cases with noise. With greater than 50,000 comparisons in the mean all four cases are below the 60 arcsecond trending goal. Based on this figure it is expected that the X-axis angular error will be below the threshold on orbit. The high fidelity of the model simulation including the use of flight BAD and TLEs suggests these results are achievable.

The Y-axis angular error for the four test cases is graphed in Figure 25. The overall trends are consistent with the total and X-axis angular errors. At high numbers of comparisons the cases with the apparent Sun motion correction have more error than the cases without the Sun correction, and the error bars for the cases with noise do not overlap. For the Y-axis the apparent Sun correction does not consistently minimize the angular error. The case with Sun correction and noise is the only case that does not reach the 60 arcsecond trending goal.

The Z-axis angular error for the four test cases is graphed in Figure 26. The overall trend is consistent with the total, X-axis, and Y-axis angular errors. For high numbers of comparisons, the error for cases with Sun correction are lower than without, which is not always the case for the total error and the other axes, showing

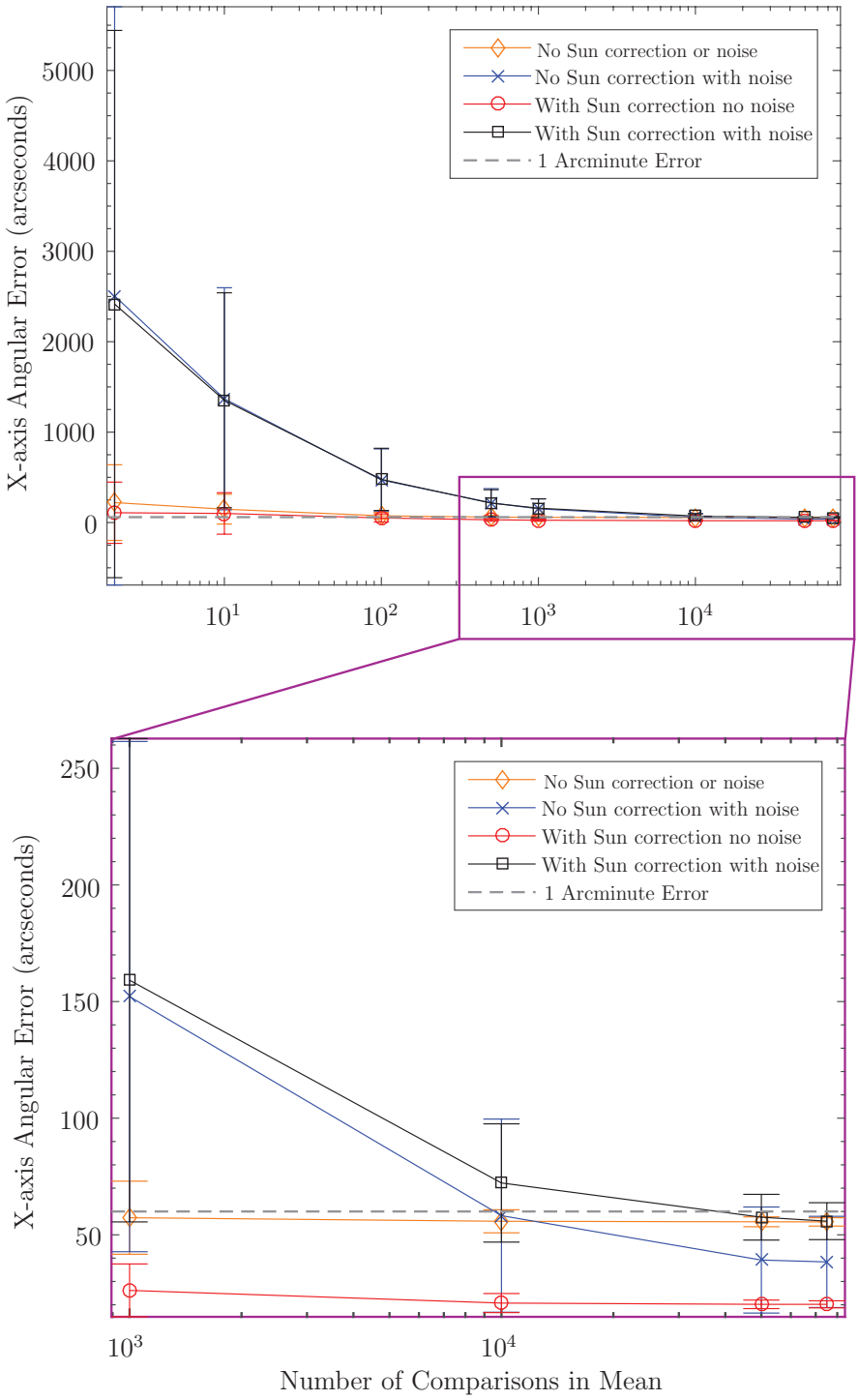


**Figure 24: X-axis Angular Error versus Number of Comparisons in Mean.** The plot on the top displays comparison sizes 10 to 75,000, and the plot on the bottom displays comparison sizes 1,000 to 75,000. Monte Carlo error bars are $1\sigma$.

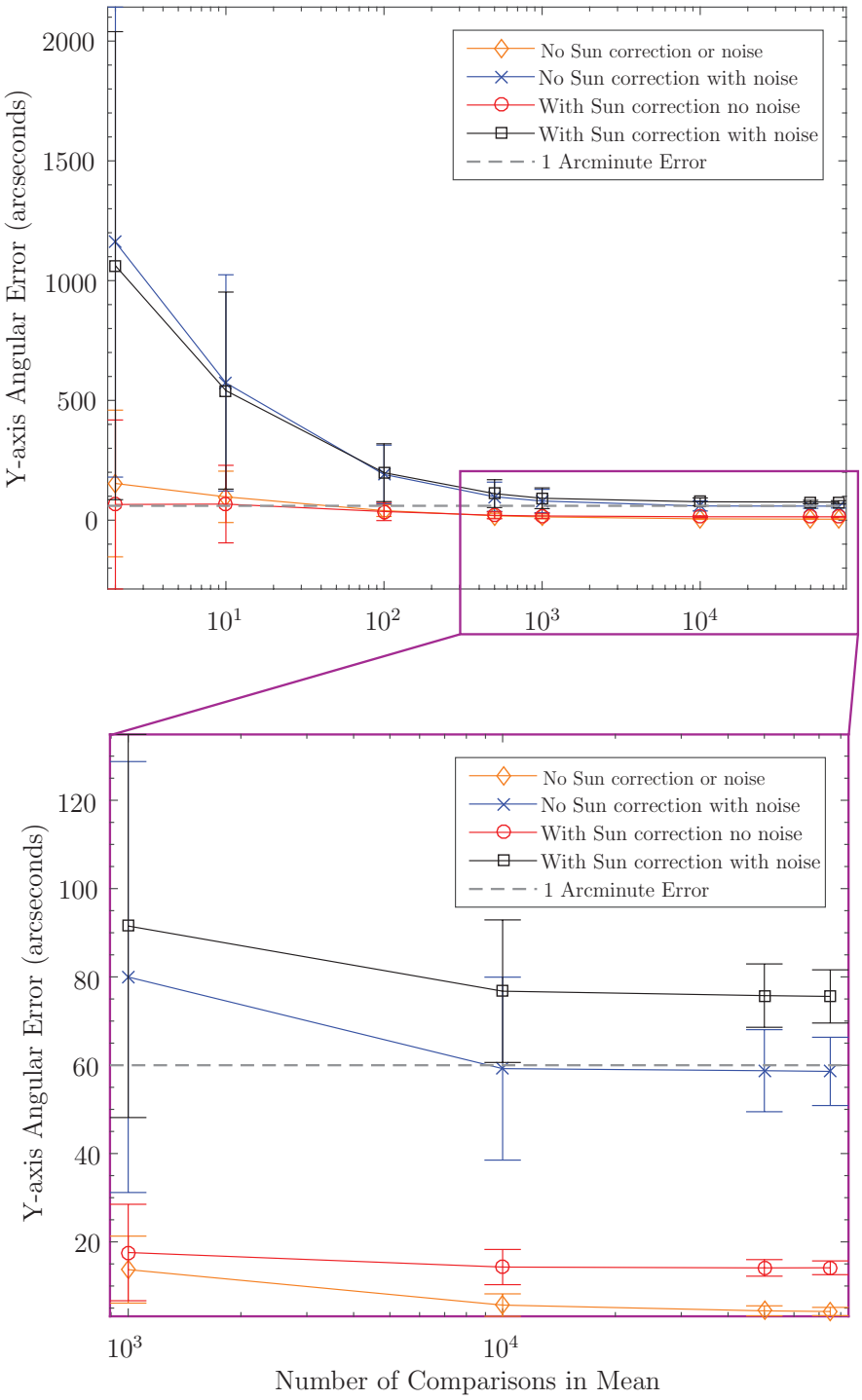


**Figure 25: Y-axis Angular Error versus Number of Comparisons in Mean.** The plot on the top displays comparison sizes 10 to 75,000, and the plot on the bottom displays comparison sizes 1,000 to 75,000. Monte Carlo error bars are $1\sigma$.

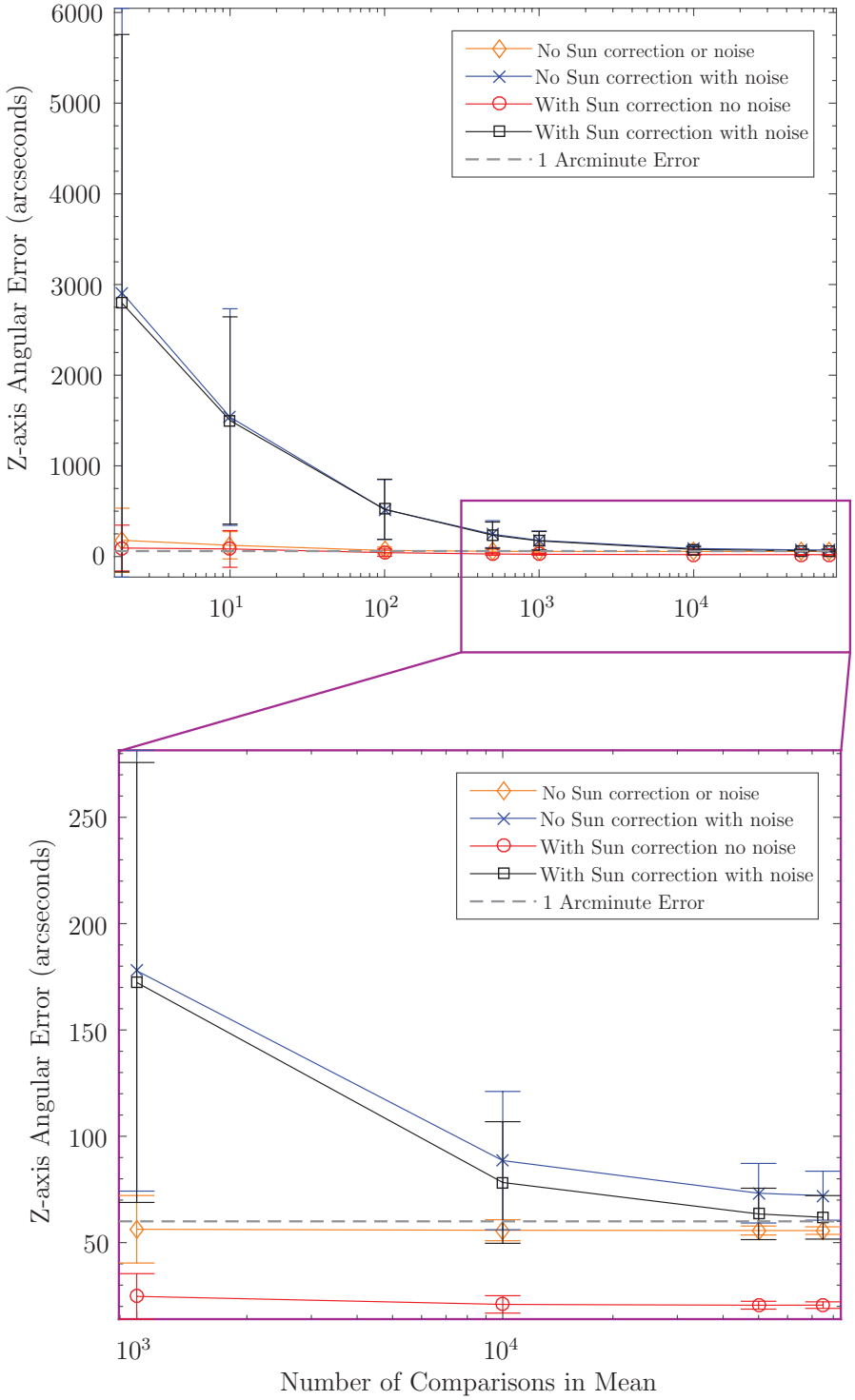


**Figure 26: Z-axis Angular Error versus Number of Comparisons in Mean.** The plot on the top displays comparison sizes 10 to 75,000, and the plot on the bottom displays comparison sizes 1,000 to 75,000. Monte Carlo error bars are $1\sigma$.

that the apparent Sun motion correction is well captured for the Z-axis around which most of that motion occurs during solar occultations. The cases with measurement noise do not drop below the 60 arcsecond trend goal, but the error bars do encompass the threshold.

It was hypothesized in Section 4.2 that the apparent Sun motion correction would be necessary on orbit. From the angular error figures, however, the Sun correction with noise case is consistently within the error bars of the case with no Sun correction and noise with the exception of the Y-axis angular error at large numbers of comparisons in mean. Also, as previously discussed, the Sun correction inconsistently minimizes error. Based on the analysis of the four test cases the apparent Sun motion correction does not need to be applied on orbit.

Using simulated data the 60 arcsecond trending goal requested by the SAGE III DMP science team was not met for all angular errors considered. The error trends decrease at an average power of $-0.5$. When the SAGE III payload is in flight the number of comparisons available will ideally increase with time, and given a coordinate transformation error requirement, multiple coordinate transformation quaternions could be derived during the course of the mission using a determined number of rotation axes pairings, and so changes in the coordinate transformation quaternion between the DMP and SA can be trended over time.

### 4.4.6 Error Around Sun Vector

The previous sections have established the process of determining how many comparisons are needed to derive a stable and accurate average coordinate transformation and the angular error inherent in this quaternion. Once an average quaternion is established on orbit, it will be used to transform DMP measurements to the SA coordinate frame. The application of the coordinate transformation for correcting the altitude registration of the SA solar data is in the "Rate Fix" portion of the SAGE III

transmission algorithm (Damadeo et al., 2013). The rotation error around the Sun vector, or clocking error, is of particular interest because the Rate Fix correction is only applied in the instrument boresight scan plane. The coordinate transformation pitch along the boresight scan direction is irrelevant to the Rate Fix correction because the gyro correction will be made relative to the absolute SA measurements of the solar edges. The aspects of pointing that are important to this process are where the instrument is pointing on the Sun and where in tangent altitude. Clocking error will affect these components of pointing knowledge, and their relationship is coupled.

The amount of noise inherent in pointing on the solar disk that is accounted for in the SAGE III inversion algorithm is a known quantity. The SAGE III DMP science team has directed that clocking error on the order of an arcminute is within the noise for pointing on the solar disk and would not introduce a significant amount of error. How this translates to altitude registration will be discussed in Section 4.4.6.2.

#### *4.4.6.1 Clocking Error*

In Section 3.2.3 the SA partial quaternion $q_2$ (the clocking quaternion) was constructed using the DMP total rotation because the SA is missing a component of total rotation since it reports only two angles. By using this method the DMP total rotation and SA azimuth and elevation angles were assumed to be correct, attributing any difference between partial quaternion $q_1$ and the total rotation observed by the DMP as clocking around the Sun. This assumption introduces error into the clocking because the difference between $q_1$ and the DMP rotation can also be because of error in azimuth and elevation positions, and error in the DMP measurement of rotation. This was the most direct way to derive a coordinate transformation with the measurements supplied by the SAGE III instrument, but the effect of that assumption will manifest itself in the clocking error. The following analysis serves as a measure of how much error is in the clocking and determines if it is small enough to avoid negatively

impacting the science product when a correction using the coordinate transformation is applied.

The clocking error will be a fraction of the full angular error that has been previously derived. To find this error, $\theta_s$, around the Sun vector, rearrange the dot product between the vector portion of the transformation quaternion $\boldsymbol{q}_T$ and Sun vectors $\boldsymbol{s}$.

$$\boldsymbol{q}_T \cdot \boldsymbol{s} = |\boldsymbol{q}_T||\boldsymbol{s}| \cos \alpha. \tag{82}$$

$$\alpha = \arccos \frac{\boldsymbol{q}_T \cdot \boldsymbol{s}}{|\boldsymbol{q}_T||\boldsymbol{s}|}. \tag{83}$$

Relate $\theta_s$ to $\alpha$ using

$$\theta_s = \theta \cos \alpha, \tag{84}$$

where $\theta$ is the transformation quaternion angle. Finally, the error around the Sun vector is found using

$$\theta_s = 2 \arccos (q_\theta) \frac{\boldsymbol{q}_T \cdot \boldsymbol{s}}{|\boldsymbol{q}_T||\boldsymbol{s}|}, \tag{85}$$

where $q_\theta$ is the scalar portion of the transformation quaternion. The full suite of $\boldsymbol{v}_1$ and $\boldsymbol{v}_2$ vectors (as defined in Section 3.2.3) make up the Sun vectors $\boldsymbol{s}$ that are used to find $\theta_s$.

This method of deriving clocking error assumes that the error is small and that the vibration environment in the scan plane is similar to the vibration environment in the plane orthogonal to the scan plane. The dot product between the scan plane and orthogonal plane when offset by a small amount, say an arcminute, when assuming the magnitude of vibration in both planes is comparable, would introduce a negligible amount of angular error.

The clocking error is calculated using the mean coordinate transformations derived from the Monte Carlo simulations described in Section 4.4.2 for each 2, 10, 100, 500, 1,000, 10,000, and 50,000 comparisons in the mean. The mean coordinate transformations are paired with the Sun vectors $\boldsymbol{s}$. On the order of 1,000 Sun vectors are

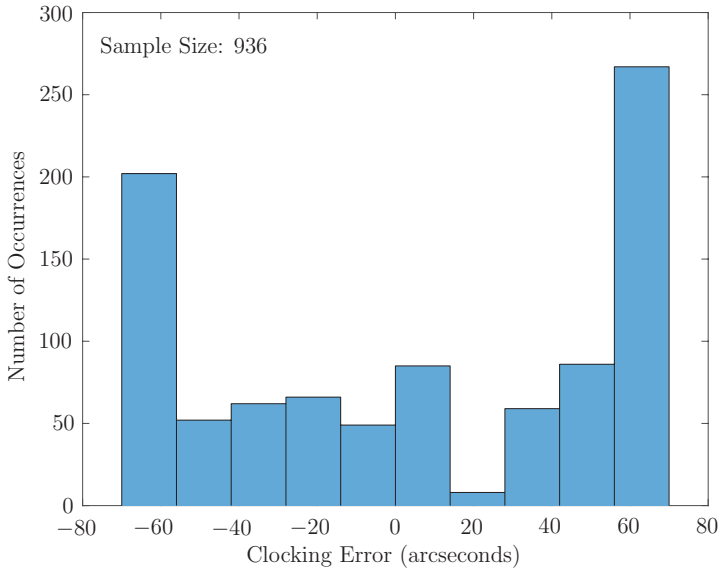


**Figure 27: Clocking Error Distribution.** The histogram shows the distribution of clocking errors for 50,000 comparisons in a mean coordinate transformation quaternion with SA Gaussian measurement noise and no apparent Sun motion correction.

available for pairing over the set of 15 days used for this research. To calculate clocking, the angle constraint described in Section 4.2 is used, no apparent Sun motion correction is applied, and Gaussian SA measurement noise is included.

A distribution of error is shown for the 50,000 comparison case in Figure 27. The distribution is clearly non-Gaussian. In fact, when analyzing the individual clocking errors, the error often oscillates between positive and negative based on event type (Sunrise vs Sunset). This manifestation of error in clocking supports a need to derive separate coordinate transformation quaternions for each event type.

Separating the clocking error by event type in Figure 28 shows a clear positive bias for Sunrise events and negative bias for Sunsets. Sunrise and Sunset events are defined by the apparent motion of the Sun relative to the Earth limb. Table 13 summarizes the associated statistics. The average bias for each event type is approximately half an arcminute, oppositely signed by event type. As expected from Figure 27, the two events are distinctly biased. The skewness statistic proves that the overall distribution is approximately symmetric, whereas both the Sunrise and Sunset distributions are

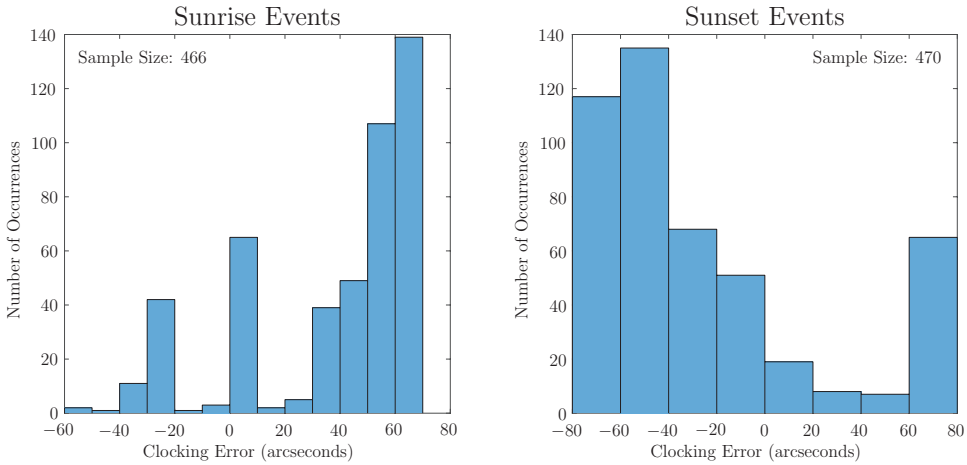


**Figure 28: Clocking Error Distribution Split by Event Type.** The histograms show the distribution of clocking errors for 50,000 comparisons in a mean coordinate transformation with SA Gaussian measurement noise and no apparent Sun motion correction. Sunrise events are on the left, and Sunset events are on the right.

highly skewed with absolute values greater than 1.

The level of error for both event types is acceptable because it is just over an arcminute in the worst case. To minimize the error on orbit from algorithm bias and from thermoelastic effects it is recommended to derive two coordinate transformations, one for each event type.

**Table 13: Clocking Error Statistics for 50,000 Comparisons.** Clocking error statistics are reported for all event types and each event type individually.

| | **All Events** | **Sunrise** | **Sunset** |
|---|---|---|---|
| Mean (arcseconds) | 5.196981726 | 37.1144797 | −26.44887797 |
| Median (arcseconds) | 1.762961084 | 53.77407266 | −53.51357543 |
| Standard Deviation (arcseconds) | 50.63368026 | 32.58757411 | 45.19337211 |
| Minimum (arcseconds) | −67.02146164 | −50.49199141 | −67.02146164 |
| Maximum (arcseconds) | 68.66870538 | 68.44741404 | 68.66870538 |
| Skewness | −0.093294570 | −1.032830995 | 1.125820499 |

The ranges for Sunrise and Sunset events span almost the same range as the combined events. The standard deviation decreases by about 11 arcseconds on average when split by event type. In all cases the means and standard deviations are less than an arcminute on average, and the range of clocking errors only exceeds an arcminute

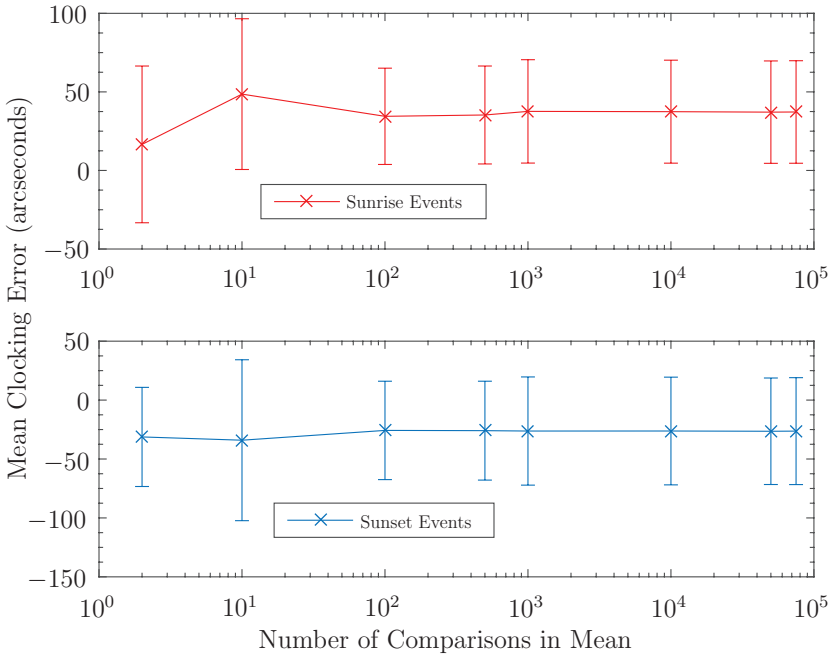


**Figure 29: Mean Clocking Error by Event Type.** The plots show the average clocking error separated by Sunrise and Sunset events. Error bars are $1\sigma$.

by 9 arcseconds in the worst case.

Figure 29 shows the mean clocking error for both Sunrise and Sunset events individually. Because the measurements are inherently noisy, the standard deviation will not become infinitesimally small. The 50,000 comparison case has been used as a basis for analysis following the results shown in Section 4.4.2. The trend in Figure 29 shows the strong positive bias for Sunrise events and negative bias for Sunset events for all numbers of comparisons in the mean further supporting the conclusion reached following Figure 28.

#### *4.4.6.2 Clocking Error Altitude Registration*

The clocking error propagates as an error in the tangent altitude, $Z_t$ (shown in Figure 2 on page 2). This is the error in altitude over a full Sun scan caused by clocking error $\theta_s$. Accurate knowledge of the tangent altitude where the instrument is pointing is important in the retrieval of species in the SAGE III inversion algorithm. Figure 30

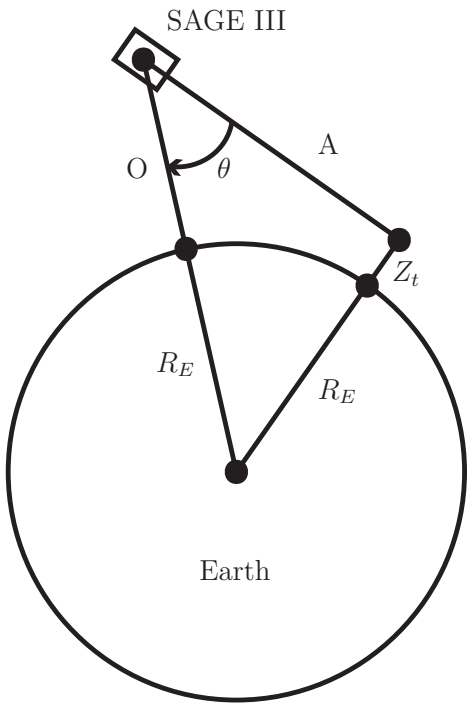


**Figure 30: Defining the Relationship Between $Z_t$ and $\theta$.** The ISS is orbiting the Earth at an altitude $O$ and acquiring science measurements at scan mirror angle $\theta$ with respect to the local spacecraft horizon. Species are retrieved at corresponding tangent altitude $Z_t$.

and Equation 86 show the relationship between tangent altitude and scan angle $\theta$, where $R_E$ is the radius of the Earth, and $O$ is the orbital altitude.

$$\sin\theta = \frac{(R_E + Z_t)}{(R_E + O)}. \tag{86}$$

Rearranging and taking the derivative provides

$$\frac{dZ_t}{d\theta} = (R_E + O)\cos\theta. \tag{87}$$

Solving for $\Delta Z_t$

$$\Delta Z_t = (R_E + O)\cos(\theta)\Delta\theta, \tag{88}$$

for small $\Delta\theta$. The maximum derivative occurs when $\cos\theta = 1$ or $\theta = 0$, but that is not physically possible based on Figure 30. Therefore, the maximum within the

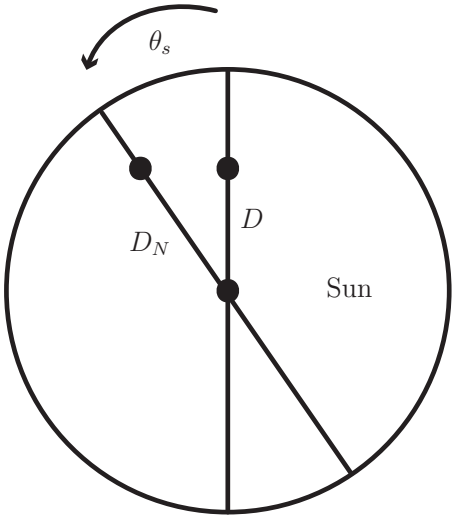


**Figure 31: $\theta_s$ Offset from Scan Plane.** $D$ is measured in the instrument scan plane on the Sun. $D_N$ is offset by $\theta_s$.

physical confines of the problem occurs when $Z_t$ is zero. When $Z_t$ is zero,

$$\theta_{max} = \arcsin \frac{R_E}{R_E + O}. \tag{89}$$

The worst case altitude error $\Delta Z_{t,max}$ can be found by

$$\Delta Z_{t,max} = (R_E + O) \cos(\theta_{max}) \Delta\theta. \tag{90}$$

Figure 31 relates the clocking error $\theta_s$ to the scan plane.

Using the quantities in Figure 31, $\Delta\theta$ can be found.

$$\cos\theta_s = \frac{D}{D_N}, \tag{91}$$

where $D_N$ is the angular height on the Sun during an instrument scan, and $D$ is the projection of $D_N$ into the scan plane. Solving for $\Delta\theta$,

$$\Delta\theta = D_N - D = D_N - D_N \cos\theta_s. \tag{92}$$

$$\Delta\theta = D_N(1 - \cos\theta_s). \tag{93}$$

Solving for $A$ in Figure 30 when $Z_t$ is zero gives

$$A^2 + R_E^2 = (R_E + O)^2 \Rightarrow A = \sqrt{(R_E + O)^2 - {R_E}^2}. \tag{94}$$

Using $A$ to solve for $\cos\theta_{max}$ gives

$$\cos\theta_{max} = \frac{\sqrt{(R_E + O)^2 - {R_E}^2}}{R_E + O}. \tag{95}$$

Substituting Equations 93 and 95 into Equation 90 provides the final $\Delta Z_{t,max}$.

$$\Delta Z_{t,max} = D_N(1 - \cos\theta_s)\sqrt{(R_E + O)^2 - {R_E}^2}. \tag{96}$$

**Table 14: Values For $\Delta Z_t$ Calculation.** Equation 96 will yield altitude registration errors $\Delta Z_{t,max}$ for various clocking errors $\theta_s$. These parameters were assumed for the calculation.

| Variable | Value |
|---|---|
| $R_E$ | 6371 km |
| $O$ | 410 km |
| $D_N$ | 32 arcminutes |

Figure 32 shows the results for $\Delta Z_{t,max}$ using the $\theta_s$ means calculated from all outcomes of the 50,000 comparison case found in Section 4.4.6.1 and constants defined in Table 14. The error in tangent altitude is so small as to be insignificant, with a percentage error less than 0.001% of the stated instrument vertical resolution of 1 km and a maximum value less than 1 meter. Per approval of the SAGE III DMP science team, this level of error is acceptable for incorporation into the inversion algorithm.

### 4.4.7 Non-orthogonal Application

Non-orthogonality in the DMP axes is considered unlikely because Honeywell has flown approximately 400 MIMUs that have not exhibited non-orthogonality in the operational theater. However, since there is a remote possibility of non-orthogonality post-launch, additional analysis is included to detect how violating the assumption of orthogonality from the previous sections might affect the coordinate transformation.

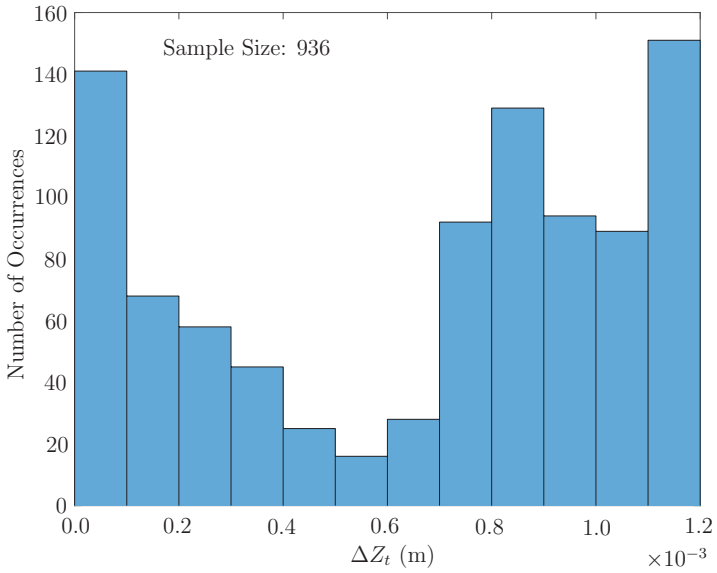


**Figure 32: $\Delta Z_t$ Max Distribution.** This histogram of the maximum tangent altitude errors over 468 occultation events (including scans at both $\boldsymbol{v}_1$ and $\boldsymbol{v}_2$ Sun vectors for each event) is based on a coordinate transformation quaternion using a mean of 50,000 comparisons. SA Gaussian measurement noise was included in the simulation, and no apparent Sun motion correction was made.

The following analysis is a way to gauge if the gyros have shifted on the sensor block resulting in a non-orthogonal coordinate basis and if a post processing orthogonalization might be needed.

The Markley fast quaternion estimation method assumes both orthogonality and measurement error, meaning variation in the output is assumed to be caused by the measurement error alone. Conversely, matrix inversion for six linearly independent measurements does not assume orthogonality but does assume perfect measurements. With perfect measurements differences are assumed to be caused by non-orthogonality. These error assumptions are essentially equivalent for small non-orthogonalities. Mathematically distinguishing between what is measurement error as opposed to the presence of non-orthogonal axes is exceptionally difficult, and ultimately not worthwhile if both effects can be accounted for in one statistical error bar.

Non-orthogonalities are expected to be small for the SAGE III payload, if any non-orthogonality exists, and this supports using the fast quaternion method for finding the coordinate transformation. The coordinate transformation can be calculated using the same method for both an orthogonal and non-orthogonal simulated DMP data set, and the magnitude of the errors can be compared. If a significant difference exists in the comparison, the difference between the expected errors can be used to detect the presence of non-orthogonality on orbit.

For the first three test cases, a small 1 arcminute offset is applied separately to each axis. Next, a small 1 arcminute offset is applied to each axis to form a three-axis non-orthogonal system. These RLG axes are used to generate simulated DMP data on five days: 2 February, 5 February, 25 March, 27 March, and 4 April 2014. The definitions of these axes are provided in Table 6. The quaternion statistics are summarized in Tables 15, 16, and 17 both with and without SA Gaussian measurement error cases. In all cases a Sun correction is applied, and the entirely orthogonal case is included for comparison. The mean and median are shown for each term in the quaternion.

The Wilcoxon signed-rank test is used to non-parametrically test if the mean quaternion of the non-orthogonal cases are statistically significantly different from the baseline. The null hypothesis that the two means are statistically identical is accepted both with and without additional Gaussian measurement error in the SA azimuth and elevation and for non-orthogonality in all axes. The p-value, however, varies for each axis. The largest p-values correspond to Y-axis non-orthogonality (0.875 without noise, 1 with noise) and lowest when the Z-axis or all axes are non-orthogonal (0.625 without noise, 0.25 with noise). The smallest value is well outside the range of statistical likelihood of being different.

Comparing the four small non-orthogonal cases with measurement noise to the baseline case with measurement noise, the standard deviations are the same order of

**Table 15: Small Non-orthogonality Coordinate Transformation Statistics Part 1.** The table lists part 1 of a summary of statistics for the coordinate transformation quaternion terms derived using STK data with slight non-orthogonality in the DMP axes on 2 February, 5 February, 25 March, 27 March, and 4 April 2014 with and without expected Gaussian noise introduced into the SA measurement system. The statistics for the same set of days with orthogonal axes is included as a baseline comparison.

| Quaternion Statistics | Scalar Term | X-term | Y-term | Z-term |
|---|---|---|---|---|
| **Baseline Without Noise** | | | | |
| **Mean** | 0.999999997642070 | $8.86324996641106 \times 10^{-6}$ | 0.000058584485913 | 0.000034715442729 |
| **Median** | 0.999999998741133 | $-8.26592399286581 \times 10^{-7}$ | 0.00004470359266 | 0.000022773649110 |
| **Standard Deviation** | $4.89879766953602 \times 10^{-7}$ | 0.000127902829499 | 0.000329460449783 | 0.000116669517369 |
| **Baseline With Noise** | | | | |
| **Mean** | 0.999999472633020 | 0.000530188504970 | 0.00087799725767 | 0.000052484731837 |
| **Median** | 0.999999923104331 | −0.000241997221682 | 0.000307683546144 | 0.000023653996952 |
| **Standard Deviation** | 0.000134137479585 | 0.003956072880642 | 0.009009206927324 | 0.000333872397786 |
| **Non-orthogonal X-Axis Without Noise** | | | | |
| **Mean** | 0.999999997289514 | 0.000010691780950 | 0.000063696938125 | 0.000035346246415 |
| **Median** | 0.999999998373075 | $-1.81113171112642 \times 10^{-7}$ | 0.000035293464736 | −0.000044812809833 |
| **Standard Deviation** | $4.88767561483072 \times 10^{-7}$ | 0.000127616060479 | 0.000325438407935 | 0.000121148105079 |
| **Non-orthogonal X-Axis With Noise** | | | | |
| **Mean** | 0.999999468345334 | 0.000531935446717 | 0.000883202262967 | 0.000017535497576 |
| **Median** | 0.999999921130275 | −0.000242499203062 | 0.000311569378400 | −0.000043105726404 |
| **Standard Deviation** | 0.000133868035266 | 0.003956007179196 | 0.009000629923455 | 0.000334143909983 |

**Table 16: Small Non-orthogonality Coordinate Transformation Statistics Part 2.** The table lists part 2 of a summary of statistics for the coordinate transformation quaternion terms derived using STK data with slight non-orthogonality in the DMP axes on 2 February, 5 February, 25 March, 27 March, and 4 April 2014 with and without expected Gaussian noise introduced into the SA measurement system.

| Quaternion Statistics | Scalar Term | X-term | Y-term | Z-term |
|---|---|---|---|---|
| **Non-orthogonal Y-Axis Without Noise** | | | | |
| **Mean** | 0.999999995727657 | 0.000011328503648 | 0.0000640391587631 | 0.000065691222387 |
| **Median** | 0.999999997692634 | $-8.05797194852789 \times 10^{-8}$ | 0.0000377282819586 | 0.000056491621162 |
| **Standard Deviation** | $4.94711105880698 \times 10^{-7}$ | 0.000128165364990 | 0.000324921444529 | 0.000121047587390 |
| **Non-orthogonal Y-Axis With Noise** | | | | |
| **Mean** | 0.999999464416299 | 0.000532649635077 | 0.000883447572511 | 0.0000834977152215 |
| **Median** | 0.999999920731542 | −0.000242930430353 | 0.000309935869196 | 0.000058834278119 |
| **Standard Deviation** | 0.000133888319479 | 0.003955847616666 | 0.009001250093989 | 0.000333896209874 |
| **Non-orthogonal Z-Axis Without Noise** | | | | |
| **Mean** | 0.999999994147532 | 0.000093020985203 | 0.000044439352550 | 0.000032820351946 |
| **Median** | 0.999999992757336 | 0.000102146536387 | −0.0000598621196192 | 0.000021631939215 |
| **Standard Deviation** | $4.67768521250185 \times 10^{-7}$ | 0.000128778130580 | 0.000330478030840 | 0.000117017777672 |
| **Non-orthogonal Z-Axis With Noise** | | | | |
| **Mean** | 0.999999606718777 | 0.000428312400659 | 0.000774950775554 | 0.000050616940050 |
| **Median** | 0.999999968667270 | −0.000140289658935 | 0.000206154331990 | 0.000022015054982 |
| **Standard Deviation** | 0.000133900251193 | 0.003956162665771 | 0.009010468181076 | 0.000333772764238 |

**Table 17: Small Non-orthogonality Coordinate Transformation Statistics Part 3.** The table lists part 3 of a summary of statistics for the coordinate transformation quaternion terms derived using STK data with slight non-orthogonality in the DMP axes on 2 February, 5 February, 25 March, 27 March, and 4 April 2014 with and without expected Gaussian noise introduced into the SA measurement system.

| Quaternion Statistics | Scalar Term | X-term | Y-term | Z-term |
|---|---|---|---|---|
| **Non-orthogonal X-, Y-, and Z-Axes Without Noise** | | | | |
| **Mean** | 0.999999995472358 | 0.000088706602862 | 0.000033869190468 | $6.26903471393979 \times 10^{-6}$ |
| **Median** | 0.999999991229747 | 0.000103367241209 | −0.000081470820385 | −0.000014772466843 |
| **Standard Deviation** | $4.71945418910134 \times 10^{-7}$ | 0.000129753879938 | 0.000324617900263 | 0.000134448859904 |
| **Non-orthogonal X-, Y-, and Z-Axes With Noise** | | | | |
| **Mean** | 0.999999597795991 | 0.000432541123178 | 0.000785608891780 | 0.000011606188488 |
| **Median** | 0.999999966384256 | −0.000144777909568 | 0.000214929072870 | $-8.73712534626513 \times 10^{-6}$ |
| **Standard Deviation** | 0.000133382906253 | 0.003955898948585 | 0.008994030510472 | 0.000337441681573 |

magnitude for all quaternion terms. The largest percentage difference in the standard deviation terms corresponds to the three-axis non-orthogonal system with 1.1% greater standard deviation than the baseline case for the Z-term of the quaternion. On average, however, the standard deviations are 0.2% different from the baseline case. From these results it can be concluded that a very small non-orthogonality of an arcminute or less in any of the three axes or in all of the axes at once does not present distinctly different coordinate transformations and does not significantly increase the standard deviation. To determine if this conclusion is definitively supported, the angular error will be analyzed later in this section.

For the next test cases, offsets ranging from 1.281° to 1.811° are applied to each axis individually and the three axes combined on five days: 2 February, 5 February, 25 March, 27 March, and 4 April 2014. The definitions of these axes are provided in Table 6. The quaternion statistics are summarized in Tables 18 and 19 for both with and without SA Gaussian measurement error. In all cases a Sun correction is applied. For the same days the baseline is included in Table 15. The mean and median are shown for each term in the quaternion. The degree of non-orthogonalilty in this test case is far beyond the magnitude expected to be observed on orbit, but it is included as an extreme case for characterization.

Again, the Wilcoxon signed-rank test is used to non-parametrically test if the mean quaternion of the non-orthogonal cases are statistically significantly different from the baseline. The null hypothesis that the means are statistically identical is accepted both with and without Gaussian measurement errors in the SA azimuth and elevation and for non-orthogonality in all axes. Similar to the small non-orthogonal cases the p-values differ greatly for each axis. The largest p-values correspond to Y-axis non-orthogonality (0.625 without noise, 0.875 with noise) and the lowest correspond to cases when the X-axis or all axes are non-orthogonal (0.625 without noise, 0.375 with noise).

**Table 18: Large Non-orthogonality Coordinate Transformation Statistics Part 1.** The table lists part 1 of a summary of statistics for the coordinate transformation quaternion terms derived using STK data with large non-orthogonality in the DMP axes on 2 February, 5 February, 25 March, 27 March, and 4 April 2014 with and without expected Gaussian noise introduced into the SA measurement system.

| Quaternion Statistics | Scalar Term | X-term | Y-term | Z-term |
|---|---|---|---|---|
| **Non-orthogonal X-Axis Without Noise** | | | | |
| **Mean** | 0.999976896298290 | 0.000182034589352 | 0.000532269619464 | 0.006774246976545 |
| **Median** | 0.999979360376369 | −0.000032358459493 | 0.000596631232013 | −0.006397015348687 |
| **Standard Deviation** | 0.000033250247009 | 0.001385238992870 | 0.003177446385533 | 0.003415536749839 |
| **Non-orthogonal X-Axis With Noise** | | | | |
| **Mean** | 0.999976184078268 | 0.000693390332777 | 0.001252916363078 | 0.006751347028634 |
| **Median** | 0.999978606484643 | −0.000358485309816 | 0.001106679444941 | −0.006436872060331 |
| **Standard Deviation** | 0.000121540546697 | 0.004138615221896 | 0.008624233300007 | 0.003417004412331 |
| **Non-orthogonal Y-Axis Without Noise** | | | | |
| **Mean** | 0.999995177544098 | 0.000248572291112 | 0.000559367092247 | 0.003044701762298 |
| **Median** | 0.999994729598382 | −0.000037589364098 | 0.000697687676371 | 0.003170582660137 |
| **Standard Deviation** | 0.000018018186793 | 0.001303670566993 | 0.003028309261887 | 0.003324023791381 |
| **Non-orthogonal Y-Axis With Noise** | | | | |
| **Mean** | 0.999994181309261 | 0.000768645485752 | 0.001281535958437 | 0.003066626375294 |
| **Median** | 0.999994236228436 | −0.000430213239204 | 0.001101775389836 | 0.003182533183891 |
| **Standard Deviation** | 0.000114794080998 | 0.004084892643206 | 0.008609164920563 | 0.003321303427267 |

**Table 19: Large Non-orthogonality Coordinate Transformation Statistics Part 2.** The table lists part 2 of a summary of statistics for the coordinate transformation quaternion terms derived using STK data with large non-orthogonality in the DMP axes on 2 February, 5 February, 25 March, 27 March, and 4 April 2014 with and without expected Gaussian noise introduced into the SA measurement system.

| Quaternion Statistics | Scalar Term | X-term | Y-term | Z-term |
|---|---|---|---|---|
| **Non-orthogonal Z-Axis Without Noise** | | | | |
| **Mean** | 0.999876640915671 | 0.004922713541221 | 0.014915161035281 | 0.000088396133078 |
| **Median** | 0.999873978365550 | 0.004996568958713 | −0.015068352331276 | −0.000080275214019 |
| **Standard Deviation** | $9.74824865036077 \times 10^{-6}$ | 0.000449276357171 | 0.000692207643118 | 0.000434099168738 |
| **Non-orthogonal Z-Axis With Noise** | | | | |
| **Mean** | 0.999890855074517 | 0.004398879469312 | 0.014103979408972 | 0.000074582815222 |
| **Median** | 0.999882062231712 | 0.0047050221983268 | −0.014619292850603 | −0.000025882804161 |
| **Standard Deviation** | 0.000165943712490 | 0.004000632580508 | 0.009114768459042 | 0.000513823421499 |
| **Non-orthogonal X-, Y-, and Z-Axes Without Noise** | | | | |
| **Mean** | 0.999887223555549 | 0.004273784378199 | 0.013863608042926 | 0.003882693587936 |
| **Median** | 0.999890062127189 | 0.004677833427628 | −0.013617059519018 | −0.003543617327620 |
| **Standard Deviation** | 0.000115348808680 | 0.002608239818558 | 0.006135944156035 | 0.006762238849291 |
| **Non-orthogonal X-, Y-, and Z-Axes With Noise** | | | | |
| **Mean** | 0.999898257263280 | 0.003771507672410 | 0.013203259424747 | 0.003863261872388 |
| **Median** | 0.999900966445241 | 0.004289579692790 | −0.012922534924103 | −0.003558777749148 |
| **Standard Deviation** | 0.000182256859294 | 0.004611672027196 | 0.009647924504298 | 0.006752425867332 |

Compared to the baseline and small non-orthogonality cases, when no additional SA Gaussian measurement noise is present there are up to three orders of magnitude difference in the quaternion terms, and the standard deviations are about one order of magnitude larger. When noise is introduced, the quaternion terms resulting from the large non-orthogonal cases are about one order of magnitude larger than the baseline and small non-orthogonal cases with noise. The standard deviations are approximately the same except in the Z-term, which is an order of magnitude larger. On average, however, the standard deviations are 241% larger than the baseline case. With large non-orthogonality on the order of 1° in any or all of the three axes, the standard deviations are significantly larger than the baseline case. If a large non-orthogonality is present post-launch, the magnitudes of the standard deviations in the terms of the derived coordinate transformation quaternion will be one of the indications that non-orthogonality exists. An analysis of angular error will be presented next.

To further analyze the effects of non-orthogonality similar to Section 4.4.2, Tables 20, 21, and 22 are created by running 1,000 Monte Carlo simulations for each of the displayed number of comparisons: 2, 10, 100, 500, 1,000, and 10,000 comparisons per mean. The quantities of interest are total angular error (error in the scalar term) and angular error in each of the X-, Y-, and Z-axes. The standard deviation is also included for each quantity. The tables included are representative of the aforementioned non-orthogonal variations. Table 20 contains the results for the baseline case of the five days with SA Gaussian measurement error, Table 21 for the X-, Y-, and Z-axes small non-orthogonality case with the addition of SA measurement noise, and Table 22 for the X-, Y-, and Z-axes large non-orthogonality case with SA measurement noise. As shown in Table 6 on page 75, for slight non-orthogonality, the offset in each axis is expected to be about 1 arcminute. For large non-orthogonality the angular errors are expected to range from 1.281° in the X-axis to 1.811° in the Z-axis.

**Table 20: Monte Carlo Results Baseline Using Orthogonal DMP Data.** The mean angular error and standard deviation of the error for 1,000 Monte Carlo runs for various numbers of rotation axis pairs is shown for simulated data from 2 February, 5 February, 25 March, 27 March, and 4 April 2014. This provides a baseline using orthogonal data for the subset of days used for non-orthogonal analysis.

| **Number of Comparisons in Mean** | **2** | **10** | **100** | **500** | **1,000** | **10,000** |
|---|---|---|---|---|---|---|
| **Total Angular Error (°)** | 0.862273681 | 0.416970142 | 0.174677116 | 0.128254297 | 0.120886884 | 0.117232998 |
| **Total Angular Error (arcseconds)** | 3104 | 1501 | 629 | 462 | 435 | 422 |
| **Total Angular Error Std (°)** | 0.890411882 | 0.290667486 | 0.102253798 | 0.053726894 | 0.042028331 | 0.013420766 |
| **X-axis Angular Error (°)** | 0.71126083 | 0.351604673 | 0.144434452 | 0.106698323 | 0.100477090.099978649 | |
| **X-axis Angular Error (arcseconds)** | 2561 | 1266 | 520 | 384 | 362 | 360 |
| **X-axis Angular Error Std (°)** | 0.898688821 | 0.298807942 | 0.107518492 | 0.059503977 | 0.047081769 | 0.014816128 |
| **Y-axis Angular Error (°)** | 0.338784391 | 0.162380699 | 0.07618496 | 0.060818984 | 0.060943743 | 0.060854928 |
| **Y-axis Angular Error (arcseconds)** | 1220 | 585 | 274 | 219 | 219 | 219 |
| **Y-axis Angular Error Std (°)** | 0.330973098 | 0.1393109 | 0.05305577 | 0.027456724 | 0.019818004 | 0.006423084 |
| **Z-axis Angular Error (°)** | 0.86122387 | 0.41648371 | 0.1744191 | 0.128077996 | 0.120714647 | 0.117078081 |
| **Z-axis Angular Error (arcseconds)** | 3100 | 1499 | 628 | 461 | 435 | 421 |
| **Z-axis Angular Error Std (°)** | 0.890636779 | 0.290828614 | 0.102358036 | 0.0537666 | 0.042066904 | 0.013429859 |

**Table 21: Monte Carlo Results With Small Non-orthogonality With Gaussian Measurement Noise.** The mean angular error and standard deviation of the error for 1,000 Monte Carlo runs for various numbers of rotation axis pairs with slightly non-orthogonal DMP axes is shown for simulated data from 2 February, 5 February, 25 March, 27 March, and 4 April 2014.

| **Number of Comparisons in Mean** | **2** | **10** | **100** | **500** | **1,000** | **10,000** |
|---|---|---|---|---|---|---|
| **Total Angular Error (°)** | 0.812736053 | 0.426440582 | 0.160427811 | 0.111286107 | 0.106153914 | 0.102835938 |
| **Total Angular Error (arcseconds)** | 2926 | 1535 | 578 | 401 | 382 | 370 |
| **Total Angular Error Std (°)** | 0.840129499 | 0.316748897 | 0.09946425 | 0.050045743 | 0.040553262 | 0.013601645 |
| **X-axis Angular Error (°)** | 0.657766304 | 0.360521333 | 0.135201855 | 0.092684037 | 0.089573553 | 0.089563926 |
| **X-axis Angular Error (arcseconds)** | 2368 | 1298 | 487 | 334 | 322 | 322 |
| **X-axis Angular Error Std (°)** | 0.830727196 | 0.33007871 | 0.105476662 | 0.055505139 | 0.044960012 | 0.014683614 |
| **Y-axis Angular Error (°)** | 0.335880267 | 0.161225462 | 0.064264404 | 0.050590871 | 0.049816705 | 0.049856884 |
| **Y-axis Angular Error (arcseconds)** | 1209 | 580 | 231 | 182 | 179 | 179 |
| **Y-axis Angular Error Std (°)** | 0.363890111 | 0.132615997 | 0.046165549 | 0.025828057 | 0.019806416 | 0.006276175 |
| **Z-axis Angular Error (°)** | 0.81174722 | 0.425917586 | 0.16028145 | 0.11124953 | 0.106130723 | 0.102825863 |
| **Z-axis Angular Error (arcseconds)** | 2922 | 1533 | 577 | 400 | 382 | 370 |
| **Z-axis Angular Error Std (°)** | 0.840161218 | 0.316977105 | 0.09953705 | 0.050054534 | 0.040554354 | 0.013600576 |

**Table 22: Monte Carlo Results With Large Non-orthogonality With Gaussian Measurement Noise.** The mean angular error and standard deviation of the error for 1,000 Monte Carlo runs for various numbers of rotation axis pairs with largely non-orthogonal DMP axes is shown for simulated data from 2 February, 5 February, 25 March, 27 March, and 4 April 2014.

| **Number of Comparisons in Mean** | **2** | **10** | **100** | **500** | **1,000** | **10,000** |
|---|---|---|---|---|---|---|
| **Total Angular Error (°)** | 2.029485666 | 1.70721147 | 1.647111016 | 1.638634364 | 1.634345155 | 1.634866893 |
| **Total Angular Error (arcseconds)** | 7306 | 6146 | 5930 | 5899 | 5884 | 5886 |
| **Total Angular Error Std (°)** | 0.829237405 | 0.446746857 | 0.155734636 | 0.064991988 | 0.049405312 | 0.014771371 |
| **X-axis Angular Error (°)** | 1.901314166 | 1.628953228 | 1.587355892 | 1.580234652 | 1.575856345 | 1.576599682 |
| **X-axis Angular Error (arcseconds)** | 6845 | 5864 | 5714 | 5689 | 5673 | 5676 |
| **X-axis Angular Error Std (°)** | 0.826520266 | 0.459391464 | 0.158025912 | 0.065354719 | 0.049697635 | 0.014996175 |
| **Y-axis Angular Error (°)** | 0.988228493 | 0.700850593 | 0.626510665 | 0.620510243 | 0.619356772 | 0.618802059 |
| **Y-axis Angular Error (arcseconds)** | 3558 | 2523 | 2255 | 2234 | 2230 | 2228 |
| **Y-axis Angular Error Std (°)** | 0.537839748 | 0.270191544 | 0.098758051 | 0.046334115 | 0.031611876 | 0.010149125 |
| **Z-axis Angular Error (°)** | 1.806563213 | 1.601259391 | 1.581458053 | 1.576557949 | 1.572873348 | 1.57379312 |
| **Z-axis Angular Error (arcseconds)** | 6504 | 5765 | 5693 | 5676 | 5662 | 5666 |
| **Z-axis Angular Error Std (°)** | 0.886180973 | 0.485382389 | 0.162695294 | 0.067237233 | 0.051757874 | 0.015310481 |

The magnitude of the errors across the board are larger than what was observed in previous sections because the results encompass only five days. This limits the number of comparisons that can be run in the Monte Carlo simulations without oversampling. Because of this limitation none of the angular errors are below the 60 arcsecond trending goal. This does not present a problem, however, because reaching the science angular error goal is not the purpose of this analysis. The purpose is to identify indications in the data analysis that point to axis non-orthogonalities. Therefore, analyzing the angular error trends is sufficient and a useful exercise.

Consistent with the standard statistics in previous tables, the baseline (Table 20) and small non-orthogonal case (Table 21) produce similar angular error values and have similar standard deviations, thus supporting the conclusion that a small RLG non-orthogonality of 1 arcminute or less will not significantly increase the error. The error convergence for the baseline angular errors follow an average power fit raised to the $-0.24$ power. The rate of error convergence for the standard deviations follow an average power fit of $-0.47$. If the DMP axes shift to a slightly non-orthogonal configuration it will not likely be detected in the coordinate transformation quaternion.

Conversely, comparing Tables 20 and 22 the error terms and their standard deviations are grossly larger than the baseline. At 10,000 comparisons per mean the angular errors are on average a 1233% increase, and the standard deviations are on average a 21% increase over the baseline. Error convergence for the angular errors follow an average power fit raised to the $-0.03$ power. This trend is distinctly different from the baseline and small non-orthogonality cases. The rate of error convergence for the standard deviations follow an average power fit of $-0.47$, which is consistent with the previous two cases.

After evaluating the standard statistics and Monte Carlo analysis it is clear that slight non-orthogonality is not easily ascertainable, and small non-orthogonalities do not substantially increase the angular error of the coordinate transformation. As

expected, very large non-orthogonality noticeably increases angular error and alters the error trends.

The clocking error and corresponding altitude error have a similar relationship in the non-orthogonal case as to the results in Sections 4.4.6.1 and 4.4.6.2. Table 23 compares the two quantities for the baseline, small non-orthogonal, and large non-orthogonal cases.

**Table 23: Clocking Error and $\Delta Z_t$ Statistics for the Non-Orthogonal Cases.** The non-orthogonal clocking and altitude statistics for the large non-orthogonal case are noticeably larger than the baseline and small non-orthogonal cases.

| | $\theta_s$ (arcseconds) | | |
|---|---|---|---|
| | Baseline | Small | Large |
| Mean | −25.92494362 | −24.87458306 | −128.4101896 |
| Median | 16.56398459 | 4.99894246 | 108.2159118 |
| Standard Deviation | 277.9576893 | 243.1145358 | 3673.782312 |
| Minimum | −409.0425264 | −360.4606217 | −5881.046093 |
| Maximum | 414.6531005 | 362.3385566 | 5204.003565 |
| | $\Delta Z_{tmax}$ (meters) | | |
| | Baseline | Small | Large |
| Mean | 0.019733836 | 0.015123058 | 3.421548047 |
| Median | 0.020540861 | 0.015344255 | 3.346848497 |
| Standard Deviation | 0.015661937 | 0.011776804 | 2.300281935 |
| Minimum | $4.15357 \times 10^{-8}$ | $2.95463 \times 10^{-8}$ | $1.28 \times 10^{-4}$ |
| Maximum | 0.043677055 | 0.033351291 | 8.785437771 |

Similar to the conclusions drawn based on the standard statistics and angular error earlier in this section, it is clear that a small non-orthogonality exhibits similar behavior to the baseline case and would not be easy to distinguish. Large non-orthogonality, however, would challenge acceptable levels of error. The maximum altitude deviation is almost 9 meters.

# CHAPTER V

# CONCLUSIONS AND FUTURE WORK

## *5.1 Conclusions*

The presented research explains the essential nature of calibration and attitude determination for SAGE III ISS on-orbit operations. The expected on-orbit performance of the coordinate system calibration has been investigated, and the methods and algorithms to produce an attitude product have been provided. The research questions posed in Section 4.1 which have been answered by the subsequent analyses are summarized herein.

### 5.1.1 Sampling Considerations

The number of solar occultation events that needs to be acquired by the SAGE III payload to derive a well-performing coordinate transformation was extensively investigated in Chapter 4. Of the four cases examined in Sections 4.4.1 through 4.4.4, the two without additional SA Gaussian measurement noise were included as a baseline and do not closely reflect flight conditions. The case with SA Gaussian measurement error and without an apparent Sun motion correction (Section 4.4.2) and the case with both SA Gaussian measurement error and an apparent Sun motion correction (Section 4.4.4) are most representative of what can be expected in flight. The 1 arcminute criterion was used to examine the behavior of the error decay curve. Stability was assessed based on the asymptotic behavior of the angular error and angular error standard deviation trends. Although the 60 arcsecond goal was not consistently reached in either case for the four angular errors analyzed (total, X-, Y-, and Z-axis errors), this was not an analysis requirement. The establishment of the trend was sufficient to estimate the number of solar events needed on orbit and provides insight

to the SAGE III DMP science team to refine the on-orbit angular error requirement. The mean total angular error levels reached were 73 and 79 arcseconds, respectively, which corresponds to just over 1.3 arcminutes in the worst case. The trends indicate that approximately 58,000 and 75,000 comparisons between paired measurements of rotation axes are needed to achieve an error below 60 arcseconds. Assimilating these outcomes, 75,000 comparisons serves as a basis for on-orbit characterization. To be conservative, an estimate of 100,000 comparisons can be established. As described in Section 4.3, the number of solar events needed to reach this level of comparisons is approximately 448. With an average of 32 daily solar events, this level can be achieved using about two weeks of data taken at various times over a full solar beta angle cycle.

Lunar events were not included in the simulated data set for two reasons; The Moon is not as uniform as the Sun, and it moves more quickly with respect to the fixed stars than the Sun. If there is a desire to derive a coordinate transformation on orbit earlier, extending the algorithm to include lunar events is a possibility, but there would be a need for an apparent Moon motion correction. Since the length of the SAGE III ISS commissioning phase is three months, it is possible for a coordinate transformation to be derived before routine operations begin. This is an excellent outcome, but additional factors exist.

### 5.1.2 Effects of ISS Orientation

The placement of a science payload, such as SAGE III, on the ISS platform presents challenges for science data retrievals. The extent to which the ISS operations limit or in some way impact SAGE III can be difficult to predict prior to being on orbit. As such, simulation using the BAD data was essential to the calibration derivation. One of the more surprising outcomes from this research was how integral slew events (large

deviations from ISS TEA) are to the development of an accurate coordinate transformation. From an operations perspective, such events may be viewed as disruptive and potentially damaging to the payload, but for calibration the slew events move the payload axis of rotation within the DMP coordinate frame and thereby provide much needed angular separation between vector inputs to the optimal fast quaternion method. Generally, when such an event is occurring it is because of a spacecraft docking or ISS maintenance. Contamination is of paramount concern during operations, thus suspending science events if a visiting vehicle is outgassing beyond SAGE III limitations. There is also the likelihood that the maneuver causes too much disturbance for science data to be viable, and might also orient the payload such that the HMA cannot maintain the instrument in a nadir-viewing geometry. If the change in orientation is purely a rotation about the ISS Z-axis, then the scan head can compensate because the SAGE III instrument can rotate over 360° in azimuth. Orientation changes about the X- or Y-axis, however, must be within the ±8° for which the HMA can compensate in order for a science event to occur. Although slew events are not guaranteed on orbit, based on several months of BAD they occur on average about once per month. The derivation of a coordinate transformation will be an ongoing process. Even after an initial quaternion is established, routine verification and updates will allow trending to ensure that there are no unexpected deviations over time. Gathering statistics at various TEAs and the full range of beta angles inside a moving temporal window will aid in this verification process.

The angle constraint discussed and established in Section 4.2 is intrinsically linked to a non-static ISS orientation with respect to LVLH. Applying the angle constraint removes outliers in the quaternion terms, as shown in Figure 22 on page 80, and improves the transformation quaternion accuracy. The most effective way to obtain DMP/SA combinations with angular separations greater than a few degrees is

through incorporation of solar events during off-nominal attitudes caused by ISS maneuvers with solar events acquired at nominal ISS attitudes. These maneuvers are not predictable prior to launch, but historical data suggest one such maneuver could be witnessed within a month of being on orbit. Currently 12 ISS dockings are scheduled for 2017, confirming the historical maneuver frequency will likely continue after the SpaceX-10 launch.

Although exact on-orbit conditions cannot be predicted, it is possible to estimate how the angle constraint could prolong the calibration of the initial coordinate transformation. Equation 81 in Section 4.3 calculates the number of comparisons that can be generated from $n$ samples. If $m$ represents the number of samples captured during off-nominal ISS orientations, Equation 81 becomes

$$\text{number of comparisons} = m \times n, \tag{97}$$

because this represents the number of pairs that do not violate the angle constraint. The number of events $n$ accumulated during the three month commissioning phase is about 2,880 events. To reach 100,000 comparisons in this time period about 35 samples, or just over one day of science events, would need to be at an off-nominal ISS attitude. With an off-nominal orientation approximately once a month and based on the durations seen in BAD used for the simulated data set, 35 samples is achievable. Even if contamination limits occultations or if slew events are not as frequent as predicted, a coordinate transformation should be established within the first six months of on-orbit operations.

As the beta angle cycle causes TEA variations the angular separation between measured rotation axes will vary as well. The rotation axis angular separations were approximately 8.5° or less over a full beta cycle for the chosen 11 simulated test days during which the ISS maintained a nominal TEA. This means that the ISS TEA wobbles with respect to LVLH by about 8.5° over a full beta cycle. With an angular constraint of 10° the calibration cannot be performed, but a relaxed angular

constraint could be used to build a set of rotation axes. This will be discussed further in Section 5.2.1.

### 5.1.3 Effects of Instrument Noise

Sections 4.4.2 and 4.4.4 incorporated realistic instrument measurement Gaussian noise into the simulated STK data. The effects of the noise on the transformation quaternion terms were pronounced. Between the cases with and without noise, the increase in angular error ranged from 2–53 arcseconds at 10,000 comparisons in the mean. It is because of noise that statistics and time become important. The trends in angular error and standard deviation presented and analyzed in Chapter 4 show that with an increasing number of combinations the angular error decreases toward some unknown asymptote, and the standard deviations diminish correspondingly. By extrapolating these trends, it is feasible and realistic to expect that once the appropriate number of comparisons have been accumulated on orbit, the desired level of accuracy is achievable despite measurement noise. That behavior is considered a validation of the proposed calibration technique. It is likely that the flight angular error requirement, to be defined by the SAGE III DMP science team, will be larger than the 60 arcsecond goal presented in the thesis further supporting the conclusion that measurement noise will not prevent reaching this goal.

### 5.1.4 Effects of Non-Orthogonality

Two non-orthogonal coordinate frames were simulated for DMP data in STK. The first frame incorporated an arcminute per axis of non-orthogonality, which would be the most likely maximum limit if indeed any non-orthogonality occurs in flight, and the second coordinate frame introduced large non-orthogonality for demonstration purposes. For both test configurations non-orthogonality was introduced to each of the X-, Y-, and Z-axes individually as well as all three axes simultaneously. Although variation did exist between the inclusion of non-orthogonality in each or all axes, the

angular error trends were similar throughout all configurations. Through this analysis, it was determined that small RLG non-orthogonality, whether it be in an individual axis or multiple axes, is not easily detectable and also not significantly detrimental to the derived coordinate transformation quaternion. If non-orthogonality occurs in the DMP, it will presumably not be ascertained through the derivation or analysis of the transformation quaternion. Large non-orthogonality was easily detectable by the magnitude of the variance in the coordinate transformation quaternion terms, and the angular error trends were distinctly different from the baseline case.

### 5.1.5 Effects of Apparent Sun Motion

The phenomenon of apparent Sun motion was initially described in Section 3.2.3.1. The correction process was then applied in Sections 4.4.3 and 4.4.4. Based on these results, it can be concluded that applying an apparent Sun motion correction is not beneficial enough to use on orbit, as illustrated by Figures 23 through 26. The averages for the cases with noise and with/without a Sun correction (shown in black or blue, respectively) are almost statistically identical based on the error bars. Additionally, in many instances the mean case without a Sun correction outperforms the case with a Sun correction. Incorporating an apparent Sun motion correction was a straightforward process for the STK simulation, but accounting for how the Sun moves with respect to the fixed stars would have been a challenge on orbit. In flight, there is no readily available mechanism to use the ICRF Sun vector because the corresponding ICRF attitude rates of the payload would have to be known. This would require a knowledge of the absolute attitude of SAGE III to uncouple attitude motions from the apparent Sun motion. It was a beneficial exercise to incorporate Sun motion corrections in the thesis analyses, but proving that this is not advantageous to the calibration effort is the best possible outcome.

### 5.1.6 Assessment of Clocking Error

Section 4.4.6 describes the effect of the clocking error, or attitude error around the Sun vector, which would result after applying the derived coordinate transformation to incorporate the DMP data (by way of coordinate transformation to SA coordinates) into Level 1 science data processing. This error represents the primary source of pointing error caused by incorporating DMP measurements into generating a SAGE III ISS science data product. The clocking error corresponds to that part of the angular error in the estimate of the location of the instrument's boresight scan plane that is not corrected by the SAGE III measurements of the locations of the top and bottom edges of the solar disk. The Rate Fix algorithm is used within the scan plane to calculate an effective boresight scan rate on the Sun by combining the instrument scan mirror rate with the spacecraft attitude rates. The mean error for the case with SA measurement noise and no apparent Sun motion correction is just over 5 arcseconds and ranges from approximately -67 to 69 arcseconds. Guidance from the SAGE III DMP science team confirms that this level of error is acceptable and is within the existing algorithm noise. There is evidence suggesting that Sunrise and Sunset events might have clocking error biases in opposite directions of each other, although this might be an artifact of the chosen days for the simulated data set rather than an algorithmic bias. Nevertheless, when considered with the possibility of thermoelastic differences between Sunrise and Sunset events, this opens the possibility that clocking error might be improved by finding separate coordinate transformations based on solar event type. This will be discussed more in Section 5.2.1.

The tangent altitude that corresponds to an instrument measurement is correlated to the clocking error. The aforementioned range of clocking errors corresponds to less than 1 meter of error in the altitude registration. Even in the small non-orthogonal case, the maximum error was 0.03 meters. Guidance from the SAGE III DMP science team suggests that a delta altitude on the order of 3 meters is acceptable. Of all the

test cases addressed in Chapter 4, only the large non-orthogonal case exceeds this threshold with a maximum of almost 9 meters. Because large non-orthogonality was included for demonstration, not because it is a likely possibility, error in altitude registration is not expected to be a concern on orbit.

There is a clear path forward for assessing the stability and accuracy of the coordinate transformation algorithm on orbit, and the results of this thesis provide a preview of what can be expected and how external factors influence the calibration.

## *5.2 Future Work*

A worthwhile and challenging endeavor is never complete. There are always improvements and updates that can be made and minor problems to be addressed. In the context of this thesis, the on-orbit application of the aforementioned algorithms is the primary future task, but this opens a realm of possible applications including comparison opportunities and Algorithm Theoretical Basis Document (ATBD) creation.

### 5.2.1 Flight Implementation

The research in this thesis was conducted with flight implementation in mind, but many items were identified throughout the research process that have yet to be addressed, some because of simulation limitations, others because of flight unknowns.

The coordinate transformation algorithm is designed such that there are minimal changes needed for the incorporation of flight data upon delivery. There are several items, however, that can be investigated or reevaluated on orbit. The construction of the DMP quaternions in Section 3.2.2 creates a partial quaternion for each 200 Hz measurement and multiplies them to construct a total quaternion. The successive multiplication of a large number of quaternions is susceptible to propagated roundoff error. It may be worth investigating averaging the DMP partial quaternions to reduce the number of quaternion multiplications, with the expectation that averaging would alleviate error propagation up to a point. At a certain threshold, the data averaging

benefits would diminish proportional to the loss of precise knowledge of attitude rate.

The angular constraint described and established in Section 4.2 was not rigorously optimized. The cutoff angles were selected by weighing the benefit of minimizing error and disadvantage of removing samples. Once angular separation for the SA and DMP vectors is calculated with flight data, it would be advantageous to reconsider the angle constraints. Additionally, if off-nominal ISS orientations are not feasible for science data acquisition, the coordinate system calibration must rely on beta angle cycle TEA variation for angular separation also causing the angular constraint to be reconsidered. In this case, relaxing the angular constraints allows the inclusion of samples over a full beta angle cycle, and although the accumulation of samples will take longer without off-nominal ISS orientation, this provides an alternative method to accumulate rotation axes.

As mentioned in Section 5.1, lunar events were not included in the simulated data set. Although using the Moon as a "Moon sensor", similar to how the Sun is used as a Sun sensor, presents multiple challenges, if there is a great need to provide a transformation quaternion more quickly than is possible using only solar events, the addition of lunar events could be explored. This would require a method to account for Moon non-uniformity and a correction for apparent lunar motion.

As described in Section 4.4.6.1, the Sunrise and Sunset events exhibit opposite clocking error biases. It is unclear if the same bias will be seen in flight data, but two transformations based on event type should be considered when establishing the first coordinate transformation on orbit.

The Hexapod subsystem was not included in the simulated data set because the orientation correction is assumed in SA pointing. The error in Hexapod position, however, will impact the coordinate transformation accuracy. It would be possible to simulate the Hexapod by applying a noisy rotation quaternion to the SA. Typical Hexapod positions were used extensively in ground testing. The knowledge of the

Hexapod attitude quaternion is within ±1 arcminute as shown in Table 3. An additional measurement noise could be included to capture this. The derivation of the coordinate transformation also does not consider thermoelastic effects. It would be possible to fit a hypersurface to the transformation during a single event that is a function of time/solar elevation and beta angle to capture thermal effects. Thermoelastic effects will manifest as biased Hexapod error on orbit.

As previously mentioned, the flight DMP integrates measured angular rate to return X, Y, and Z angular positions at 200 Hz. The simulated STK DMP data are rates. The flight implementation will convert the DMP angles to rates because they can be summed in quadrature to derive the DMP quaternions as described in Section 3.2.2.

The most substantial item addressed in this thesis that has not been fully realized is the implementation of a multiplicative extended Kalman filter to provide a DMP attitude product. The method outlined in rigorous detail in Section 3.3 is a starting point for many possible innovations to the Kalman filter, including smoothing and running the filter backward as well as forward as mentioned in Section 3.3.2.4 to reduce the attitude discontinuities at the measurement updates. One known open item is the process of constructing the SA attitude quaternion for the measurement update step. Also, there is the possibility of incorporating additional data sources. For example, BAD or other ISS attitude products could be introduced as another absolute measurement in the filter if the ISS bending mode error is small. A considerable amount of effort could be dedicated to determining an optimal procedure to run the Kalman filter, and the creation of an attitude data product would have multiple uses.

### 5.2.2 Data Set Comparisons

The creation of a SAGE III DMP attitude data product provides benefits to the payload as well as the ISSP and other external payloads. Limb scattering events require

full attitude determination because, unlike solar and lunar events, there is no target to track during instrument scans. The process is not as simple and straightforward as correcting for motion in only the scan plane, which requires only relative DMP measurements. Using the MEKF to derive a DMP attitude product and incorporating the attitude in the science inversion algorithm will supply accurate pointing knowledge for limb science data.

An ATBD documents the methods and assumptions of a particular EOS algorithm providing the user with abundant information on how a data product is derived thereby ensuring proper data usage. There are four existing SAGE III ATBDs, and following the work of this thesis one of these documents can be appended or a new document can be created. Publishing the calibration and attitude determination methods of the SAGE III DMP supports the entire ISS community. The ISSP has expressed interest in a DMP data product. Other external science payloads, either already on the ISS or those slated to launch at a future date, might need to understand the ISS attitude environment just as the SAGE III team was assisted by the HREP team during project development.

The community is small, but attitude products do exist for several locations on the ISS. The addition of a SAGE III DMP product will generate interest in comparisons between published ISS data products, including BAD and the Reconstructed ISS Attitude from both the SAGE III Project and other ISS payloads. Two possible collaborations and comparisons are with the Alpha Magnetic Spectrometer (AMS-02) payload and the Multiple User System for Earth Sensing (MUSES) payload. Fortuitously, MUSES also includes a Honeywell MIMU, whereas AMS-02 has a dual star tracker system.

The DMP calibration process and attitude determination algorithm defined in this thesis will contribute to the success and advancement of the SAGE III mission data

products. The calibration technique defining the coordinate transformation quaternion between the SA and DMP subsystems and associated errors is well-established and understood, and has been demonstrated with simulated data sets. Incorporation of this calibration into the science inversion algorithm will provide a correction to instrument pointing leading to an improved science product. The defined MEKF algorithm can be implemented using data from the DMP and SA on orbit to establish an attitude product. Not only will this be used as pointing knowledge for limb scattering measurements, but will also provide an opportunity to compare to existing ISS attitude measurements at multiple ISS locations, further characterizing the ISS environment and internal bending modes.

## *5.3 Coda*

While creating a beautifully constructed theory can be enjoyable, there is nothing like diving into an application. This thesis experience has been a balance between the theoretical and the practical aspects of a challenging, interesting, and ongoing task for the SAGE III ISS Project. This technical problem inspired the creation of a new calibration technique and integrated existing attitude determination knowledge in a novel way, proving that there is always something new to learn and develop. The calibration algorithm presented will improve science retrieval accuracy and provide opportunities for occultation measurements lower into the troposphere, ultimately aiding in the understanding of atmospheric composition. The attitude algorithm will expedite the creation of a highly-desired DMP attitude product, demonstrating the worthwhile and exciting nature of this research endeavor. Though the bulk of the work is complete and ready for use when the payload is on orbit, plenty remains to be fully resolved, creating another opportunity for future researchers to push the boundaries of science.

# APPENDIX

## DERIVATION OF STATE TRANSITION MATRIX

The following is an independent derivation of state transition matrix $\boldsymbol{A}$ that arrives at the same solution as Trawny and Roumeliotis (2005). This is continuing from Equation 60 in Chapter 3.

Begin with the differential equation of the error state $\boldsymbol{x}$

$$\dot{\tilde{\boldsymbol{x}}} = \boldsymbol{F}_c\tilde{\boldsymbol{x}} + \boldsymbol{G}_c\boldsymbol{n} \tag{98}$$

where $\boldsymbol{F}_c = \begin{bmatrix} -\lfloor\hat{\boldsymbol{\omega}}\times\rfloor & -\boldsymbol{I}_3 \\ \boldsymbol{0}_3 & \boldsymbol{0}_3 \end{bmatrix}$, $\boldsymbol{G}_c = \begin{bmatrix} -\boldsymbol{I}_3 & \boldsymbol{0}_3 \\ \boldsymbol{0}_3 & \boldsymbol{I}_3 \end{bmatrix}$, and $\boldsymbol{n}$ is white noise. The $c$ subscript implies continuous equations, not discrete time steps.

To solve, multiply by $e^{-\boldsymbol{F}_c t}$ giving

$$\dot{\tilde{\boldsymbol{x}}}e^{-\boldsymbol{F}_c t} = \boldsymbol{F}_c\tilde{\boldsymbol{x}}e^{-\boldsymbol{F}_c t} + \boldsymbol{G}_c\boldsymbol{n}e^{-\boldsymbol{F}_c t}. \tag{99}$$

Rearranging gives a complete differential such that

$$\frac{d}{dt}\tilde{\boldsymbol{x}}e^{-\boldsymbol{F}_c t} = \boldsymbol{G}_c\boldsymbol{n}e^{-\boldsymbol{F}_c t}. \tag{100}$$

Integrate to find

$$\int_{t_0}^{t} d(\tilde{\boldsymbol{x}}e^{-\boldsymbol{F}_c t}) = \int_{t_0}^{t} \boldsymbol{G}_c\boldsymbol{n}e^{-\boldsymbol{F}_c t}dt \;\Rightarrow\; \tilde{\boldsymbol{x}}(t)e^{-\boldsymbol{F}_c t} - \tilde{\boldsymbol{x}}(t_0)e^{-\boldsymbol{F}_c t_0} = \int_{t_0}^{t} \boldsymbol{G}_c\boldsymbol{n}e^{-\boldsymbol{F}_c t}dt. \tag{101}$$

Multiplying by $e^{\boldsymbol{F}_c t}$ isolates $\tilde{\boldsymbol{x}}(t)$.

$$\tilde{\boldsymbol{x}}(t) = e^{\boldsymbol{F}_c(t-t_0)}\tilde{\boldsymbol{x}}(t_0) + \int_{t_0}^{t} e^{\boldsymbol{F}_c(t-\tau)}\boldsymbol{G}_c(\tau)\boldsymbol{n}(\tau)d\tau. \tag{102}$$

The function of $e^{\boldsymbol{F}_c(t-t_0)}$ must be determined. First, find the expectation value $\hat{\tilde{\boldsymbol{x}}}$, remembering that $\boldsymbol{n}$ is white noise as a function of time

$$\Rightarrow E\left[\int_{t_0}^{t} \boldsymbol{n}(\tau)d\tau\right] = 0. \tag{103}$$

$$\hat{\tilde{\boldsymbol{x}}}(t) = e^{\boldsymbol{F}_c(t-t_0)}\hat{\tilde{\boldsymbol{x}}}(t_0) + 0. \tag{104}$$

So, $\boldsymbol{A}(t,t_0) = e^{\boldsymbol{F}_c(t-t_0)}$ is the state propagator or state transition matrix.

This gives the following relation

$$\tilde{\boldsymbol{x}}(t) = \boldsymbol{A}(t,t_0)\tilde{\boldsymbol{x}}(t_0) + \int_{t_0}^{t} \boldsymbol{A}(t,\tau)\boldsymbol{G}_c(\tau)\boldsymbol{n}(\tau)d\tau. \tag{105}$$

Differentiate to obtain

$$\dot{\tilde{\boldsymbol{x}}}(t) = \dot{\boldsymbol{A}}(t,t_0)\tilde{\boldsymbol{x}}(t_0) + \int_{t_0}^{t} \dot{\boldsymbol{A}}(t,\tau)\boldsymbol{G}_c(\tau)\boldsymbol{n}(\tau)d\tau + \boldsymbol{A}(t,t)\boldsymbol{G}_c(t)\boldsymbol{n}(t). \tag{106}$$

But $\boldsymbol{A}(t,t) = 1$. Comparing Equation 106 and 98 implies that $\dot{\boldsymbol{A}}(t,t_0) = \boldsymbol{F}_c\boldsymbol{A}(t,t_0)$.

$$\dot{\tilde{\boldsymbol{x}}}(t) = \boldsymbol{F}_c\left[\boldsymbol{A}(t,t_0)\tilde{\boldsymbol{x}}(t_0) + \int_{t_0}^{t} \boldsymbol{A}(t,\tau)\boldsymbol{G}_c(\tau)\boldsymbol{n}(\tau)d\tau\right] + \boldsymbol{G}_c\boldsymbol{n}. \tag{107}$$

Let $\dot{\boldsymbol{A}} = \begin{bmatrix} \dot{\boldsymbol{A}}_1 & \dot{\boldsymbol{A}}_2 \\ \dot{\boldsymbol{A}}_3 & \dot{\boldsymbol{A}}_4 \end{bmatrix}_{6\times 6}$ and $\boldsymbol{A} = \begin{bmatrix} \boldsymbol{A}_1 & \boldsymbol{A}_2 \\ \boldsymbol{A}_3 & \boldsymbol{A}_4 \end{bmatrix}_{6\times 6}$. Then

$$\dot{\boldsymbol{A}} = \boldsymbol{F}_c\boldsymbol{A} \Rightarrow \begin{bmatrix} \dot{\boldsymbol{A}}_1 & \dot{\boldsymbol{A}}_2 \\ \dot{\boldsymbol{A}}_3 & \dot{\boldsymbol{A}}_4 \end{bmatrix} = \begin{bmatrix} -\lfloor\boldsymbol{\omega}\times\rfloor & \boldsymbol{I}_3 \\ \boldsymbol{0}_3 & \boldsymbol{0}_3 \end{bmatrix} \begin{bmatrix} \boldsymbol{A}_1 & \boldsymbol{A}_2 \\ \boldsymbol{A}_3 & \boldsymbol{A}_4 \end{bmatrix}. \tag{108}$$

Clearly $\dot{\boldsymbol{A}}_3 = \boldsymbol{0}_3$ and $\dot{\boldsymbol{A}}_4 = \boldsymbol{0}_3$. Therefore, $\dot{\boldsymbol{A}}_1$ and $\dot{\boldsymbol{A}}_2$ are left to be found by examining following boundary conditions.

$$\boldsymbol{A}(t_0,t_0)\tilde{\boldsymbol{x}}(t_0) = \tilde{\boldsymbol{x}}(t_0) \Rightarrow \boldsymbol{A}(t_0,t_0) = \boldsymbol{I}_6. \tag{109}$$

Meaning

$$\boldsymbol{A}_1(t_0,t_0) = \boldsymbol{A}_4(t_0,t_0) = \boldsymbol{I}_3 \quad \text{and} \quad \boldsymbol{A}_2(t_0,t_0) = \boldsymbol{A}_3(t_0,t_0) = \boldsymbol{0}_3. \tag{110}$$

But

$$\dot{\boldsymbol{A}}_3 = \boldsymbol{0}_3 \Rightarrow \boldsymbol{A}_3(t,t_0) = \boldsymbol{0}_3 \quad \text{and} \quad \dot{\boldsymbol{A}}_4 = \boldsymbol{0}_3 \Rightarrow \boldsymbol{A}_4(t,t_0) = \boldsymbol{I}_3. \tag{111}$$

Therefore

$$\dot{\boldsymbol{A}}_1 = -\lfloor\hat{\boldsymbol{\omega}}\times\rfloor\boldsymbol{A}_1 \quad \text{and} \quad \dot{\boldsymbol{A}}_2 = -\lfloor\hat{\boldsymbol{\omega}}\times\rfloor\boldsymbol{A}_2 + \boldsymbol{I}_3. \tag{112}$$

Assuming $\hat{\boldsymbol{\omega}}$ is constant over time step $t_0 \to t$ the solution to the $\boldsymbol{A}_1$ differential equation is the usual $\boldsymbol{A}_1(t,t_0) = e^{-\int_{t_0}^{t} \lfloor \hat{\boldsymbol{\omega}} \times \rfloor dx} = e^{-\lfloor \hat{\boldsymbol{\omega}} \times \rfloor (t-t_0)}$. For $\boldsymbol{A}_2$ the total differential is formed by multiplying by $e^{\int_{t_0}^{t} \lfloor \hat{\boldsymbol{\omega}} \times \rfloor dt}$.

$$e^{\int_{t_0}^{t} \lfloor \hat{\boldsymbol{\omega}} \times \rfloor dt} \dot{\boldsymbol{A}}_2 = -\lfloor \hat{\boldsymbol{\omega}} \times \rfloor \boldsymbol{A}_2 e^{\int_{t_0}^{t} \lfloor \hat{\boldsymbol{\omega}} \times \rfloor dt} + e^{\int_{t_0}^{t} \lfloor \hat{\boldsymbol{\omega}} \times \rfloor dt}. \tag{113}$$

Collect terms in $\boldsymbol{A}_2$ to obtain

$$e^{\int_{t_0}^{t} \lfloor \hat{\boldsymbol{\omega}} \times \rfloor dt} \dot{\boldsymbol{A}}_2 + \lfloor \hat{\boldsymbol{\omega}} \times \rfloor \boldsymbol{A}_2 e^{\int_{t_0}^{t} \lfloor \hat{\boldsymbol{\omega}} \times \rfloor dt} = e^{\int_{t_0}^{t} \lfloor \hat{\boldsymbol{\omega}} \times \rfloor dt}. \tag{114}$$

$$\frac{d}{dt} \boldsymbol{A}_2 e^{\int_{t_0}^{t} \lfloor \hat{\boldsymbol{\omega}} \times \rfloor dt} = e^{\int_{t_0}^{t} \lfloor \hat{\boldsymbol{\omega}} \times \rfloor dt}. \tag{115}$$

Integrate with respect to time and remember that $\boldsymbol{A}_2(t_0,t_0) = \boldsymbol{0}_3$.

$$\begin{aligned} \boldsymbol{A}_2(t,t_0) e^{\int_{t_0}^{\tau_2} \lfloor \hat{\boldsymbol{\omega}} \times \rfloor d\tau_2} - \boldsymbol{0}_3 &= \int_{t_0}^{t} e^{\int_{t_0}^{t} \lfloor \hat{\boldsymbol{\omega}} \times \rfloor d\tau_1} dt. \\ \Rightarrow \boldsymbol{A}_2(t,t_0) &= \int_{t_0}^{t} e^{-(\int_{t_0}^{\tau_2} \lfloor \hat{\boldsymbol{\omega}} \times \rfloor d\tau_2 - \int_{t_0}^{t} \lfloor \hat{\boldsymbol{\omega}} \times \rfloor d\tau_1)} dt. \end{aligned} \tag{116}$$

Assuming $\hat{\boldsymbol{\omega}}$ constant over interval $t_0 \to t$.

$$\boldsymbol{A}_2(t,t_0) = \int_{t_0}^{t} e^{-\lfloor \hat{\boldsymbol{\omega}} \times \rfloor (\tau - t_0 + \tau_0 - t)} dt = \int_{t_0}^{t} e^{-\lfloor \hat{\boldsymbol{\omega}} \times \rfloor (\tau - t)} dt. \tag{117}$$

This begs the question of how to evaluate the exponential $e^{\boldsymbol{X}}$ of matrix $\boldsymbol{X}_{nxn}$. Using the division algorithm it may be written as

$$e^{\boldsymbol{X}} \equiv 1 + \boldsymbol{X} + \frac{\boldsymbol{X}^2}{2} + \ldots = \underbrace{det(\boldsymbol{X} - \lambda \boldsymbol{I})}_{\text{order n}} \underbrace{\boldsymbol{Q}_{\infty}(\boldsymbol{X})}_{\text{order } \infty} + \underbrace{\boldsymbol{R}_{n-1}(\boldsymbol{X})}_{\substack{\text{at most order} \\ \text{n-1 (remainder)}}}. \tag{118}$$

There will be n eigenvalues $\lambda_1$, $\lambda_2$, ..., $\lambda_n$. Take for example

$$det(\lfloor \hat{\boldsymbol{\omega}} \times \rfloor - \lambda \boldsymbol{I}_3) = \begin{vmatrix} -\lambda & -\omega_3 & \omega_2 \\ \omega_3 & \lambda & -\omega_1 \\ -\omega_2 & \omega_1 & \lambda \end{vmatrix} \tag{119}$$

$$= -\lambda \begin{vmatrix} \lambda & -\omega_1 \\ \omega_1 & \lambda \end{vmatrix} + \omega_3 \begin{vmatrix} \omega_3 & -\omega_1 \\ -\omega_2 & \lambda \end{vmatrix} + \omega_2 \begin{vmatrix} \omega_3 & \lambda \\ -\omega_2 & \omega_1 \end{vmatrix} \tag{120}$$

$$= -\lambda(\lambda^2 + \omega_1^2) + \omega_3(\lambda\omega_3 - \omega_1\omega_2) + \omega_2(\omega_3\omega_1 + \lambda\omega_2) \tag{121}$$

$$= -\lambda(\lambda^2 + \omega_1^2 + \omega_3^2 + \omega_2^2) = -\lambda(\lambda^2 + |\vec{\boldsymbol{\omega}}|^2). \tag{122}$$

Set $det(\lfloor\hat{\boldsymbol{\omega}}\times\rfloor - \lambda\boldsymbol{I}_3) = 0 \Rightarrow \lambda = 0$ or $\lambda = \pm i\boldsymbol{\omega}$, the characteristic polynomial with three eigenvalues. Where $\lambda = 0$ or $\lambda = \pm i\boldsymbol{\omega} \Rightarrow e^{\lfloor\hat{\boldsymbol{\omega}}\times\rfloor} = \boldsymbol{R}_{n-1}(\lfloor\hat{\boldsymbol{\omega}}\times\rfloor)$. For $\lfloor\hat{\boldsymbol{\omega}}\times\rfloor$, $n = 3$. Hence, $\boldsymbol{R}_{n-1}(\lfloor\hat{\boldsymbol{\omega}}\times\rfloor)$ will be order two at most. Clearly,

$$det(-\lfloor\hat{\boldsymbol{\omega}}\times\rfloor(t - t_0) - \lambda\boldsymbol{I}_3) = -(t - t_0)\begin{vmatrix} \frac{-\lambda}{-(t-t_0)} & -\omega_3 & \omega_2 \\ \omega_3 & \frac{\lambda}{-(t-t_0)} & -\omega_1 \\ -\omega_2 & \omega_1 & \frac{\lambda}{-(t-t_0)} \end{vmatrix}, \tag{123}$$

yields eigenvalues from before $\frac{\lambda}{-(t-t_0)} = 0$ or $\pm i\boldsymbol{\omega}$. Hence, $\lambda = 0$, $\pm i\boldsymbol{\omega}(t - t_0)$. Now, the Cayley-Hamilton theorem guarantees that the remainder polynomials $\boldsymbol{R}_{n-1}(\boldsymbol{X})$ and $\boldsymbol{R}_{n-1}(\lambda)$ are the same since matrix $\boldsymbol{X}$ satisfies its own characteristic polynomial. Hence, we may use the eigenvalues to find the coefficients of $\boldsymbol{R}_{n-1}$.

$$e^2 = \boldsymbol{R}_{n-1}(\lambda) = c_0 + c_1\lambda + c_2\lambda^2. \tag{124}$$

$$\lambda = 0 \Rightarrow e^0 = c_0 \quad \text{or} \quad c_0 = 1. \tag{125}$$

$$\lambda = \pm i\boldsymbol{\omega}(t - t_0) \Rightarrow e^{\pm i\boldsymbol{\omega}(t-t_0)} = 1 + c_1[\pm i\boldsymbol{\omega}(t - t_0)] + c_2[\pm i\omega(t - t_0)]^2. \tag{126}$$

$$\Rightarrow \cos(\boldsymbol{\omega}\Delta t) + i\sin(\boldsymbol{\omega}\Delta t) = 1 - c_2\boldsymbol{\omega}^2\Delta t + ic_1\boldsymbol{\omega}\Delta t \tag{127}$$

$$\cos(\boldsymbol{\omega}\Delta t) = 1 - c_2\boldsymbol{\omega}^2\Delta t \quad \text{and} \quad \sin(\boldsymbol{\omega}\Delta t) = c_1\boldsymbol{\omega}\Delta t \tag{128}$$

Finally,

$$c_1 = \frac{\sin(\boldsymbol{\omega}\Delta t)}{\boldsymbol{\omega}\Delta t} \quad \text{and} \quad c_2 = \frac{1 - \cos(\boldsymbol{\omega}\Delta t)}{\boldsymbol{\omega}^2\Delta t}. \tag{129}$$

# REFERENCES


Alenia Spazio (1998). *Hexapod/SAGE III/ISS Interface Requirements Document (IRD)*. Turin, Italy. HEX-ESA-RQ-002.

Alenia Spazio (2005). *Hexapod User's Manual*. Turin, Italy. HEXMA AI0003.

Allred, R. (2010). *Digital Filters For Everyone*. Creative Arts & Sciences House, Indian Harbour Beach, Florida. ISBN: 9780982972908.

Armenise, M. N., Ciminelli, C., Dell'Olio, F., and Passaro, V. M. N. (2011). *Advances in Gyroscope Technologies*. Springer Publishing, New York, NY. ISBN: 9783642154935.

Ball Aerospace & Technologies Corp. (2012). *SAGE III Command and Telemetry Definition for ISS*. Boulder, CO. 546483 Rev E.

Bar-Itzhack, I. Y. (1971). Optimum normalization of a computed quaternion of rotation. *IEEE Transactions on Aerospace and Electronic Systems*, AES-7(2):401–402. DOI: 10.1109/TAES.1971.310384.

Black, H. D. (1964). A passive system for determining the attitude of a satellite. *AIAA Journal*, 2(7):1350–1351. DOI: 10.2514/2.5048.

Black, H. D. (1990). Early development of Transit, the Navy Navigation Satellite System. *Journal of Guidance, Control, and Dynamics*, 13(4):577–585. DOI: 10.2514/3.25373.

Bradley, Jr., O. H., Mauldin, L. E., McCormick, M. P., Ray, A. J., and Baer, J. W. (1994). The Stratospheric Aerosol and Gas Experiment III (SAGE III) instrument for the Earth Observer System (EOS) program. In *32nd Aerospace Sciences Meeting & Exhibit*. 10–13 January, Reno, Nevada, AIAA 94-0600.

Chu, W. P., Trepte, C. R., and Taha, G. (2002). Initial comparison of SAGE III data with GOMOS and SCIAMACHY. In *Proceedings of Envisat Validation Workshop*. Frascati, Italy, 9–13 December, ESA SP-531.

Crassidis, J. L. and Junkins, J. L. (2012). *Optimal Estimation of Dynamic Systems*. CRC Press, Boca Raton, FL. ISBN: 9781439839867.

Cutright, S. (2011). SAGE III distrubance monitoring package concept study. Technical report, NASA Langley Research Center. SAGE III-SYS-027.

Damadeo, R. P., Zawodny, J. M., Thomason, L. W., and Iyer, N. (2013). SAGE version 7.0 algorithm: application to SAGE II. *Atmospheric Measurement Techniques*, 6:3539–3561. Issues 4–8, Benefits of Space for Humanity. DOI: 10.5194/atm-6-3539-2013.

Farrenkopf, R. L. (1978). Analytic steady-state accuracy solutions for two common spacecraft attitude estimators. *Journal of Guidance, Control, and Dynamics*, 1(4):282–284. DOI: 10.2514/3.55779.

Folkner, W. M., Williams, J. G., Boggsand, D. H., Park, R. S., and Kuchynka, P. (2014). The planetary and lunar ephemerides DE430 and DE431. Technical report, Jet Propulsion Laboratory. IPN Progress Report 42-196.

Giardina, C. R., Bronson, R., and Wallen, L. (1975). An optimal normalization scheme. *IEEE Transactions on Aerospace and Electronic Systems*, AES-11(4):443–446. DOI: 10.1109/TAES.1975.308105.

Hamilton, W. (1844). On quaternions; or on a new system of imaginaries in algebra. *Philosophical Magazine*, 25:10–13.

Hill, C. A. (2014). SAGE III IA RVDT and azimuth resolver calibration test. Technical report, NASA Langley Research Center. SAGE III-05-299a-TR-001.

Honeywell International Inc. (2010). *User's Manual for the Miniature Inertial Measurement Unit (MIMU) Inertial Reference Unit (IRU).* Clearwater, FL. UMYG9666HA, Rev B.

ISSP (2001). Space station reference coordinate systems. Technical report, NASA International Space Station Program. SSP 30219 Revision F.

Johnson, T. (2016). SAGE III-10-205 end-to-end NVP/IP/ELC PRCU2 test report. Technical report, NASA Langley Research Center. SAGE III-10-205-TR-002.

Kalman, R. E. (1960). A new approach to linear filtering and prediction problems. *Transactions of ASME – Journal of Basic Engineering*, 82:35–45.

Kuipers, J. B. (1999). *Quaternions and Rotation Sequences.* Princeton University Press, Princeton, New Jersey. ISBN: 9780691102986.

Lefferts, E. J., Markley, F. L., and Shuster, M. D. (1982). Kalman filtering for spacecraft attitude estimation. *Journal of Guidance, Control, and Dynamics*, 5(5):417–429. DOI: 10.2514/3.56190.

Markley, F. L. (1993). Attitude determination using vector observations: A fast optimal matrix algorithm. *The Journal of Astronautical Sciences*, 41(2):261–280.

Markley, F. L. (2002). Fast quaternion attitude estimation from two vector measurements. *Journal of Guidance, Control, and Dynamics*, 25(2):411–414. DOI: 10.2514/2.4897.

Markley, F. L. (2003). Attitude error representations for Kalman filtering. *Journal of Guidance, Control, and Dynamics*, 26(2):311–317. DOI: 10.2514/3.2555.

Markley, F. L. (2004a). Attitude estimation or quaternion estimation? *Journal of Astronautical Sciences*, 52(1–2):221–238.

Markley, F. L. (2004b). Multiplicative vs. additive filtering for spacecraft attitude determination. In *In Dynamics and Control of Systems and Structures in Space*.

Markley, F. L., Cheng, Y., Crassidis, J. L., and Oshman, Y. (2007). Averaging quaternions. *Journal of Guidance, Control, and Dynamics*, 30(4):1193–1196. DOI: 10.2514/1.28949.

McCormick, M. P. (1991). SAGE III capabilities and global change. In *29$^{th}$ Aerospace Sciences Meeting*. 7–10 January, Reno, Nevada, AIAA 91-0051.

Prussing, J. E. and Conway, B. A. (1993). *Orbital Mechanics*. Oxford University Press, New York, New York. ISBN: 9780195078343.

Roberts, R. R., Milov, Y. G., Zonov, Y. V., Salikhov, R. S., and Charles, L. B. (1996). IAN-USA SAGE III/Meteor-3M project. *Acta Astronautica*, 38:479–485. DOI: 10.1016/0094-5765(96)00020-3.

Schaub, H. and Junkins, J. L. (1996). Stereographic orientation parameters for attitude dynamics: A generalization of the Rodrigues parameters. *Journal of the Astronautical Sciences*, 44(1):1–19.

Shuster, M. D. and Oh, S. D. (1981). Three-axis attitude determination from vector observations. *Journal of Guidance and Control*, 4(1):70–77.

Thornton, B. (2013). Sunlook test BAI rotation calculation. Technical report, NASA Langley Research Center. SAGE III-I&T-001.

Thornton, B. and Hall, S. (2013). Stratospheric Aerosol and Gas Experiment III (SAGE III on ISS) mission concept of operations. Technical report, NASA Langley Research Center. SAGE III-07-001.

Trawny, N. and Roumeliotis, S. I. (2005). Indirect Kalman filter for 3D attitude

estimation. Technical report, NASA Langley Research Center. TR-2005-002, Rev. 57.

Wahba, G. (1966). A least squares estimate of satellite attitude. *SIAM Review*, 7(3):409. DOI: 10.1137/1007077.

Wertz, J. R. (1978). *Spacecraft Attitude Determination and Control*. Reidel Publishing Company, Dordrecht, Holland. ISBN: 9789027712042.

Wilcoxon, F. (1945). Individual comparisons by ranking methods. *Biometrics Bulletin*, 1(6):80–83. DOI: 10.2307/3001968.